ISSN 1349-6832

# JEOL news

June2009 Vol.44 No.1

## JEOL 60th Anniversary Issue

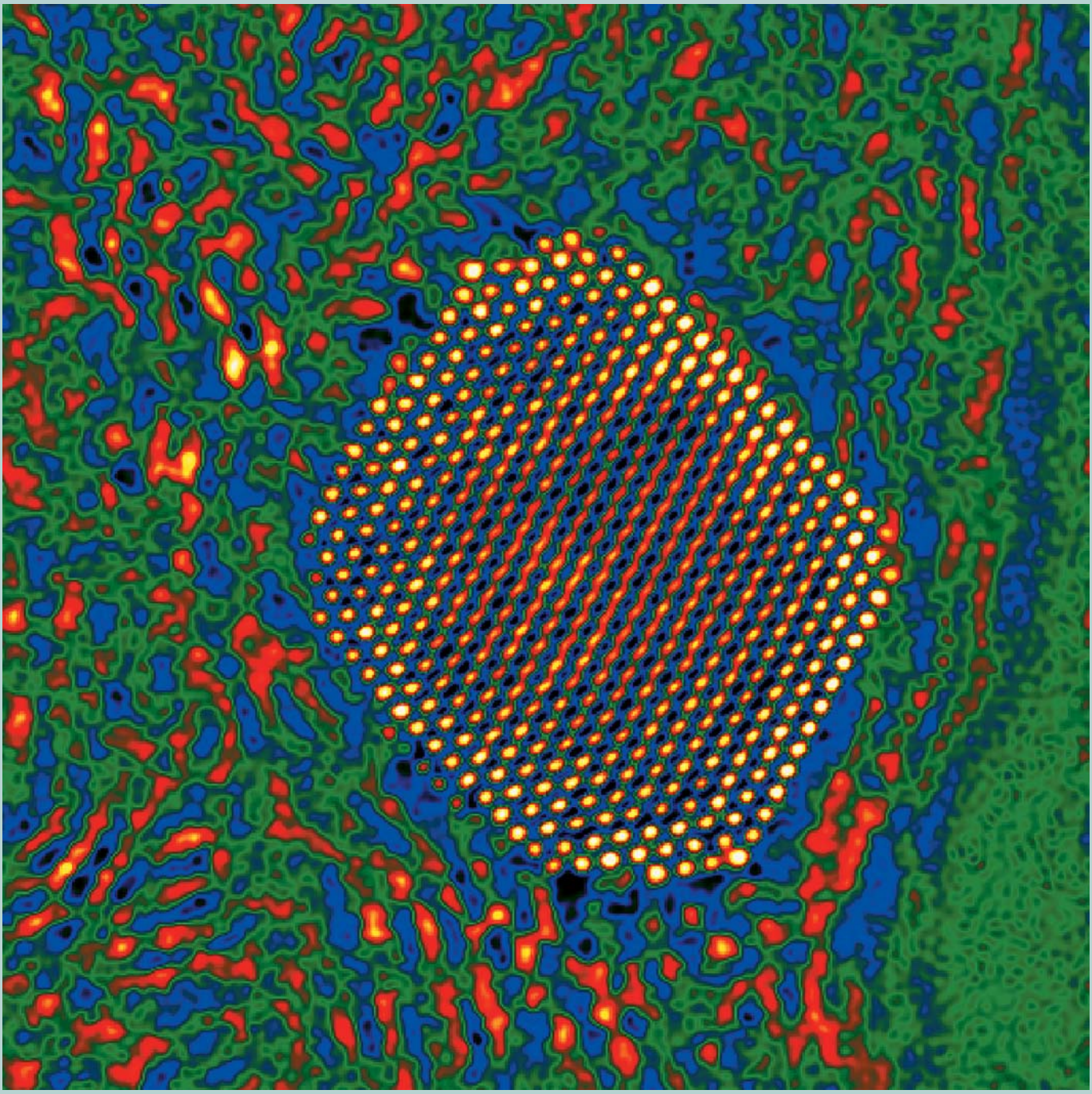

Professor David Cockayne FRS

# Congratulatory Message for the 60th Anniversary of JEOL

It is a great pleasure to have the opportunity to write a Congratulatory Message for the 60th Anniversary of JEOL. This is a very significant milestone, dating as it does from the establishment of Japan Electron Optics Laboratory Co. Ltd. in Mitaka, Tokyo in 1949, and the completion of the JEM-1 electron microscope.

The relationship between scientific researchers and instrument manufacturers is very important to science. In the early days of optics, the instrument makers were themselves the scientists (e.g. Leeuwenhoek, Hooke), and to some extent this situation still holds today. But generally the complexity and cost of instruments now requires collaboration between research laboratories and instrument manufacturers if significant electron optical advances are to be achieved. Each depends upon the other for progress, and the closer the interaction, the more rapid the progress. This is a relationship which is difficult to sustain in a commercial environment, requiring trust and mutual respect. JEOL has built up this relationship to a remarkable level of sophistication. The flow of ideas and skills between University laboratories and JEOL has had a huge impact upon instrument development. JEOL has listened to the needs of researchers, and has supported development projects in their infancy, not altruistically but with an understanding of the symbiotic benefits of this relationship. Over the many years that I have had the privilege and enjoyment of using JEOL microscopes, a highlight has been jam sessions in the Board Room in Tokyo or elsewhere, throwing around ideas and enjoying the company and expertise of the JEOL engineers.

Of course most of us know JEOL through the instrument itself, and the real joy of the instrument is when it becomes an extension of oneself. Ergonomically this was a challenge with some of the early TEMs, where contortions that seemed easy for the JEOL engineers seemed impossible for some of us mere research students. I recall gun alignment, with arms stretched firmly behind one's ears, as being particularly painful! But with the latest JEM-2200MCO double aberration-corrected TEM/STEM, one is in heaven.

JEOL can be proud of its unique and outstanding contribution to science. It has built up an enviable reputation as an innovator and manufacturer of wonderful instruments, which provide some of the clearest windows onto the nanoworld. All of us, whether users of JEOL or competitors' instruments, owe a debt to the Company for its contribution to our field of science.

**Professor David Cockayne FRS**
Department of Materials, University of Oxford
Past-President, IFSM

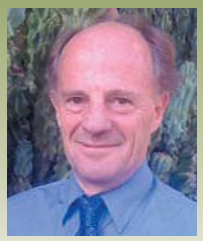

Regents Professor David J. Smith

# Congratulations from Arizona State University

As a long-time JEOL friend, customer *and* microscope user, I am delighted to be writing this letter of congratulations on the occasion of the sixtieth anniversary of JEOL. Arizona State University and JEOL have historically had a close and mutually beneficial relationship. This partnership dates from 1970 when John M. Cowley was appointed to the post of Galvin Professor of Physics at Arizona State University. Cowley soon thereafter took delivery of one of the very first JEM-100Bs to be sold commercially (Serial # 2), and this instrument enabled Iijima and Cowley to record their famous, award-winning images of block-oxide crystal structures [1,2]. Our second JEM-100B (*circa.* 1973) was also equipped with a scanning attachment that enabled early energy-filtered imaging of thick biological samples [3].

The intervening years have quickly passed and our success stories using JEOL microscopes have continued to multiply in number and grow in impact. Many generations of graduate students from diverse scientific disciplines, such as physics, chemistry, materials, and geology, have both learned the basics of electron microscopy and then honed their microscopy skills using our ever-dependable JEOL instruments before moving onto careers elsewhere. Notable among several JEOL microscopes that have been located at ASU during this period, our JEM-4000EX has produced atomic-resolution electron micrographs continuously ever since its installation and commissioning in late 1984 right through to the present day. Some of its earliest results were described in a previous *JEOL News* [4]. Mechanical parts associated with specimen exchange mechanisms and camera systems have inevitably worn out from heavy usage and have needed replacement. Nevertheless, the original guaranteed structural resolution of 0.17 nm is still obtainable on a daily routine basis even after (or despite) well over 200,000 micrographs recorded. This ongoing superior performance represents a glowing testimonial to the original design of the instrument, the exceptional quality of its construction and assembly, and the excellent training and skills of the JEOL service engineers who helped to install the scope and who have been our 'lifeline' in case of occasional need ever since. My ASU colleagues and I have greatly valued our interactions at all levels of JEOL, including design engineers, sales representatives and the service organization, and we are looking forwards to many more years of flourishing and productive science using JEOL microscopes.

Congratulations once again on reaching this historic landmark!


[1] S. Iijima, *J. Appl. Phys.*, **42**, 5891 (1971).
[2] S. Iijima and J.M. Cowley, *Z. Naturs.* **27a**, 445 (1972).
[3] H.T. Pearce-Percy and J.M. Cowley, *Optik*, **44**, 273 (1976).
[4] D.J. Smith, J.C. Barry, L.A. Bursill, A.K. Petford, and J.C. Wheatley, *JEOL News*, **24E**, 2 (1986).



**Regents Professor David J. Smith**
Department of Physics, Arizona State University,
Tempe, Arizona

Chairman Yoshiyasu Harada

# Marking Our 60th Anniversary

JEOL was established in June 1949 for the development, production and sales of transmission electron microscopes. This year, JEOL has marked its 60th anniversary.

The JEOL Group has grown in size reaching sales of 100 billion yen and a workforce of about 3000 employees through the corporate activities for 60 years, owing to the efforts of all the predecessors and all the employees of the JEOL Group. I would like to appreciate and celebrate that JEOL has reached its 60th anniversary. Furthermore, I am deeply aware that our long corporate development is primarily due to the many customers who have continually supported and guided us. On this occasion, I would like to express my heartfelt appreciation to all of our customers.

When JEOL marked its 50th anniversary, positioning the 50th anniversary as the second inauguration of the JEOL Group, we announced the JEOL Group's new long-term management vision, "JEOL SPIRIT-1." This vision set forth the direction in which JEOL should head in the first decade of the 21st century. In this vision, two key concepts are stipulated: The first is to situate our main business domains as "Twin Core," which consists of the Scientific Instrument business and the Industrial Equipment business. The second is to pursue three missions of "No.1 Solution," "Global Network," and "Innovation." Based on this long-term management vision, we formulated medium-term management plans every three years, and divided these three-year plans into annual business plans. In line with the management vision, we will continue to change our mindset to push forward with customer-oriented business.

Since its establishment 60 years ago, the JEOL Group has been marketing a broad range of products worldwide. These products are essential for basic research including materials science and life science and for technological development and quality control in various industries. We are determined to continue to meet the expectations of our customers. For example, the transmission electron microscope, which was the starting point of JEOL, is a flagship of JEOL even now. Our electron microscopes incorporate many technological innovations in recent years, such as aberration correction, tomography, specimen cooling, phase-plate microscopy, specimen-environment control, and nano-level analysis. Thus, as high-end basic research tools, JEOL electron microscopes are widely utilized in universities, national laboratories and corporations all over the world.

The world economy is now in recession, so we have all the more need to create new technologies and industries. I believe that the JEOL group is an indispensable enterprise for implementing science and technology policies and for developing industries in the world.

According to our company philosophy, we will continually contribute to the progress of science and society around the world by enhancing the competitiveness of our products. Finally, I sincerely hope for your candid evaluations and warm assistance.

**Yoshiyasu Harada**
Chairman, JEOL Ltd.

President Gon-emon Kurihara

# Aiming for Best Total Solutions

In May 1949, not long after the end of World War II, Japan Electron Optics Laboratory (forerunner of JEOL) was established for the development of transmission electron microscopes. Since then, our company has been supported by many people around the world, and this year JEOL has marked its 60th anniversary. On this occasion, I would like to express my sincere appreciation to all of you.

Progress of science and technology in these 60 years has been outstanding. During this period, JEOL has developed and marketed a number of Scientific Instruments and Industrial Equipment to meet the expectations of our customers. Now our products are playing a significant role in a broad range of fields, which include transmission and scanning electron microscopes, analytical instruments such as electron probe microanalyzers, nuclear magnetic resonance spectrometers, mass spectrometers and X-ray spectrometers, electron beam lithography systems for semiconductor-device fabrication, electron beam sources for industrial use, and clinical biochemistry analyzers.

Our company philosophy states, “On the basis of “Creativity” and “Research and Development”, JEOL positively challenges the World’s highest technology, thus forever contributing to the progress in both Science and Human Society through its products.” Our primary mission is to develop state-of-the-art products that reflect the needs of the worldwide market and timely supply the products to the customers. For as many as 60 years, although the market environment surrounding our company has greatly changed, JEOL has expanded its business to the markets of inspection and metrology businesses such as environmental-, medical- and semiconductor-use, through our traditional products of Scientific Instruments centered on electron microscopes.

However, I recognize that in the midst of a global change at present, what JEOL should focus on is to provide the best total solutions to the customers so that they feel the greatest satisfaction until the high-end instruments supplied by JEOL reach lifetime. In order to realize this objective in a more efficient manner, JEOL DATUM, which has long been engaged in maintenance service of JEOL products, will be merged to JEOL this July. Utilizing this change, we will respond to the requests from the customers through sophisticated solutions, which only JEOL can offer. To achieve this, in addition to conventional maintenance service, we will further pursue in providing up-to-date technological applications and kowhow, and in swiftly carrying out inspection of the installation room of your JEOL instrument and measurement of your samples. Moreover, we position the publication of *JEOL News* as one of providing solutions, so we will continue to make efforts to enhance the content of *JEOL News*.

At the time of our 60th anniversary, we are determined to continually strive to provide the best products and solutions to you by keeping our mindset in a global perspective. Finally, I sincerely hope for your candid evaluations and warm assistance.

**Gon-emon Kurihara**
President, JEOL Ltd.

JEOL news

Volume 44 Number 1
June, 2009

# Exit Wavefunction Reconstruction

†A. I. Kirkland and S. J. Haigh

Department of Materials, University of Oxford

Indirect methods for improving the resolution attainable in the TEM *via* image reconstruction of focal or beam-tilt series of images are now realising the promise they have long offered. This technique simultaneously recovers the complex specimen exit plane wavefunction and fully compensates for all measurable lens aberrations. Using an aberration corrected TEM and a tilt azimuth data acquisition geometry it can be shown that electron optical aberration correction and exit wave reconstruction enables the recovery of super resolved information beyond the axial information limit. In many cases the resolution improvement achievable is now limited by the sample and not by instrumental parameters.

## Introduction

High Resolution Transmission Electron Microscopy (HRTEM) is now firmly established as one of the most important tools available for studies of the local microstructure and chemistry of a wide range of materials [1]. However, HRTEM records only the real valued image intensity, resolution limited by effects due to the partial spatial and temporal coherence of the illumination. This leads to an absolute information limit under axial illumination conditions of typically 100 times the wavelength for uncorrected instruments and 40 times the electron wavelength for the current generation of intermediate voltage corrected microscopes.

Indirect reconstruction of the complex wavefunction at the exit surface of the specimen (see [2] for a review) provides an attractive (but necessarily indirect) route to obtaining quantitative structural information with improved signal to noise characteristics at resolutions equal to or greater than those that can be achieved in conventional images.

The experimental datasets required for the successful implementation of this approach comprise several conventional HRTEM images recorded at either varying defocus levels [3-10] or with different illumination tilt directions [11-13]. Either of these acquisition geometries provides a set of differently aberrated images that contain independent information about the specimen exit plane wavefunction and the latter can subsequently be computationally recovered from the overdetermined dataset. For this latter step, substantial progress has been made on the theoretical and computational problem of eliminating the non-linear image intensity components [4] and in the fully automated measurement of the aberration coefficients [14-16].

In 1997 initial results from TEM instruments fitted with electron optical elements designed for direct correction of otherwise unavoidable spherical aberration [17, 18] were announced. Commercial versions of these prototype instruments using an arrangement of sextupole elements and round lens transfer doublets have since been constructed, capable of direct correction of the coefficients in the wave aberration function to third-order and providing resolutions below 0.1nm at intermediate voltages. At the time of writing initial results from second-generation corrected electron optical systems capable of fifth-order correction have been reported [19, 20] targeting a resolution of 50 pm.

Focal and tilt series reconstruction methods have the advantage of recovering the fully complex specimen exit plane wavefunction, compensated for all measured objective lens aberrations. This data can also be retrieved using related approaches such as high resolution holography [21], diffractive imaging [22] and ptychography [23] in which a micro-diffraction pattern (from a very small area of the specimen) is recorded quasi-continuously as the illuminating probe scans the specimen. This additional data compared to that available in single HRTEM images allows structural inferences about the specimen to be made by comparison of experimentally recovered and simulated wave functions for trial structures with only one unknown experimental parameter (the specimen thickness). Thus, exit wavefunction restoration in all

†Parks Road, Oxford, OX110ES, UK.

Email: angus.kirkland@materials.ox.ac.uk

## Contents



**Cover micrograph**

Restored phase of a 6-nm Pt particle obtained by applying spherical aberration correction and through-focus exit wavefunction restoration to a defocus series of 20 images acquired at 200 kV with the coefficient of spherical aberration, Cs, adjusted to –30 μm. (See page 9)
This micrograph is reproduced with permission from Angew. Chem. (Int. Ed.) Vol 46, p3683, 2007. Copyright Wiley-VCH Verlag GmbH & Co. KGaA.

Courtesy of Professor A. I. Kirkland, Department of Materials, University of Oxford.

modes provides more quantitative structural information. Finally, as will be described subsequently there has been recent progress in combining electron optical correction and exit wavefunction reconstruction in which the former brings significant benefits to the resolution enhancement offered by the latter.

## A Historical Overview

The first recorded reference to exit wavefunction reconstruction was provided by Schiske [24] although the use of tilted illumination in an optical analog was suggested as long ago as 1873 by Abbe [25]. However, successful experimental efforts were hampered until relatively recently by several factors. Firstly, at all resolutions the largely uninterpretable non-linear components of the image intensity, which increase with specimen thickness, required the development of new reconstructions algorithms [4]. Secondly, the largely uninterpretable image intensity arising from inelastically scattered electrons by any mechanism other than phonon scattering (which it should be noted do not affect Gabor holography) required the development of imaging filters [26-28]. Thirdly the range of directions and energies in the illuminating beam (formulated as the partial spatial and temporal coherence), imposes a resolution limit on the image signal more stringent than that due to the lens aberrations which required the development of new electron sources [29, 30]. Finally, the increased availability of CCD detectors for digital image recording has made it far easier to record the sets of images needed for wave function reconstruction [31, 32].

Field-emission electron sources provide much higher coherence levels than were previously available with thermionic emitters and have provided images with higher spatial frequencies, so that focal series reconstruction in particular achieves resolution significantly beyond the limit imposed by coherent objective lens aberrations. However, the price for this is a much wider point response, meaning heavy delocalisation of image detail, and making it essential to use comparatively large field, high resolution electron detectors. The availability of these instrumental developments was utilised in the 1990s within a Brite Euram project that aimed to develop exit wavefunction reconstruction using both Gabor Holography and focal series datasets. The results from this provided the first experimental examples of exit wavefunction reconstructions at high resolution and also initiated the development of the parabaloid reconstruction method [6] which, although not optimal in its suppression of the non-linear imaging components provides useful physical insight into the reconstruction process.

Exit wavefunction reconstruction using tilted illumination requires that the primary beam is placed close to one side of an objective aperture. This allows it to interfere with beams scattered within the aperture at up to twice the maximum angle compared to the axial imaging mode, albeit eliminating beams scattered with different azimuths completely so that information must be combined from several images recorded with different tilt azimuths. However, for an optimum choice of tilt angle, the imaging properties of this mode compare favourably with those of the axial mode, and can achieve (in principle) a doubling of the resolution [12]. Since this approach synthesises a large effective Fourier space aperture from several smaller ones, it has also been termed 'aperture-synthesis' for comparison with similar established approaches in radio astronomy [33, 34] and radar [35]. Experimentally, exit wave reconstruction from tilt series datasets required the solution of two substantial technical problems in image analysis, *a posteriori* determination of the objective lens aberrations, including the beam tilt and mutual registration of differently aberrated images [11, 13] but was also demonstrated experimentally during the late 1990s [11, 13].

## Outline Theory for Exit Wavefunction Reconstruction

The wave leaving an object for monochromatic, axial illumination can be separated into scattered and unscattered components as:

$$\Psi_o(\mathbf{x}) = 1+\Psi_{so}(\mathbf{x}) \quad \text{.....(1)}$$

with the recorded image plane intensity given by:

$$I(\mathbf{x}) = |\Psi_{si}(\mathbf{x})|^2 = 1+\Psi_{si}(\mathbf{x}) + \Psi^*_{si}(\mathbf{x}) + |\Psi_{si}(\mathbf{x})|^2 \quad \text{..(2)}$$

Where $\Psi_{si}(\mathbf{x})$ is the electron wave in the real space image plane. If it is assumed that the scattering is sufficiently weak to ignore the quadratic term in (2) then the Fourier Transform of the image contrast is given as

$$c(\mathbf{k}) = \psi_{si}(\mathbf{k}) + \psi^*_{si}(-\mathbf{k}) \quad \text{.....(3)}$$

Where $\psi_{si}$ is the electron wave in the Fourier space image plane and $\psi^*_{si}$ it's complex conjugate. The Fourier transforms of the object and image waves are related by a wave aberration function $\gamma(k)$ and thus

$$\psi_{si}(\mathbf{k}) = \psi_{so}(\mathbf{k})w(\mathbf{k}) \quad \text{.....(4)}$$

where:

$$w(\mathbf{k}) = \exp\{-i\gamma(\mathbf{k})\} \quad \text{.....(5)}$$

Hence in terms of the object wave, $\psi_{so}(\mathbf{k})$, the Fourier Transform of the image contrast can be rewritten as

$$c(\mathbf{k}) = \psi_{so}(\mathbf{k})w(\mathbf{k}) + \psi^*_{so}(-\mathbf{k})w(-\mathbf{k}) + n(\mathbf{k}) \quad \text{....(6)}$$

in which the term $n(\mathbf{k})$ represents the observed noise in the image.

All reconstructions now require an estimate, $\psi'_{so}(\mathbf{k})$ of $\psi'_{so}(\mathbf{k})$ given a set of observed image contrast transforms, $c_i(\mathbf{k})$ and a knowledge of their individual transfer functions, $w_i(\mathbf{k})$. Therefore given data from several differently aberrated images, an *optimum* solution for $\psi'_{so}(\mathbf{k})$ can be defined in various ways [12]. In particular, a Wiener filter

applied to a focal or tilt series of images in the presence of noise gives an optimal estimate of the reconstructed wavefunction, expressed in the form of a weighted superposition of the image transforms as

$$\psi'_{so}(\mathbf{k}) = \sum_i \gamma_i(\mathbf{k}) c_i(\mathbf{k}) \quad \text{.....(7)}$$

where, the *restoring filters*, $\gamma_i(\mathbf{k})$, depend on the complex wave transfer functions $w_i(\mathbf{k})$for a set of images as

$$\gamma_i(\mathbf{k}) = \frac{W(-\mathbf{k}) w^*_i(\mathbf{k}) - C^*(\mathbf{k}) w_i(-\mathbf{k})}{W(-\mathbf{k}) W(\mathbf{k}) - |C(\mathbf{k})|^2 + \upsilon(\mathbf{k})} \quad \text{.....(8)}$$

$$W(\mathbf{k}) = \sum_i |w_i(\mathbf{k})|^2; C(\mathbf{k}) = \sum_i w_i(\mathbf{k}) w_i(-\mathbf{k}) \quad \text{..(9)}$$

For all the opacity of this expression, in the case of reconstruction using series of images the effect on a Fourier component transmitted by only a single image is simply to retain it after division by the corresponding transfer function, and for components present in all images to average the estimates obtainable from any pair of differently aberrated images. For a component not transferred in any image the value of the filter tends to zero due to the inclusion of the noise to object power ratio, $\upsilon(\mathbf{k})$. In the final step of the overall reconstruction process the exit-plane wavefunction itself is obtained simply by inverse transformation.

The approach to exit plane wavefunction restoration outlined above assumes linear imaging. Alternative methods have also been developed for the more general case, including the non-linear contributions to the image intensity. In the original implementation the non-linear image reconstruction was tackled by matching the electron wave to the measured intensities of images by minimization of a least squares functional (the multiple input maximum a posteriori, (MIMAP)). The improved, maximum likelihood (MAL) description [4] provides a computationally efficient, numerically optimized recursive solution and explicitly includes the coupling between the exit wave and its complex conjugate.

## Experimental Exit Wavefunction Reconstruction

The theories outlined in the previous section can be applied equally to wavefunction reconstructions using either focal or tilt azimuth datasets. However these two geometries differ in their experimental advantages. In the case of a focal series reconstruction the use of a high coherence source to extend the microscope information limit is essential to maximise resolution enhancement. However, in the case of the tilt azimuth geometry it is the displacement of the transfer function envelope relative to the primary beam which is the essential element in achieving higher resolution, without explicitly requiring a high coherence source [11, 13]. The use of a high coherence source still offers benefits to the latter geometry in the accurate determination of the imaging conditions and to date, all experimental restorations have utilised instruments fitted with field emission sources. However, overall, the tilt azimuth geometry is less sensitive to errors in the determination of the aberration coefficients and provides somewhat better recovery of low spatial frequencies. Set against these advantages image registration is simpler for focal series where the correlation peaks are centrosymmetric between all members of the dataset, which is not the case for images recorded at different illumination tilts. Finally, tilt azimuth reconstruction is potentially limited by parallax effects (see later) which are absent in focal series datasets, a factor that is ultimately limiting at extremely high resolution. As an early illustration of this approach, **Figure 1** shows the first reported example of a successful tilt series reconstruction in 1995 [11] using an uncorrected JEOL JEM-2010F in which the interpretable resolution has been improved from 0.23 nm to 0.14 nm.

## Exit Wavefunction Reconstruction with Aberration Corrected Images

Direct electron optical correction [17, 18] offers the advantage that it may be achieved on line in a single image, with no requirement for post acquisition processing or acquisition of extended focal or tilt azimuth series. However, for HRTEM imaging current generation electron optical correctors are only able to correct aberrations to third order in the wave aberration function with partial compensation of selected higher order terms for real recorded image data. Thus, for aberration corrected instruments computational reconstruction is still beneficial for both focal and tilt series data acquisition geometries as it both compensates for higher order terms and recovers the complex specimen exit surface wavefunction.

Indirect and direct correction / compensa-

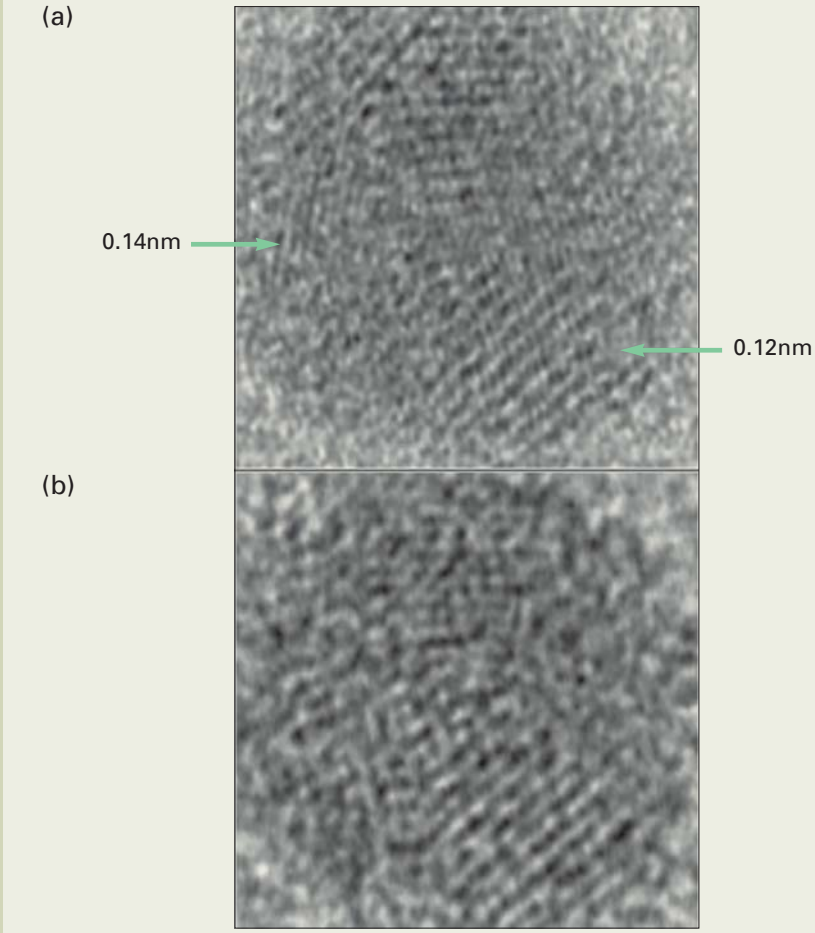


Fig. 1 (a) Modulus of the exit wavefunction of a gold nanoparticle reconstructed from a 4 member tilt series of uncorrected images with 0.14 and 0.12 nm fringes marked. (b) Original axial image recorded at the Scherzer defocus (200 kV, $C_s$ = 0.5 mm).

tion have been used in combination [36, 37] and this provides additional advantages. For focal series datasets, the elimination of tilt-induced coma relaxes the requirement of using parallel illumination and enables the illumination to be converged onto the specimen area of interest. Thus, current density at the sample may be maintained while reducing the emitter current thereby giving a reduced energy spread in the illumination (for a Schottky source) and providing an improved information limit. For a tilt series dataset, the elimination of tilt induced axial coma gives rise to a less critical focus conditioning for any given tilt magnitude and multiple tilt magnitudes are also possible without a large induced focus change. For either data acquisition geometry, the reduced delocalisation of image components in electron optically corrected images is advantageous in quantitative interpretation. Finally, in aberration corrected instruments the voltage centre and axial coma free axis are coincident and hence the temporal coherence envelope is symmetric and localized.

To illustrate the potential benefits from a combined direct / indirect approach to aberration correction and compensation **Figure 2** shows the phase of the specimen exit surface wavefunction of a Pt catalyst nanoparticle, viewed close to a <110> direction, reconstructed from a focal series of aberration corrected images acquired using a JEOL JEM-2200FS. Despite the presence of a graphitic carbon support, terraces and steps around the edge of the particle are visible and moreover, the visibility and spatial resolution within these features are improved significantly compared to a conventional HRTEM image. The monatomic steps that are visible in Figure 2(a) are conventionally termed *A* or *B* type, with either {100} or {111} microfacet atomic risers that have potentially different catalytic properties. Due to computational inversion of the HRTEM imaging process the heights of the peaks in the recovered phase are related to the number of atoms in each atomic column and can thus be used to obtain information about the local atomic arrangement of each surface in cross section. Detailed examination of these provide evidence that the outermost atomic layers consist of irregular islands of atoms, in contrast to the atomic arrangements that have been proposed on the basis of homoepitaxial growth experiments on extended Pt surfaces [38].

**Figure 3** emphasises the resolution improvement obtained by recovering the specimen exit wavefunction compared to that present in a single HRTEM image. The power spectra shown below each image in Figure 3 clearly show the presence of higher-spatial resolution lattice fringe information in the reconstruction and equally importantly, the decreased contribution to the power spectrum from the quasi-amorphous carbon support.

Our next example demonstrates experimental verification of the resolution improvement possible using aberration corrected tilted illumination images. This requires a specimen with a real space lattice separation

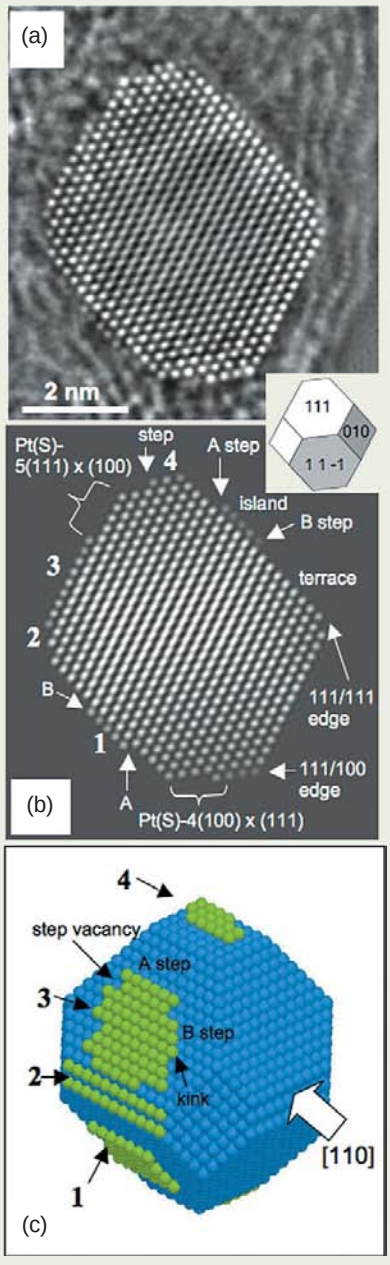


Fig. 2 (a) Phase of the reconstructed wavefunction of a 6-nm Pt particle obtained by applying spherical aberration correction and focal series exit wavefunction reconstruction to a dataset of 20 images acquired at 200 kV with a spherical aberration of -30 µm. (b) Best-fitting simulated phase. (c) Three-dimensional atomic model used to calculate the best-fitting phase in (b). The large white arrow indicates the direction of the electron beam. The inset overlapping parts shows the crystallographic details of the particle. In parts (b) and (c) labels 1-4 correspond to the same features on the surface of the particle. The notation Pt(S)-n(x,y,z)K(u,v,w) refers to the microfacets, for which n is the number of atoms in the terrace, (x,y,z) is the Miller index of the terrace, and (u,v,w) is the Miller index of the step.

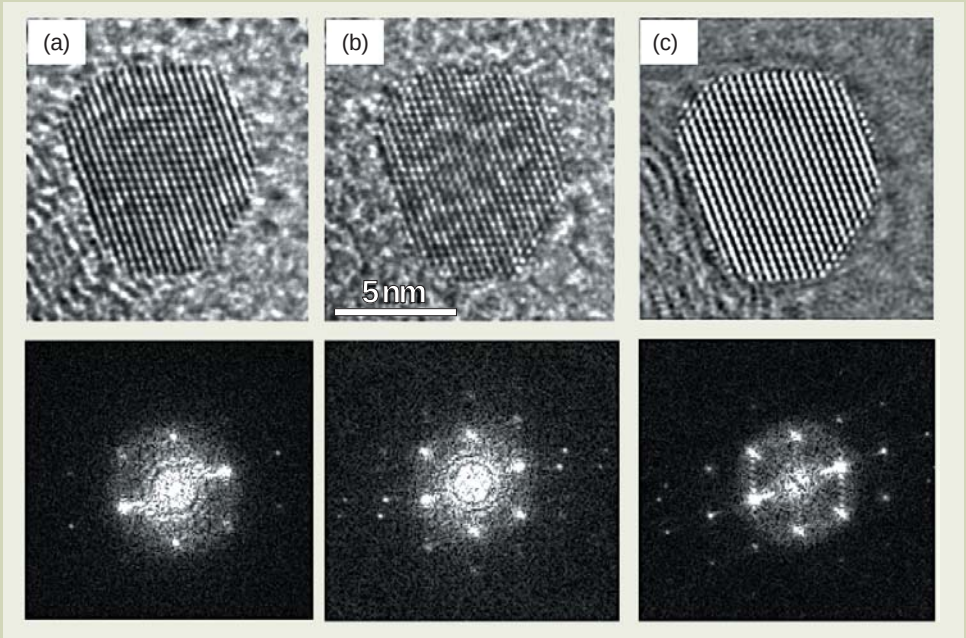


Fig. 3 (a) and (b) HRTEM (intensity) images of the Pt particle shown in Fig 2(a), acquired with the spherical aberration adjusted to 0.5 mm (a) and -30 µm (b). Corresponding power spectra are shown beneath each image. (c) Phase and power spectrum of the same particle, obtained by applying exit wavefunction reconstruction to a focal series of aberration corrected images.

beyond the axial information limit and a gold foil oriented along a <123> direction satisfies this requirement. **Figure 4** compares the phases and moduli of exit wavefunctions restored using both focal series and tilt defocus data sets. The only detail present in the phase and modulus of the exit wavefunction (Figures 4 (a) and (b)) recovered from the focal series dataset relates to the {111} planes, which have a 0.235 nm lattice spacing. In contrast, the wavefunction recovered using tilted illumination data contains information at the positions of the {331}, {420} and {242} lattice reflections, corresponding to spacings of 0.093 nm, 0.091 nm and 0.083 nm which are beyond the 0.1nm axial information limit of the microscope used.

As a final example we compare exit wavefunction reconstruction directly, now using focal and tilt series image datasets of images of thin crystals of <111> oriented $SrTiO_3$. **Figure 5** clearly shows the improvement in information transfer that can be obtained using a tilt-series data set for exit wavefunction reconstruction in which information transfer at 10% corresponding to a resolution of 0.12 nm is present for the focal series reconstruction, whereas the same level of information transfer limit is extended to 0.08 nm in the tilt-series reconstruction.

Although the data presented in this section clearly demonstrates that a combination of direct aberration correction and exit wave reconstruction is advantageous and moreover, that a tilt azimuth acquisition geometry enables super resolution, it is useful to examine in detail the limiting factors in this approach.

At large beam tilt magnitudes partial temporal coherence causes a loss of transfer at the centre of the tilted transfer function. For a beam tilt, $\tau_0 = \lambda \mathbf{k}_0$, beams at the same angle $\tau_0$ with respect to the tilt axis are perfectly transferred and the temporal coherence envelope has no effect. However, for larger beam tilts the transfer falls away significantly inside this ring of perfect transfer (the achromatic circle). Reducing the tilt angle prevents this central transfer loss but reduces the resolution improvement compared to the axial case. This reduction in transfer for tilted illumination can in principal be recovered in the final reconstruction either by increasing the number of azimuthal angles or by including more than one tilt magnitude. However, either of these approaches increases the number of images required with consequent implications for experimental stability and overall radiation dose.

The second limiting factor is given by the variation within the experimentally measured axial aberration coefficients as a function of illumination tilt which can be estimated by taking the real part of the expansion of the wave aberration function with respect to the complex aberration coefficients and illumination tilt angle [39].

Finally, in contrast to exit wavefunction reconstruction using focal series data the individual images within a tilt series data set are not simply different measurements of the same projected specimen potential. Under tilted illumination the specimen potential is projected along a slightly different direction compared to the axial case and this introduces an additional phase shift in an image which can be estimated using a simple geometric parallax model. Choosing a maximum phase variation for a resolvable distance, $d$ as $\pm\pi/2$, the maximum parallax allowed between the top and bottom specimen surfaces relative to the middle of the specimen is d/4. For a beam tilt, $\tau$, this leads to a maximum specimen thickness of $d/(2\tau)$. The simple geometric parallax argument described above is independent of the imaging conditions but has been found to be more stringent than the limit determined from a full dynamical calculation [40].

These various limits for wavefunction reconstruction using tilted illumination images are summarised in **Table 1.** This clearly demonstrates that the aperture synthesis approach to exit waveunction reconstruction can use larger tilt magnitudes under aberration corrected imaging conditions, giving rise to the possibility of greater resolution improvement, significantly beyond the axial information limit of the microscope. However at very high resolution, parallax considerations become increasingly significant leading to a new regime where the sample limits the resolution attainable in tilt series exit wavefunction reconstruction.

## Conclusions

In this paper we have highlighted the development and application of exit wavefunction reconstruction in the TEM as a method for obtaining higher resolution, quantitative structural data using focal or more particularly, tilt azimuth series of images. We have also demonstrated the use of this technique in studies of nanocrystalline metal catalyst particles where local surface structures can now be described with atomic precision. Finally we have outlined the recent use of a combination of electron optical aberration correction and exit wavefunction reconstruction in a complimentary approach that further improves attainable resolution and have summarized the ultimate instrumental and specimen- based limitations to this.

## Acknowledgment

It is a pleasure to contribute this paper to *JEOL News* on the occasion of JEOL's 60th anniversary. AIK would like to acknowledge Drs W. O. Saxton, R. R. Meyer, L. Y. Chang, H. Sawada, M. Kawasaki, K. Tsuno and F. Hosokawa for their substantial contributions to the development of exit wavefunction reconstruction and aberration measurement. We

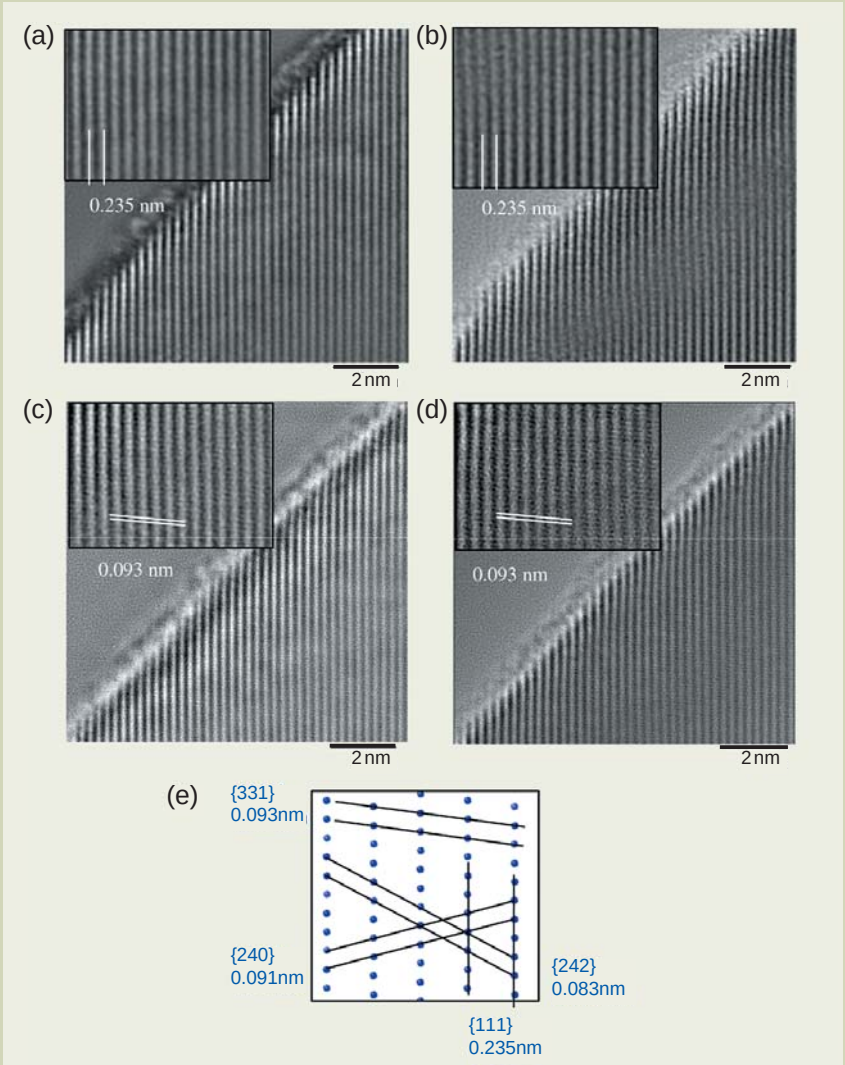


Fig. 4 Exit wavefunctions recovered from a gold foil oriented along a <123> direction. (a) and (b) phase and modulus restored using a 16 image focal series with a focal step of 7 nm. (c) and (d) phase and modulus of the same specimen area restored from a 27 image tilt-defocus data set with a maximum tilt magnitude of 18.4 mrad. (e) The atomic structure of gold projected along a <123> direction with lattice planes indicated.

would also like to acknowledge Dr Y Harada and M Hepburn from JEOL Ltd. and JEOL UK Ltd. respectively, together with other colleagues from these organisations for their continued enthusiastic support of research in advanced electron microscopy at Oxford.

## References


[1] A. I. Kirkland, J. L. Hutchison Chapter 1 (pp3-64) in 'The Science of Microscopy' Eds. P. W. Hawkes and J. Spence, Kluwer Press, 2007 )(2nd edition 2009).

[2] A. I. Kirkland, R. R. Meyer, L. Y. Chang, *Microscopy and Microanalysis*, **12(6)**, 461, (2006)

[3] W. Coene, G. Janssen, M. Op de Beeck, D. van Dyck, *Phys. Rev. Letts* **69,** 3743, (1992)

[4] W. M. J. Coene, A. Thust, M. Op de Beeck and D. van Dyck, *Ultramicroscopy*, **64,** 109, (1996)

[5] D. van Dyck and M. Op de Beeck, *Ultramicroscopy*, **55,** 435, (1994)

[6] M. Op de Beeck, D. van Dyck and W. Coene, *Ultramicroscopy* **64,** 167, (1996)

[7] D. van Dyck D. and W. Coene, *Ultramicroscopy* **15,** 29, (1984)

[8] A. Thust, W. Coene, M. Op de Beeck and D. van Dyck, *Ultramicroscopy*, **64,** 211, (1996)

[9] A. Thust, M. Overwijk, W. Coene and M. Lentzen *Ultramicroscopy*, **64,** 249, (1996)

[10] M. Lentzen, B. Jahnen, C. L. Jia, A. Thust, K. Tillmann and K. Urban, *Ultramicroscopy*, **92,** 233,(2002)

[11] A. I. Kirkland, W. O. Saxton, K. L. Chau, K. Tsuno, M. Kawasaki, *Ultramicroscopy*, **57,** 355, (1995)

[12] W. O. Saxton. (pp213) in " Image and Signal Processing in Electron Microscopy, Proc. 6th Pfferkorn Conf., Niagara", Scanning Microscopy International Eds. P. W. Hawkes, F. P. Ottensmeyer, W. O. Saxton and A Rosenfeld A., (1988)

[13] A. I. Kirkland, W. O. Saxton and G. Chand, *J. Electron Microscopy*, **1,** 11, (1997)

[14] F. Zemlin, K. Weiss, P. Schiske, W. Kunath and K. H. Herrmann, *Ultramicroscopy*, **3,** 49, (1978)

[15] R. R. Meyer, A. I. Kirkland and W. O. Saxton, *Ultramicroscopy*, **92,** 89, (2002)


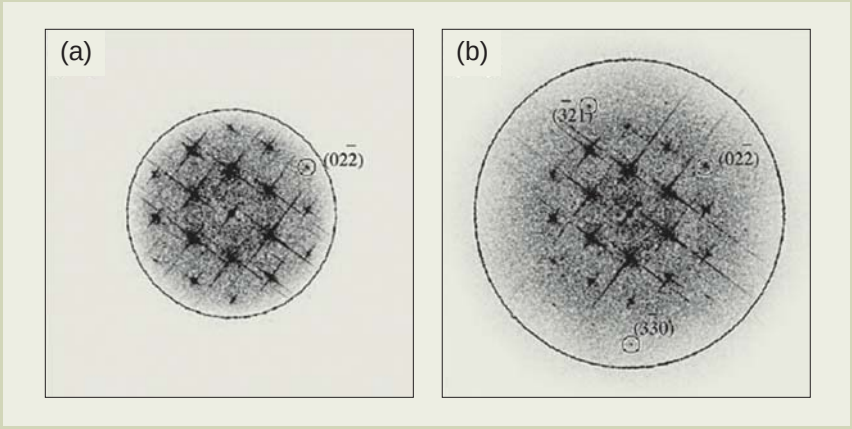


Fig. 5 Moduli of Fourier transforms of the complex specimen exit wavefunctions of <111> orientated $SrTiO_3$ reconstructed using (a) focal-series data and (a) combined tilt/focal-series data. Circles indicate the limit for which information transfer drops below 10%, equivalent to a spatial resolution of 0.12 nm for the focal series and 0.08 nm for the tilted data set. Selected high-order reflections are highlighted to emphasize the presence of additional information in the exit wavefunction recovered from the tilt/focal-series data compared to the axial focal series data. Experimental focal series comprised 20 images separated by a focal increment of 10 nm with the series centered at the Gaussian focus with a spherical aberration of -3 μm. Tilt series consisted of six short focal series taken at different illumination tilt directions using tilt magnitudes of up to 20 mrad.

Table 1 Tilt limits determined for an object thickness of 2 nm at 200 kV assuming third order aberration correction and a focal spread = 4 nm.

| Limiting Factor | Maximum Tilt Magnitude | Resolution Limit |
|---|---|---|
| Incoherent Aberrations | 19 mrad | 0.0629 nm |
| Coherent Aberrations | 25 mrad | 0.0547 nm |
| Geometric Parallax | 18 mrad | 0.0645 nm |


[16] R. R. Meyer, A. I. Kirkland and W. O. Saxton, *Ultramicroscopy*, **99,** 115, (2004)

[17] M. Haider, H. Rose, S. Uhlemann, B. Kabius and K. Urban, *Nature* **392,** 768, (1998)

[18] M. Haider, H. Rose, S. Uhlemann, B. Kabius and K. Urban, *J. Electron Microsc.* **47,** 395, (1998)

[19] C. Kisielowski, B. Freitag, M. Bischoff, H. van Lin, S. Lazar, G. Knippels, P. Tiemeijer, M. van der Stam, S. von Harrach, M. Stekelenburg, M. Haider, H. Muller, P. Hartel, B. Kabius, D. Miller, I. Petrov, E. Olson, T. Donchev, E. A. Kenik, A. Lupini, J. Bentley, S. Pennycook, A. M. Minor, A. K. Schmid, T. Duden, V. Radmilovic, Q. Ramasse, R. Erni, M. Watanabe, E. Stach, P. Denes, U. Dahmen, *Microscopy and Microanalysis* **14,** 454, (2008)

[20] H. Sawada, F. Hosokawa, T. Kaneyama, T. Ishizawa, M. Terao, M. Kawazoe, T. Sannomiya, T. Tomita, Y. Kondo, T. Tanaka, Y. Oshima, Y. Tanishiro, N. Yamamoto and K. Takayanagi, *Jpn. J. Appl. Phys.* **46,** L568-L570, (2007)

[21] M. Lehmann, H. Lichte, D. Geiger, G. Lang and E. Schweda, *Materials Characterisation*, **42,** 249, (1999)

[22] J. M. Zuo, I. Vartanyants, M. Gao, R. Zhang, L. A. Nagahara, *Science*, **300**, 1419, (2003)

[23] P. D. Nellist, B. C. McCallum and J. M. Rodenburg, *Nature* **374,** 630, (1995)

[24] P. Schiske (pp82) *" Image Processing and Computer Aided Design in Electron Optics"*, Ed. P. Hawkes, London: Academic Press, (1973)

[25] E. Abbe, *Arkiv Mikroskopische Anat.*, **9,** 413, (1873)

[26] O. L. Krivanek, A. J. Gubbens, N. Dellby and C. E. Meyer, *Microsc. Microanal. Microstruct.* **3,** 187, (1992)

[27] H. Rose and E. Plies E, *Optik*, **40,** 336, (1974)

[28] K. Tsuno, T. Kaneyama, T. Honda, K. Tsuda, M. Terauchi and M. Tanaka, *J. Electron Microscopy*, **46,** 357, (1997)

[29] M. T. Otten and W. M. J. Coene, Ultramicroscopy, 48, 77, 1993.

[30] T. Honda, T. Tomita, T. Kaneyama and Y. Ishida, *Ultramicroscopy*, **54,** 132, (1994)

[31] J. Spence and J. Zuo, *Rev. Sci. Inst.* **59,** 2102, (1988)

[32] R. R. Meyer, A. I. Kirkland, R.E. Dunin-Borkowski, J. L. Hutchison, *Ultramicroscopy*, **85,** 9, (2000)

[33] F. G. Pease, Ergeb. Exakt. *Naturwiss.* **10,** 84, (1931)

[34] A. A. Michelson, *Phil. Mag.* **30,** 1, (1890)

[35] M. Ryle and D. Vonberg, *Nature* **158,** 339, (1946)

[36] L. Houben, A. Thust, K. Urban *Ultramicroscopy*, **106,** 200, (2006)

[37] L. Cervera Gontard, L.-Y. Chang, C. J. D. Hetherington, A. I. Kirkland, D. Ozkaya, and R. E. Dunin-Borkowski, *Angew. Chem.*, **46,** 3683, (2007)

[38] B. Lang, R. W. Joyner, G. A. Somorjai, *Surf. Sci.* **30,** 454, (1972)

[39] A. I. Kirkland, S. J. Haigh, H. Sawada, Phil. Trans. Proc Roy. Soc, in press (2009)

[40] R. R. Meyer, PhD Thesis, Dresden University, (2002)

# Single Shot Nanosecond Imaging in the Dynamic TEM

**James E. Evans, Geoffrey H. Campbell, Judy S. Kim, Thomas B. LaGrange, Bryan W. Reed, Mitra L. Taheri, and †Nigel D. Browning**

**Lawrence Livermore National Laboratory**

Directly observing dynamic processes that occur on the micro- and nanosecond timescale is not possible with conventional Transmission Electron Microscopes. The Dynamic Transmission Electron Microscope (DTEM) couples a pump-probe laser based experimental approach with the column of a conventional TEM to allow single shot imaging of dynamic events with nanosecond temporal and nanometer spatial resolution. This paper reviews the experiments that have been performed on the first-generation DTEM at Lawrence Livermore National Laboratory and describes future design improvements for a second-generation microscope aimed at future research plans in the area of biomolecular imaging.

## Introduction

Several technological advancements have improved the spatial resolution of Transmission Electron Microscopes (TEM) during the last decade [1], yet the temporal resolution of conventional in situ TEM observations has remained limited to video acquisition rates around 33 ms between frames. Therefore, the imaging of many dynamic processes and reactions on the micro- and nanosecond timescales has remained largely unexplored limiting our understanding of salient phenomena that control these processes and define the macroscopic material properties, e.g. rapid nucleation and growth events, coordinated atomic motion across interfaces, defect interactions, etc. The Dynamic Transmission Electron Microscope (DTEM) at Lawrence Livermore National Laboratory (LLNL) addresses this need by extending the temporal resolution of *in situ* TEM observations by six orders of magnitude. The nanosecond time resolution of the DTEM is achieved through the integration of pulsed laser systems with the TEM column and adopting a pump-probe experimental approach in which a material processes is initiated with a pump laser pulse and is subsequently analyzed with a photoemitted electron probe pulse using electron diffraction or real-space imaging [2].

The DTEM aims to capture an image of a reaction or structural change with a single pulse of electrons that is currently ~15 ns in duration. As such, the instrument is tuned to investigate irreversible reactions. This is in marked contrast to other ultrafast methods, such as Ultrafast Electron Diffraction (UED), which uses electron pulses on the order of 20 - 100 fs but does not obtain real-space images of the sample reacting and builds up the pattern from multiple electron pulses containing at most a few thousand electrons per pulse [3, 4]. Stroboscopic Ultrafast TEM (UFTEM) also uses femtosecond electron pulses to observe highly reversible processes such as electronic excitations but cannot image irreversible chemical or physical reactions [5-10].

The single-shot DTEM was originally pioneered by Bostanjoglo and coworkers [11]. Yet while their design was great leap forward for in situ microscopy, technical issues involved with producing high spatial resolution images with nanosecond pulses limited their attainable spatiotemporal resolution to around 200 nm at 10 ns. The primary challenge in this single shot approach for high spatiotemporal resolution imaging is generating a sufficient number of electrons during a single pulse to form an interpretable image. That is, the pulsed electron gun must be a high brightness source ($10^9$ A $cm^{-1}$ $steradian^{-1}$) and electron optical system must preserve this brightness. Additionally, an effort must be made to balance the number of electrons within a given pulse duration to achieve enough contrast for the signal to be detected, while attempting to mitigate the effect of space charge and statistical coulomb effects which cause blurring and degrade spatial resolution [12]. The DTEM developed at LLNL uses a modern TEM platform and novel gun design that produces a spatiotemporal resolution of less than 10 nm at 15 ns [15].

The design of the LLNL DTEM is based upon a modified JEOL JEM-2000FX containing an additional condenser lens (C0) directly beneath the electron gun and two integrated lasers to perform the pump-probe experiments using the single shot approach (**Figure 1**a). Briefly, a 1064 nm wavelength Nd:YAG drive laser pulse enters the column of the microscope through a modified analytical X-ray port and directly excites the sample to initiate a reaction. Depending on the absorption characteristics of the sample and desired process to be stimulated in the sample, the fundamental wavelength of the drive laser, using non-linear harmonic generation crystals, can be frequency converted to wavelengths of 532 or 355 nm. After a user-specified delay (Figure 1b), a frequency quintupled Nd:YLF laser pulse with a wavelength of 211 nm enters the column through a window in another added section beneath the C0 lens and excites an area of the photocathode [12]. Around $1\times10^9$ electrons are produced via photoemission as a single bunch with a FWHM duration of 15 ns and pass through the column to probe the sample as in a conventional TEM [15]. By recording an image of the sample prior to the initiating laser pulse, information about the transient and permanent changes occurring within the material during the reaction can be obtained. When several images with different delays between the pump and probe pulses are acquired, an evolutionary timeframe of the reaction can be constructed.

As conventional TEMs traditionally operate with a single electron in the column at any one time, this introduction of a very dense pulse of electrons can affect the performance of the DTEM for real-space imaging [12]. There is therefore a limitation for single shot

†Physical and Life Sciences Directorate, 7000 East Avenue, L-353, Livermore, CA, 94550, USA
Email: Evans80@LLNL.Gov

imaging that arises from space-charge effects within the electron beam and which degrade the spatial and temporal resolution due to Coulomb interactions. Stochastic blurring affects the spatial resolution due to irreversible and uncorrectable loss of information from random electron scattering events within the pulse while electron-electron repulsion will cause the electron bunch to expand temporally while traveling through the column (for very short pulses) and will limit the current density at the cathode (for longer pulses, via the Child-Langmuir effect) [20, 21]. The loss of resolution for both types of Coulomb interactions increases as the electron pulse duration decreases and can become a limiting factor at the picosecond timescale for the necessary electron fluence required for single shot imaging. Thus, not only does one have to combat the photocathode reaching saturation for certain pulse durations, the maximum fluence attainable for imaging is limited by the Coulombic interactions in the electron pulse as there will be a trade-off between brightness and resolution.

## Results

The DTEM is a unique and powerful tool for characterizing the dynamic processes occurring in material science samples and can operate in diffraction mode to observe phase transformations, or it can acquire real-space images showing the propagation of a reaction front through a thin foil and in situ growth of a nanowire via laser ablation. In these experiments, the wavelength of the sample drive laser used to initiate the reaction was optimized for the material being studied as was the delay between the pump and probe pulses. Although the resolution of the DTEM for a 15 ns probe laser pulse is limited due to the available brightness to around 8 nm in spatial resolution [15], there is enough dynamical contrast in the images to observe the same features in a single shot image as you would in a conventional TEM (**Figure 2**).

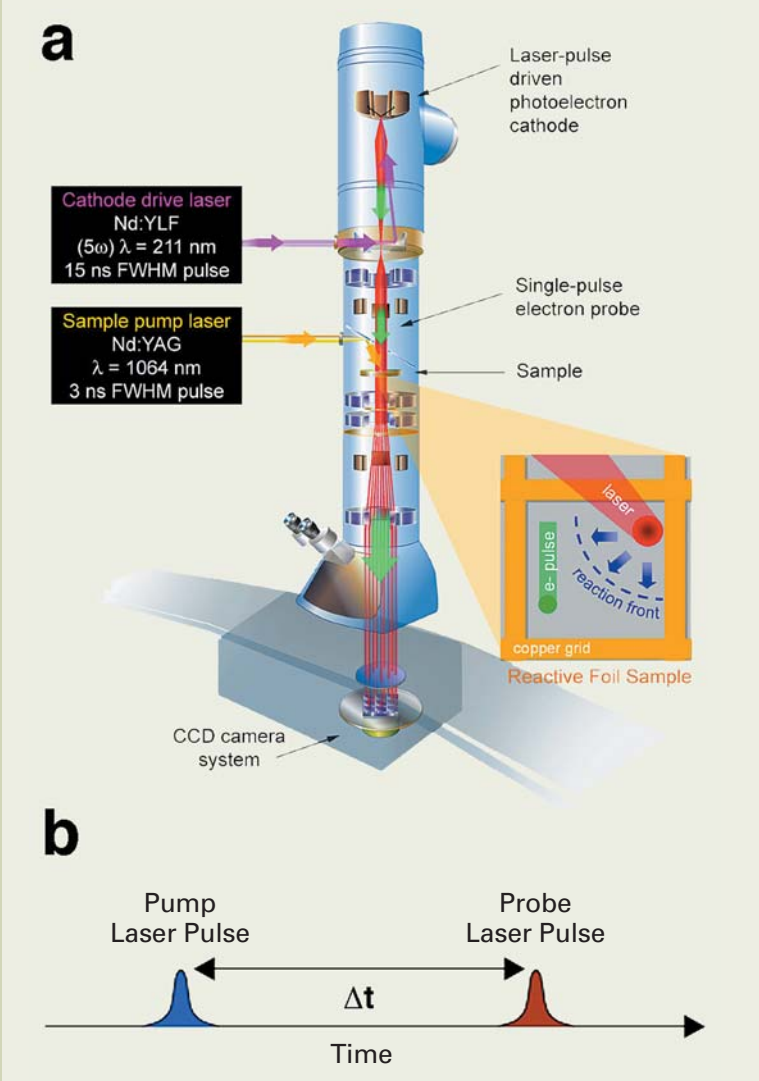


Fig. 1 Schematic of the DTEM. Two lasers enter the column of the TEM to provide the pump and probe pulses for the experiment (a). The sample drive laser initiates a reaction and after a user controlled delay, the cathode laser initiates photoemission from a photocathode. The resulting bunch of $10^8$–$10^9$ electrons traverse the column and image the sample. Depending on the experiment, the probe pulse can either be offset or centered directly over the pump pulse that initiates the reaction. Image adapted from [17]. (b) The temporal resolution of the DTEM is determined by the probe pulse duration. However, the pump-probe delay allows for analyzing the progression of a reaction at varying time points. The probe pulse duration is nominally set to 15 ns however the delay between the pump and probe pulses can be set directly by the user for each sample. Image adapted from [12].

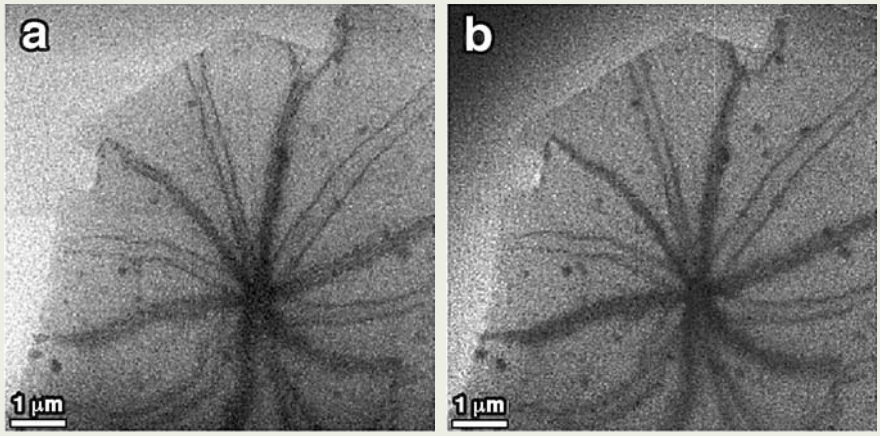


Fig. 2 Low magnification micrographs of secondary phase precipitates within a 6061 Al sample. Similar contrast information is present in both images acquired using conventional bright-field-TEM (a) and with a dynamic 15 ns single-shot probe pulse (b). Image adapted from [15].

One of the most striking discoveries made using the DTEM was found when studying reactive multilayer foils. After the pump pulse strikes a stacked array of alternating thin Ni and Al layers, the layers intermix and an exothermic reaction propagates until extinction via full mixing and intermetallic formation [17]. The DTEM was capable of observing the rate of the reaction by positioning the electron probe pulse at a specified distance (dependent on the temporal delay) from the initiating pulse and acquiring images of the moving reaction front. Surprisingly, these snapshots also recorded the first ever example of a transient structure traveling with the reaction front (**Figure 3**), which did not persist and are not observed in the postmortem analysis. These tendril-like extensions were characterized as regions of phase separation that disappeared 2-3 μs after the reaction front had passed [17].

Using the sample drive laser, it is possible to heat a sample to initiate a temperature driven reaction, whether that is through an annealing or oxidation process or a solid-to-liquid or solid-to-solid phase transformation. One such experiment was performed on thin foils of pure titanium. Upon heating above 882°C, a solid-to-solid diffusionless phase transformation occurs via a structural change from the HCP α-phase to the BCC β-phase [12]. By acquiring a series of selected area diffraction patterns using varying pump-probe delays (**Figure 4**), it was found that the grain size dictates the incubation time necessary for nucleation. This suggested that the grain boundaries were acting as defects and nucleation sites increasing the rate of the reaction for smaller initial grain sizes [12].

The DTEM has also been used to divulge the nucleation behavior during laser-induced crystallization of amorphous materials [16]. Due to the low optical contrast between the crystalline and amorphous phases limiting the ability to study the transformation with standard ultrafast optical techniques, there is little to no data on the crystallization kinetics of metallic glasses under pulsed laser irradiation. However, with the high time and spatial resolution capabilities of the dynamic transmission electron microscope (DTEM), the rapid nucleation events occurring from pulsed laser irradiation can be directly observed and nucleation rates can be quantified (**Figure 5**). With sufficient laser fluence, a single IR pulse can crystallize small areas of the film within 2 μs [16]. The crystallized volume fraction and morphology depend strongly on the laser energy, the spatial profile of the laser spot, and heat transport in the film. As compared to slower furnace and CW laser annealing, pulsed laser heating produces a dramatically different microstructure with observed crystallization rates being orders of magnitude higher than those predicted by extrapolation of kinetic data obtained from slow-heating crystallization experiments.

The DTEM is also capable of laser based in situ synthesis. The growth of nanowires by laser ablating a thin film sample of <111> Si coated with a 4 nm Au layer within the DTEM can be seen in **Figure 6**. The Au coating acts as a catalyst for the Si substrate and the synthesis was initiated by pulsing the 355 nm wavelength sample drive laser [18]. The nanowire growth occurred in the absence of additional gas or heat and was due solely to the controlled melting and ablation of the materials within the DTEM. This suggests that the DTEM can be used to characterize the morphology of materials as well as investigate new methods for nanomaterial synthesis.

## Discussion

To improve the spatial and temporal performance of the DTEM, future developments are planned for the design of a second-generation DTEM capable of both single shot and stroboscopic imaging. The incorporation of aberration correction, phase plate technology, and fiber-based back-illumination of the photocathode will increase the contrast and spatial resolution of the microscope to sub-nanometer level for a large range of temporal pulse durations [20]. Additionally, the incorporation of an arbitrary waveform generator for the laser system, multi-frame image series acquisition with a few tens of nanoseconds time delay between each frame and a CMOS frame grabber will increase the attainable temporal resolution allowing multi-frame movies of a single dynamic event to be recorded [20].

In addition to the experiments listed above, incorporating *in situ* holders for both gas and fluid environments will vastly expand the experimental regime of the DTEM. In such environmental cells, a reaction can be initiated by the absorption of laser energy to heat the sample directly, degrade a molecular species into substituent components or to activate a photo-switchable event. For example, by using an *in situ* fluid holder, one could observe the nucleation and growth of zinc sulfide nanoparticles by the ultraviolet laser pulsed decomposition of thioacetamide in the presence of zinc sulfate [22]. Upon completion, the zinc sulfide nanoparticles can be rinsed, dried and adhered to a holey-carbon TEM grid and placed inside the in situ gas holder for subsequent heating to 400°C in an oxygen atmosphere for annealing to obtain zinc oxide nanoparticles [23]. Observing the combined reactions would give insight to the nucleation, growth, melting and annealing characteristics at the nanoscale in gaseous and liquid environments.

The DTEM is likely to prove useful for biological experiments as well. Due to the ultrafast nature of the imaging event used with the DTEM, it may be possible to outrun some of the damage and sample charging issues that cause resolution loss [24]. By increasing the gun brightness and improving the temporal resolution of the microscope to transmitting the entire bunch of electrons through the sample before any beam induced damage occurs it might be possible to image radiation sensitive materials with electron doses similar to those currently used for non-radiation sensitive materials science samples. The inherent increase in contrast due to more probing electrons interacting with the sample would help improve the typical spatial resolution for biomolecular imaging. Other benefits for biomolecular imaging with the DTEM include the possibility of visualizing dynamic molecular reactions using ultrafast movie mode. Dependant on the beam sensitivity of the sample within a fluid cell environment, it may be possible to record up to 20 consecutive images of a single molecular assembly or interaction

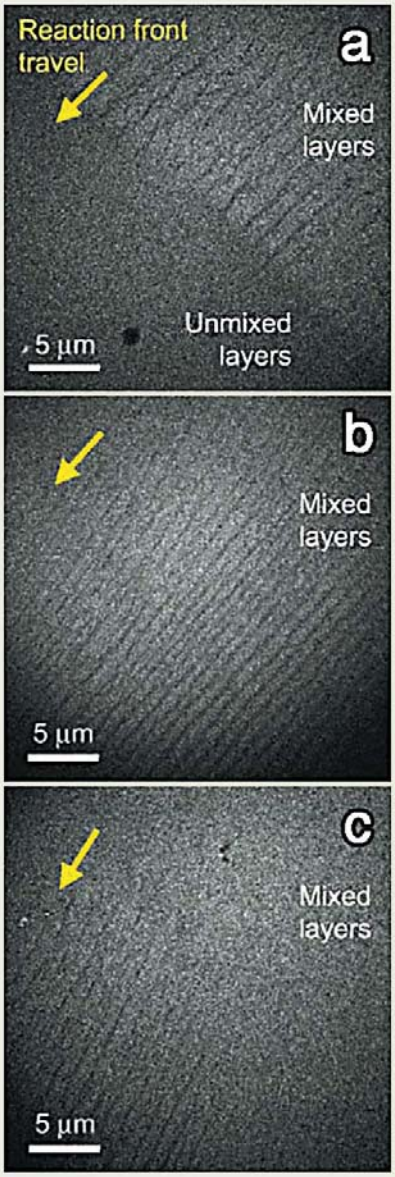


Fig. 3 Progression of a moving reaction front within a reactive multilayer foil of alternating Al/Ni layers as a function of time. A transient cellular morphology is observed traveling with the propagating front in (a). After an additional 2 μs the tendril like extensions are still present. However, after 5 μs the mixing of the layers has completed and the transient structure is no longer present (c). Image adapted from [17].

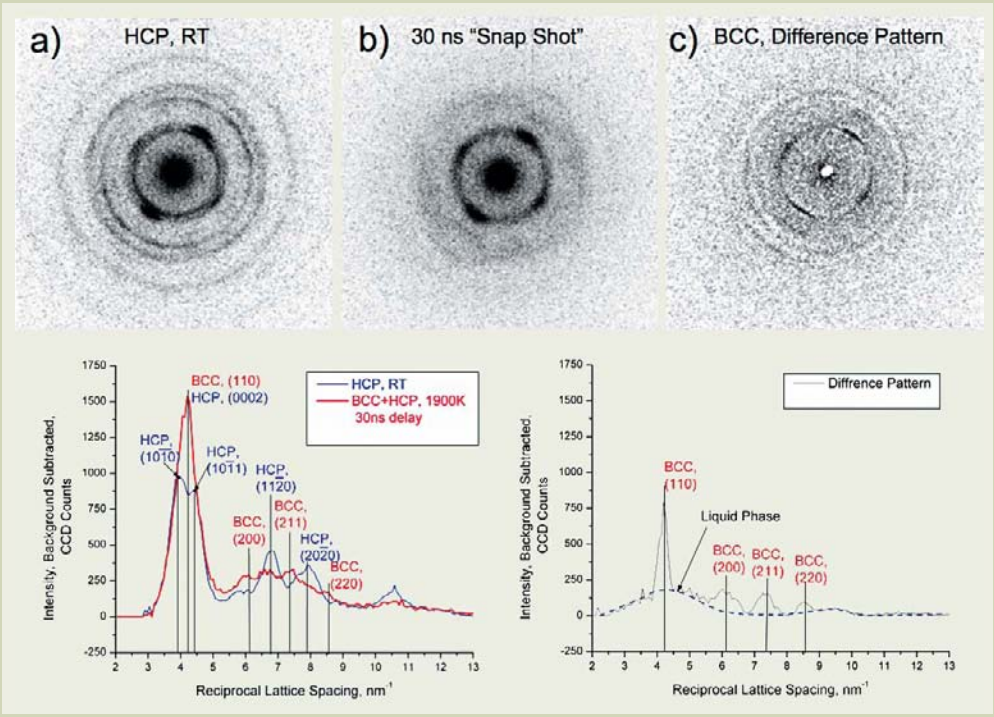


Fig. 4 Diffraction patterns depicting a martensitic type α-β phase transformation of Ti acquired using different pump/probe pulse delays. The initial state is shown in (a) while (b) was acquired 30 ns after initiating the reaction with a sample drive laser pulse. The difference between the initial and during transformation states is shown in (c). Rotationally averaged diffracted intensity versus the reciprocal lattice spacing as depicted in the lower panel were used to determine the phase content as a function of time. Image adapted from [15].

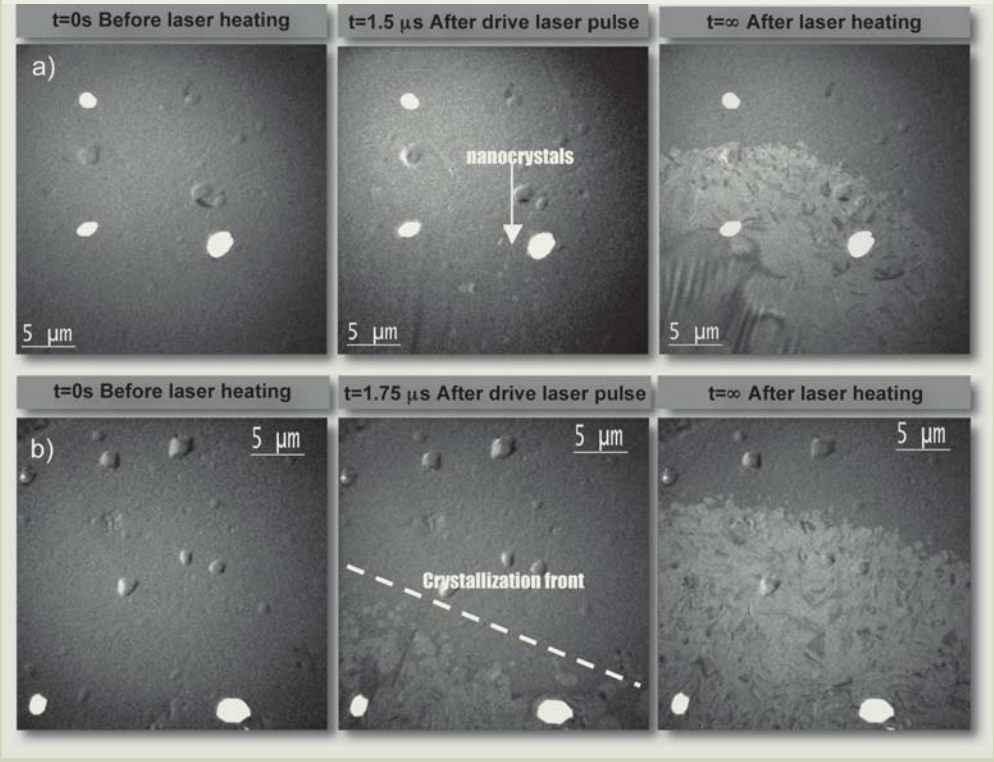


Fig. 5 Series of 15 ns exposure pulsed electron images, a) left image taken before laser heating, middle image taken 1.5 μs after laser strikes the foil, right image taken after foil cools to room temperature, b) similar series of images from different region on the foil and with the middle image taken 1.75 μs after the pump laser irradiates the specimen. Images adapted from [16].

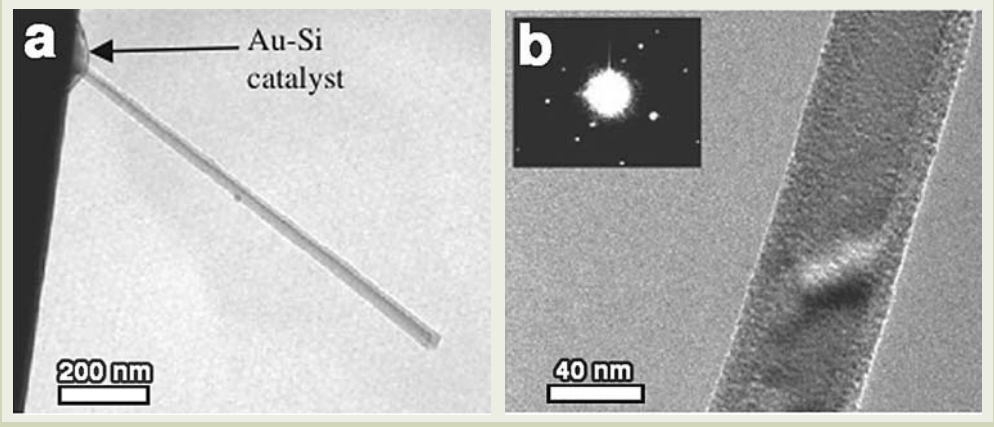


Fig. 6 Growth of a Si nanowire following laser ablation inside the DTEM. (a) depicts the formation of a catalyst bulb and nanowire after laser based melting of the Si substrate and 4 nm deposited layer of Au. A higher magnification image of a Si nanowire with diffraction pattern inset (b) shows growth occurred along the <111> direction. Image adapted from [18].

event within an *in situ* fluid holder environment.

Several possible examples of biomolecular reactions that could be initiated by an infrared laser induced temperature jump include observing nanoparticle nucleation and growth within the protein cage of ferritin [25], imaging DNA binding by Rad51 [26] or the assembly/disassembly of microtubules along with their interactions with motor proteins [27]. Additionally, the sample drive laser does not need to be used to initiate a temperature-jump, rather it could be used at a wavelength of 532 nm to activate the photoswitch conjugated opening/closing of ion channels [28]. Thus, if the DTEM can either outrun beam induced damage to proteins or low dose methods can be used to spread the total accumulated dose over 10 – 20 images, then the dynamics of many biological processes occurring on nanoscale and involving macromolecular complexes or cells might soon be observed.

## Conclusion

The DTEM has been used to image several types of reactions at the nanoscale both spatially and temporally. While the resolution is currently limited by the brightness of the photocathode source, future modifications promise to increase the spatial resolution to near one-angstrom and a temporal resolution of between 10 ns and 1 μs. The high spatial and temporal resolution coupled with the use of *in-situ* gas and fluid stages and the ability to image in either stroboscopic or single-shot mode with multi-frame movie mode capabilities will increase the regime of dynamic processes capable of observation in the DTEM to include phase transformations of a structural and electronic nature, nucleation, growth and oxidation of nanoparticles within controlled environments and the assembly/disassembly of protein complexes and other biomolecular interactions.

## Acknowledgments

This work was performed under the auspices of the U.S. Department of Energy, by Lawrence Livermore National Laboratory under contract DE-AC52-07NA27344.

## References

[1] Krivanek, O.L., Corbin, G.J., Dellby, B., Elston, B.F., Keyse, R.J., Murfitt, M.F., Own, C.S., Szilagyi, Z.S. and Woodruff, J.W. "An Electron Microscopy for the Aberration-Corrected Era" *Ultramicroscopy*, **108**, 179-195 (2008).

[2] King, W. E., Campbell, G. H., Frank, A., Reed, B., Schmerge, J. F., Siwick, B. J., Stuart, B. C. and Weber, P. M. "Ultrafast Electron Microscopy in Materials Science, Biology, and Chemistry" *J Appl Phys*, **97**, 11110 (2005).

[3] Siwick, B. J., Dwyer, J. R., Jordan, R. E. and Miller, R. J. D. "An Atomic-Level View of Melting using Femtosecond Electron Diffraction" *Science*, **302**, 1382-1385 (2003).

[4] Siwick, B.J., Dwyer, J.R., Jordan, R.E. and Miller, R.J.D. "Femtosecond electron diffraction studies of strongly driven structural phase transitions" *Chem Phys*, **299**, 285-305 (2004).

[5] Lobastov, V. A., Srinivasan, R. and Zewail, A. H. "Four-dimensional Ultrafast Electron Microscopy" *Proc Natl Acad Sci USA* **102**, 7069-7073 (2005).

[6] Baum, P. and Zewail, A. H. "Breaking Resolution Limits in Ultrafast Electron Diffraction and Microscopy" *Proc. Natl. Acad. Sci. U.S.A.* **103**, 16105 (2006).

[7] Baum, P., Yang, D-S. and Zewail, A. H. "4D Visualization of Transitional Structures in Phase Transitions by Electron Diffraction" *Science*, **318**, 788 (2007).

[8] Yang, D-S., Lao, C. and Zewail, A. H. "4D Electron Diffraction Reveals Correlated Unidirectional Behavior in Zinc Oxide Nanowires" *Science*, **321**, 1660 (2008).

[9] Baum, P. and Zewail, A.H. "Femtosecond Diffraction with Chirped Electron Pulses" *Chem. Phys. Lett.* **462**, 14–17 (2008)

[10] Gahlmann, A., Park, S. T. and Zewail, A. H. "Ultrashort Electron Pulses for Diffraction, Crystallography, and Microscopy: Theoretical and Experimental Resolutions" *Phys Chem Chem Phys*, **10**, 2894-2909 (2008).

[11] Bostanjoglo, O. and Horinek, W.R. "Pulsed TEM: A new method to detect transient structures in fast phase transitions" *Optik*, **65**, 361-367 (1983).

[12] Armstrong, M.R., Boyden, K., Browning, N.D., Campbell, G.H., Colvin, J.D., DeHope, W.J., Frank, A.M., Gibson, D.J., Hartemann, F., Kim, J.S., King, W.E., LaGrange, T.B., Pyke, B.J., Reed, B.W., Shuttlesworth, R.M., Stuart, B.C. and Torralva, B.R. "Practical considerations for high spatial and temporal resolution dynamic transmission electron microscopy." *Ultramicroscopy*, **107**, 356–367 (2007).

[13] LaGrange, T., Armstrong, M. R., Boyden, K., Brown, C. G., Campbell, G. H., Colvin, J. D., DeHope, W. J., Frank, A. M., Gibson, D. J., Hartemann, F. V., Kim, J. S., King, W. E., Pyke, B. J., Reed, B. W., Shirk, M. D., Shuttlesworth, R. M., Stuart, B. C., Torralva, B. R. and Browning, N. D. "Single-Shot Dynamic Transmission Electron Microscopy" *Appl Phys Lett*, **89**, 044105 (2006).

[14] LaGrange, T., Campbell, G. H., Turchi, P. E. A. and King, W. E. "Rapid Phase Transformation Kinetics on a Nanoscale: Studies of the α-β Transformation in Pure, Nanocrystalline Ti using the Nanosecond Dynamic Transmission Electron Microscope" *Acta Materialia*, **55**, 5211-5224 (2007).

[15] LaGrange, T., Campbell, G.H., Reed, B.W., Taheri, M.L., Pesavento, J.B., Kim, J.S. and Browning, N.D., "Nanosecond time-resolved investigations using the *in situ* of dynamic transmission electron microscope (DTEM)" *Ultramicroscopy*, 108, 1441-1449 (2008).

[16] LaGrange, T.B., Grummon, D.S., Reed, B.W., Browning, N.D., King, W.E. and Campbell, G.H. "Strongly Driven Crystallization Processes in a Metallic Glass" Applied Physics Letters In Press (2009).

[17] Kim, J.S., Lagrange, T., Reed, B.W., Taheri, M.L., Armstrong, M.R., King, W.E., Browning, N.D. and Campbell, G.H., "Imaging of transient structures using nanosecond in situ TEM" *Science*, **321**, 1472-1475 (2008).

[18] Taheri, M.L., Reed, B.W., LaGrange, T.B. and Browning, N.D., "In situ laser synthesis of Si nanowires in the dynamic TEM" *Small*, **4**, 2187-2190 (2008).

[19] Taheri, M.L., LaGrange, T., Reed, B.W., Armstrong, M.R., Campbell, G.H., Dehope, W.J., Kim, J.S., King, W.E., Masiel, D.J. and Browning, N.D. "Laser-Based In Situ Techniques: Novel Methods for Generating Extreme Conditions in TEM Samples" Microsc. Res. & Tech, **72**, 122–130 (2009).

[20] Reed, B.W., Armstrong, M.R., Browning, N.D., Campbell, G.H., Evans, J.E., LaGrange, T. and Masiel, D.J. "The Evolution of Ultrafast Electron Microscope Instrumentation" Microscopy and Microanalysis Accepted (2009).

[21] Kruit, P. & Jansen, G. H. "Space Charge and Statistical Coulomb Effects" In *Handbook of Charged Particle Optics*, Orloff, J. (Ed.), pp. 275-318. Boca Raton: CRC Press (1997).

[22] Yao, S., Han, Y., Liu, W., Zhang, W. and Wang, H. "Synthesis of CdS nanocrystals with different morphologies via an ultraviolet irradiation route" *Materials Chemistry and Physics*, **101**, 247–250 (2007).

[23] Houskova, V., Stengl, V., Bakardjieva, S., Murafa, N., Kalendova, A. and Oplustil, F. "Zinc Oxide Prepared by Homogeneous Hydrolysis with Thioacetamide, Its Destruction of Warfare Agents, and Photocatalytic Activity" *J. Phys. Chem. A*, **111**, 4215–4221 (2007).

[24] Glaeser, R.M. "Retrospective: radiation damage and its associated 'information limitations'" *J Struct Biol*. **163**, 271-6 (2008).

[25] Quintana, C., Cowley, J.M., and Marhic, C. "Electron nanodiffraction and high-resolution electron microscopy studies of the structure and composition of physiological and pathological ferritin." *J Struct Biol.* **147**, 166-78 (2004).

[26] Hilario, J., Amitani, I., Baskin, R.J. and Kowalczykowski, S.C. "Direct imaging of human Rad51 nucleoprotein dynamics on individual DNA molecules " *Proc Natl Acad Sci USA.* **106**, 361–368 (2009).

[27] Kerssemakers, J.W.J., Munteanu, E.L., Laan, L., Noetzel, T.L., Janson, M.E. and Dogterom, M. "Assembly dynamics of microtubules at molecular resolution" *Nature*, **442**, 709-712 (2006).

[28] Gorostiza, P., Volgraf, M., Numano, R., Szobota, S., Trauner, D. and Isacoff, E.Y. "Mechanisms of photoswitch conjugation and light activation of an ionotropic glutamate receptor" *Proc Natl Acad Sci USA.* **104**, 10865-10870 (2007).

# An Appraisal of High Resolution Scanning Electron Microscopy Applied To Porous Materials

**Sam M. Stevens[†,††], Kjell Jansson[†], Changhong Xiao[†], Shunsuke Asahina[†††], Miia Klingstedt[†], Daniel Grüner[†], Yasuhiro Sakamoto[†], Keiichi Miyasaka[†,††††], Pablo Cubillas[††], Rhea Brent[††], Lu Han[†,†††††], Shunai Che[†††††], Ryong Ryoo[††††], Dongyuan Zhao[†††††], Mike Anderson[††], Ferdi Schüth[†††††], and Osamu Terasaki[†,††††]***

[†] **Department of Physical, Inorganic & Structural Chemistry, Arrhenius Laboratory, Stockholm University**
[††] **The University of Manchester**
[†††] **JEOL Europe**
[††††] **Korea Advanced Institute of Science and Technology**
[†††††] **Shanghai Jiao Tong University**
[†††††] **Fudan University**
[†††††] **Max Planck Institute Mülheim**

Nanoporous materials such as zeolites and mesoporous silica crystals have attracted a lot of attention in recent years. In particular, the incorporation of various materials such as organic molecules, or metal nanoparticles and other inorganic compounds within their pores which give rise to fascinating new functions. For such materials, it is essential to determine their structure, composition and mechanisms of growth in order to maximize their utility in future applications.

Recent progress in the performance of SEM is enormous, especially in low energy imaging where we can now directly observe fine surface structures of porous materials even those that are electrical insulators. Furthermore, by precise filtration and detection of emitted electrons by their energy, we can selectively obtain different types of information such as material composition, location of particles inside or outside the pores etc. The physical processes and technologies behind this precise tuning of landing and detection energies for both impact and emitted electrons, respectively, are explained and illustrated using a number of porous materials including zeolite LTA, SBA-15, SBA-16, zeolite LTL, FDU-16 and Au@$TiO_2$ ' rattle spheres,' along with comparisons with other techniques such as atomic force microscopy (AFM) and transmission electron microscopy (TEM). We conclude that, by using extremely low landing energies, advanced sample preparation techniques and through a thorough understanding of the physical processes involved, HRSEM is providing new and unique information and perspectives on these industrially important materials.

## Introduction

In this report, we classify porous materials based on structural characteristics into the following three categories: (i) Materials with a periodic pore arrangement with uniform size either in periodic framework structures such as microporous zeolites or in amorphous silica wall forming "cavity crystals" such as meso- and macro-porous silica crystals; (ii) Materials which have irregular size of pores in a random arrangement such as mesoporous silica with worm-like pores or random pores in size and arrangement; and (iii) Hollow nano spheres with or without nano-particles inside. Both nanoporous (micro-, meso- and macro-porous) materials and their composites with nano-particles have been prepared. All of these materials are extremely important in a number of different industries. In (i), pores often provide acidic sites and large surface areas for heterogenous catalysis to occur as is the case for (ii) where pores may also be modified with transition metals or used to reversibly bind molecules for medicinal applications. Owing to their porosity and structure it is even possible to use them for both tissue engineering and drug delivery. In the case of (iii), hollow spheres with nanoparticles have also been synthesized with the purpose of maintaining characteristic features of the nanoparticles whilst preventing their aggregation at catalytically active conditions. They also exhibit new properties with their encapsulating hollow spheres. In order to maximize both the efficiency and range of applications of these porous crystals, an understanding of their structure and growth mechanism is therefore extremely important for further control of growth processes to tailor these materials for our specific needs. Such properties we wish to control include, but are not limited to, pore size, level of exposure of pores to the crystal surface, orientation of pores with respect to crystal surface, crystal size and shape, hydrophobicity/hydrophilicity and properties of the guest material.

With regards to porous crystals, scanning electron microscopy (SEM) has long been used as a method to rapidly gather information such as the size and shape of crystals. This is because the microscopes have a large depth of focus and are relatively easy to operate with a minimum of tuition. As visualisation of crystals occurs at scan speeds and at a range of magnifications it is therefore possible to gather a statistically significant amount of data. This information is important when discussing crystal growth trends [1], but does not supply information to scientists about the crystal formation and structural chemistry at the nanometer scale*. Such information may be found from observation of fine surface structure, for example: in zeolite LTA the height and shape of surface terraces, observed by atomic force microscopy (AFM), provides evidence of the existence of discrete growth units from which the crystals form and the nature of the growth mechanism as a function of reaction conditions [2]. In scientific reports of this nature, SEM images usually appear as little more than supporting information or visual expatiation [3] to the scientific observations and discussions on crystal growth as gleaned from other analytical techniques such as atomic force microscopy (AFM) and also by powder X-ray diffraction (XRD), transmission electron microscopy (TEM) and others.

In the last decade there has been a quantum leap forward in the utility of SEM, which we now dub high-resolution SEM (HRSEM). Particular advances include: Improvement of objective lens with smaller chromatic and spherical aberration coefficients; precise control of the landing energy of impact electrons and therefore a dramatic reduction in charging (the main contributor to loss of information in observation of insulating materials) whilst retaining a suitably small probe size; and an ability to obtain selective information by tuning proper electron energy ranges and collecting angles for detection. Important crystal features, such as mesoporous channel openings, terminations and curvature [4] and other surface features such as twinning and growth fronts in zeolites [5] have been reported.

We begin by comparing the level of detail and various other merits between HRSEM and AFM, then further quantify the measurable level of surface topography and show that the HRSEM is able to identify nanometer scale crystal surface features through an elegant example, whilst at the same time providing information on larger crystal details - both with a high level of fidelity. We then show that through new sample preparation techniques, the detail HRSEM can reach is

*That said, SEM is also able to determine the chemical composition of points on a crystal by measuring the energy / wavelength of the characteristic X-ray in energy / wavelength dispersive spectroscopy (EDS / WDS), respectively but the elemental information is an average over the range of a micrometer.

[†]SE-10691 Stockholm, Sweden, terasaki@struc.su.se

[††††]Daejeon 305-701, Korea, terasaki@kaist.ac.kr

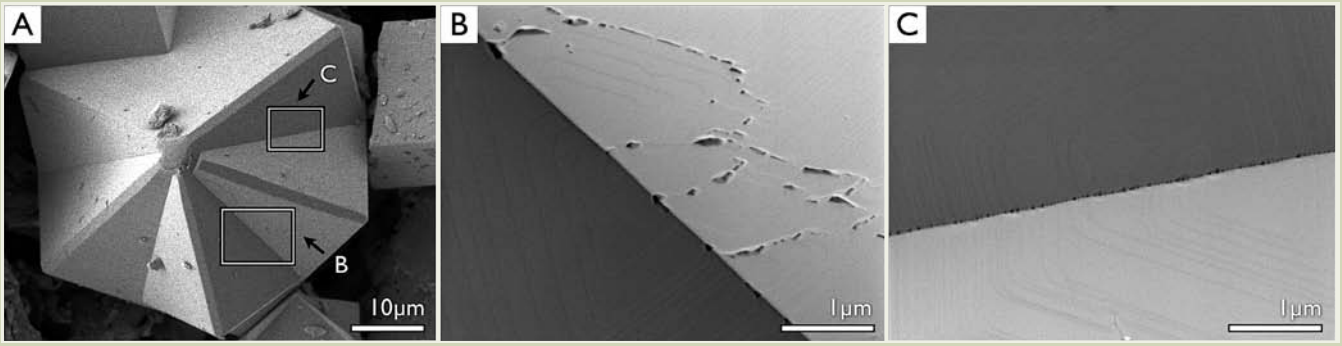


Fig.1 HRSEM images of twinned crystals of zeolite LTA. (B) and (C) show the interface between the two twins located in the boxes on (A). 1 keV landing energy, 2.5 keV column energy. In-lens detector, Sb mode (See Figure 8-1, D).

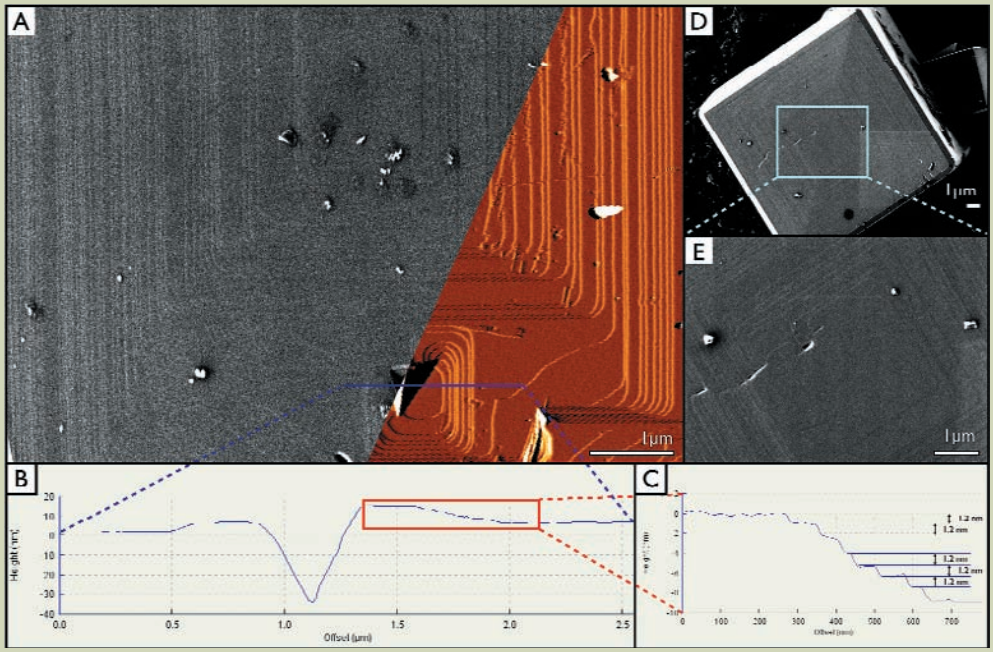


Fig.2 (A) composite HRSEM (left, grayscale) and AFM (right, red-scale) image of the exact same (100) surface of the exact same crystal of zeolite LTA. (B) Cross section is of AFM height measurements corresponding to the purple line with a zoom in (C). (D) whole (100) surface of zeolite LTA with a magnification of the position of prevailing screw dislocation in (E). HRSEM: 1 keV landing energy, 2.5 keV column energy, In-lens detector, Sb mode. AFM: Constant Force Mode.

not limited to the surface of the crystal but includes internal pore structure by cross section analyses - the three dimension structural information of which differs from the projected images observed in TEM. As most porous crystals are insulators, they are therefore subject to charging which reduces image information. Using extremely low landing energies* by a deceleration of highly unstigmated electrons leaving the objective lens called *gentle beam* (also known as *stage bias* or *retarding field*), we are able to remove charging whilst maintaining a finely focused electron probe as electrons pass through the objective lens with the column energy. We then explore the other types of detectable contrast produced from electron irradiated samples by careful filtering and detection of emitted electrons based on their energy using an energy filter for secondary electrons called r-Filter and we show that compositional contrast is extremely useful in understanding the nature of these new and exciting materials.

## Experimental, Results and Discussion, etc.:

### Instrument & Electron Interaction Overview

An SEM is composed of a number of chambers. The first is a column filled with an electron source, apertures, scanning coils and lenses, down which an electron beam is first generated, accelerated, demagnified to a small electron *probe*, and then deflected in a raster fashion over the area to be imaged in the main chamber. The interaction between the impact electrons and the sample generates a number of different electrons such as *back scattered electrons* (BE), *secondary electrons* (SE) and Auger electrons and other emissions such as characteristic and Bremsstrahlung X-rays, visible light through elastic and inelastic scattering processes. Inelastically generated and emitted SEs are classified into two types called SE1 and SE2 which are produced within materials either directly from an incident (primary) electrons or from internally scattered electrons, respectively. Therefore SE1 produces a contrast highly dependant upon sample surface geometry and gives topographic information selectively, while SE2 comes from larger depth and volume than those of SE1, the contribution of SE2 to the image reduces topographic information. It is noteworthy that reduction of SE2 contribution to an image can be made only by reducing the landing energy. Characteristic X-rays, which are used for EDS and WDS measurements, give chemical information. Rutherford scattering of electrons involves high scattering angles of impact electrons, a detectable proportion of which are scattered through a large enough angle such that their resultant trajectory allows them to exit through the sample surface as BE. As Rutherford scattering is highly dependant upon the electrostatic potential of the sample atom nucleus, and therefore the atomic number, BE therefore provides compositional contrast . The electrons generated are collected by a scintillator or solid state detector and the signal is multiplied and delivered as a grayscale value, depending upon the intensity, to a viewing screen that is progressively scanning in synchronisation with the scanning beam. The result is an image of the crystal that may be saved to film or digital image file. All HRSEM images in this article were taken using a JEOL high-resolution scanning electron microscope fitted with in-lens detector, gentle beam, cold field emission electron source and EDS detector (JSM-7000F and JSM-7401F) installed at Stockholm University, Sweden.

More information about the type of interactions produced can be found both in reference [6] and throughout this article. We begin by examining topographic contrast.

*Landing voltage
=accelerating (column) voltage - stage-bias voltage

### Level of Information/Resolution & Comparison With Atomic Force Microscopy

An elegant example of the power of imaging in HRSEM compared to AFM is shown in **Figure 1**. Part A shows a twinned crystal of zeolite LTA where each twin is of similar size and shape and considerably overlapped. Visualisation of this twin would not be possible in AFM owing to the steep sides of the crystal. In parts B and C, we increase the mag-

nification to two areas where the twins intersect each other. The AFM would not be able to probe into the sharp angle between these two surfaces owing to hindrance from the tip shape nor would it be able to image the macroporosity along the twin intersection. Surface steps are clearly visible in Figure 1B and C implying a high level of vertical resolution - the size of such features is quantified below.

As discussed in the introduction, SEM has, until recently, been unable to image surface terraces of nanoporous crystals which are essential to further the understanding of their growth with this information only reliably attained by AFM. The topographic sensitivity is so high that surface terraces on zeolite LTA of 1.2 nm are clearly observable in HRSEM images. We have confirmed this by imaging the surface of zeolite LTA *ibidem* (in the same place) using both AFM and HRSEM and overlaying the two images as shown in **Figure 2**A. It can be seen that the two images overlap with extremely good correlation and all the terraces visible in AFM are observable in the HRSEM image. Height cross-sections from the AFM (Figure 2.B and C) show that the step heights are all 1.2 nm and therefore the nominal vertical sensitivity is higher than the guaranteed lateral resolution of the microscope at this beam condition (1.5 nm).

HRSEM images can be collected much more rapidly and from a larger area by HRSEM than AFM, thus making the technique particularly efficient. Images may also be obtained at lower magnifications than that of the AFM and still the terrace information is conserved (Figure 2D and E). In AFM, the area to be scanned is limited by the range of the piezoelectric crystal used to move either the cantilever or the stage (depending on the type of AFM) which delineates, and therefore distorts the image at high displacement. The distortion in HRSEM is so slight that it can be neglected: in **Figure 3**, the left hand image is composed of four individual images of zeolite LTL with detailed surface terraces which match up well enough so that they join together seamlessly. The surface information is still conserved as in the three digital zooms shown in Figure 3 A2 to 3A4, across the length of the crystal.

AFM uses a physical probe, rather than a beam of electrons, that scans in raster fashion across the surface of the area to be observed. The tip is therefore prone to probe-tip dilation as can be seen in Figure 3B where the surface crater of zeolite LTL is imaged in both AFM (Figure 3B1) and SEM (Figure 3B2 to 3B3) and the appearance of terrace forking, the gap between each prong, is undetectable to the bulky AFM probe. The latter shows much more information about the crater detail. AFM does not perform well when the sample surface is far from orthogonal to the probe, such cases include when crystals have rounded surfaces as in silicalite-2 [7] or upon examining surfaces that intersect at obtuse angles.

As HRSEM is unable to measure vertical heights directly, AFM was used to confirm vertical resolution illustrating one advantage of AFM over SEM [8]. In terms of lateral resolution, however, HRSEM is the optimum technique. We now illustrate how this level of resolution and contrast is not just limited to surface features but also applicable to the internal structure of materials by first using a new sample preparation technique called cross-section polishing.

## Cross-Section Polishing & Comparison With Transmission Electron Microscopy

Cross-section polishing uses a beam of accelerated argon ions to *polish* the material of interest. By placing a shield that is resistant to the argon ion beam on top of the material, this shield protects a portion of the material from the abrasive argon ion beam, and polishing occurs as shown in **Figure 4**. There is a high dependancy of attrition rate upon the angle between material and direction of the argon ion beam. As the rate of attrition is effectively zero when the surface of the material is parallel to the argon ion beam, a very flat cross section is therefore formed. It is free from contamination and damage associated with other types of polishing such as mechanical or chemical etching [9]. In the case of porous crystals, they are first embedded in a (preferably conductive) medium such as silver loaded epoxy or carbon glue before being polished. In

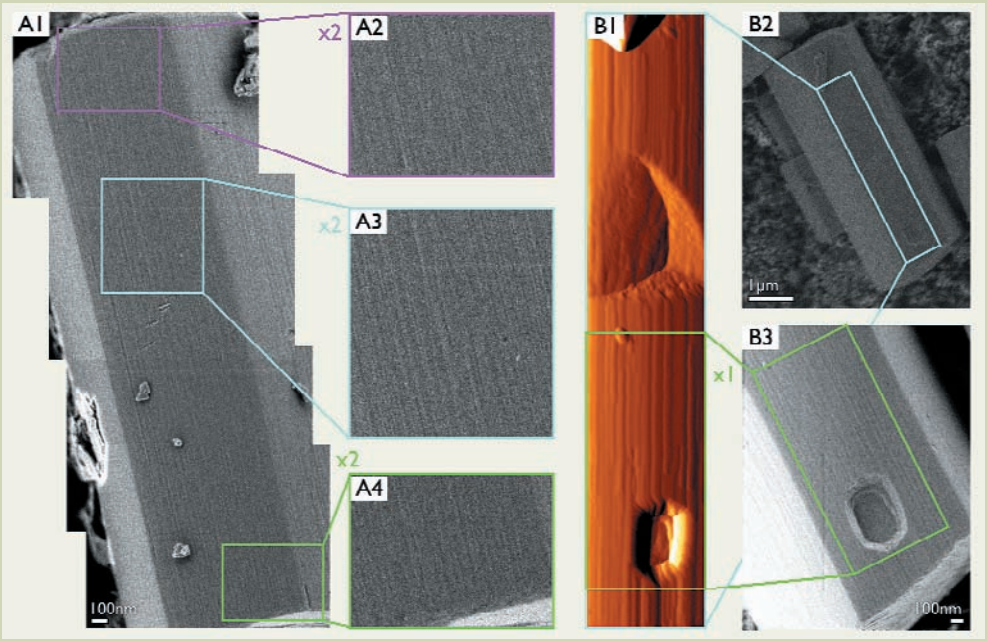


Fig.3 Zeolite LTL images. (A1) is a composite of four SEM images, the areas highlighted at the top (magenta - A2), middle (cyan - A3) and bottom (green - A4) of the crystal are 2x digital zoom of those images. Right hand crystal is shown in both AFM (B1), SEM (B2) and HRSEM (B3) images, notice the probe-tip dilation effect in the AFM reducing the amount of information around the small crater towards the bottom of the crystal. HRSEM: 0.8 keV landing energy, 2.3 keV column energy. In-lens detector, Sb mode. AFM: Constant Force Mode.

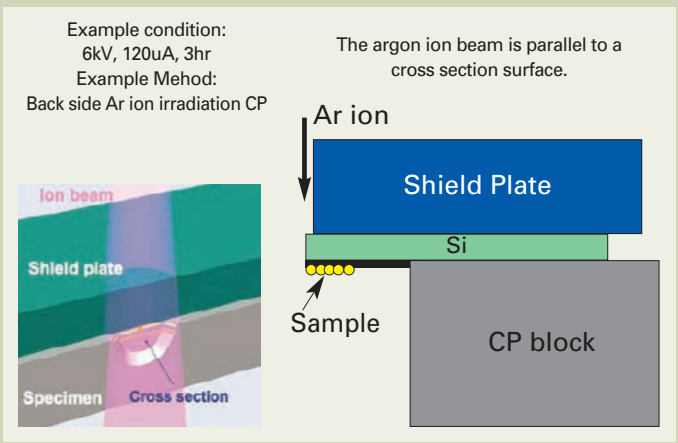


Fig.4 Schematic of the Cross Section Polisher as viewed from the side (top-right) and isometrically (bottom-left).

order to reduce imperfections in the etching process, the resin is heated or left under vacuum when drying in order to remove air bubbles, as these small cavities create eddies and fluctuations in the otherwise homogenous *stream* of the argon ion beam. It is noteworthy that much of the atrophied material produced in the polishing process presents enough of a volume to contribute to contamination contrast. To reduce this problem, the supports are cleaned with ethanol before sample preparation and heated to 250°C prior to introduction into the exchange chamber of the HRSEM.

In **Figure 5**, HRSEM images of SBA-15 are shown where the mesoporous channels terminate in corrugations on the side wall surface or as U-turns (Figure 5A) or open (Figure 5B) hexagonally distributed pores on the front wall. By encapsulating these crystals in a solid medium,it is possible to polish these materials as shown in Figure 5C to 5D. Once the internal structure is exposed it can be seen in the HRSEM that the polishing process is gentle enough to preserve both the mesoporosity and the interface between the different grains of SBA-15, the latter is invisible to TEM where the size of the crystal would be too thick for transmission and the lack of periodicity of the interface. Similarly, the change in orientation of the pore across an individual crystal can be followed. This point is reiterated in the spherical counterparts shown in both TEM (Figure 5F) and by cross section polishing (Figure 5E) where the contrast changes from lines (channels run perpendicular to the optic axis) to spots (channels run parallel). Cross-section polishing also allows a profile view of surface terminations that are visible in TEM but difficult to distingusih and disprove to be fracture lines of a crystal fragment caused by the compulsory crushing required to accommodate crystals of this size upon a TEM grid.

## Gentle Beam Helps With Charging In Insulating Porous Materials

An unfortunate occurrence when imaging insulating specimens in HRSEM is that they often experience a phenomenon known as charging. This results in the masking of image information by areas of extremely high or low contrast or by a distortion in the image. This is due to a build-up of unstable and in-homogenous electric fields generated by either a net deficit or surplus of electrons provided by the impact electrons of the electron source which then leave the sample either by conduction to earth or by emission. These electric fields disrupt the trajectory and generation of emitted electrons. As most porous materials are composed of silica, they are virtually non-conductive and so balancing of electrons within the specimen requires tight control of the ratio of emitted to impact electrons, known as the electron yield, $\sigma$, preferably keeping it as close as possible to unity for a given beam condition. The electron yield varies greatly with both surface angle (thus giving rise to topographic contrast, as discussed above) and accelerating energy, or more precisely, the landing energy which is the energy electrons impact the surface of the sample. The critical energy and the general dependency of electron yield differs from material to material but follows a general curve with a negative gradient*. The landing energy may be controlled to find the *critical energy* which is the point below/above which the electron yield is respectively greater/less than unity [10]. In siliceous materials, this is usually between 500 eV and 1.5 keV. To highlight this we have imaged both SBA-16 and FDU-16; one silica based and the other carbon based, both of which possess the same structural symmetry and approximately the same pore density and shape. In **Figure 6**, where the contrast of each image is normalised against the highly ordered pyrolytic graphite (HOPG) substrate. As HOPG is very conductive and therefore has effectively a constant electron yield of 1 over all landing energy used. It can be seen in the case of SBA-16 that the critical energy is between 1.4 and 1.7 keV, whereas in FDU-16, the range is much larger and at relatively higher energies. Unfortunately for SBA-16, at the

*The function is actually hump shaped with a second, lower critical energy at a lower landing energy. As this side of the maxima (with a positive gradient) falls below the practical range of current microscopes, it is removed from the scope of this paper for pragmatic reasons.

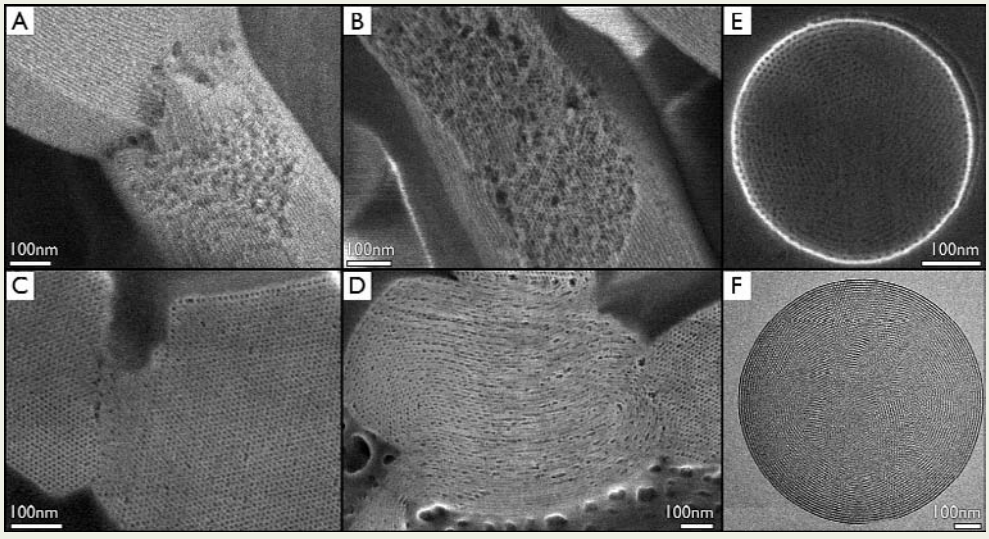


Fig.5 Mesoporous silica SBA-15. (A) and (B) are HRSEM images of the unaltered crystals clearly displaying surface channels and terminations. (C) and (D) are HRSEM of the powder after cross section polishing, notice surface profile is visible along with grain boundaries and change of channel orientation. (e) and (f) are of crystals with spherical morphology viewed both as a cross section (HRSEM) and projection (HRTEM), respectively.

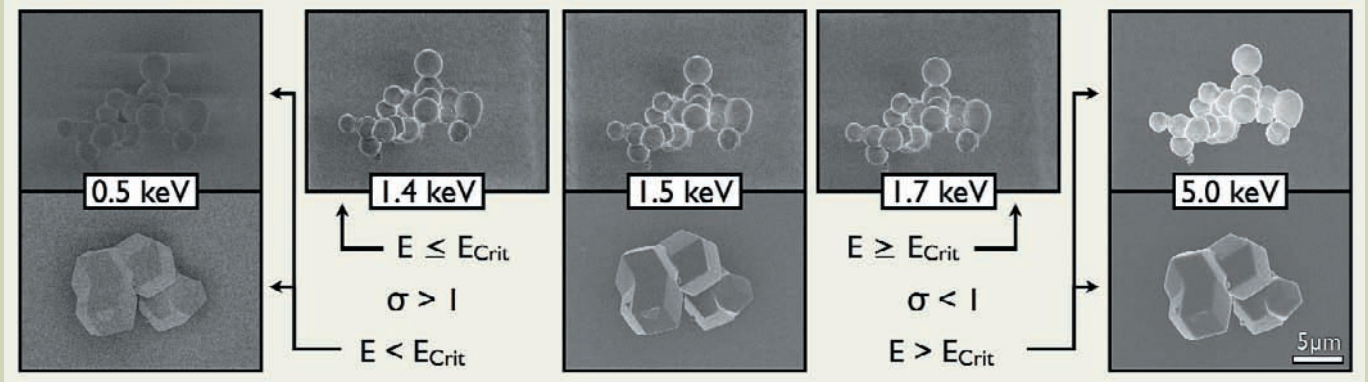


Fig.6 Mesoporous silica SBA-16 (top row) and reciprocal carbon analogue FDU-16 (bottom row) imaged at different accelerating voltages. Contrast normalized to that of the HOPG substrate. No surface bias. In-lens detector, Sb mode.

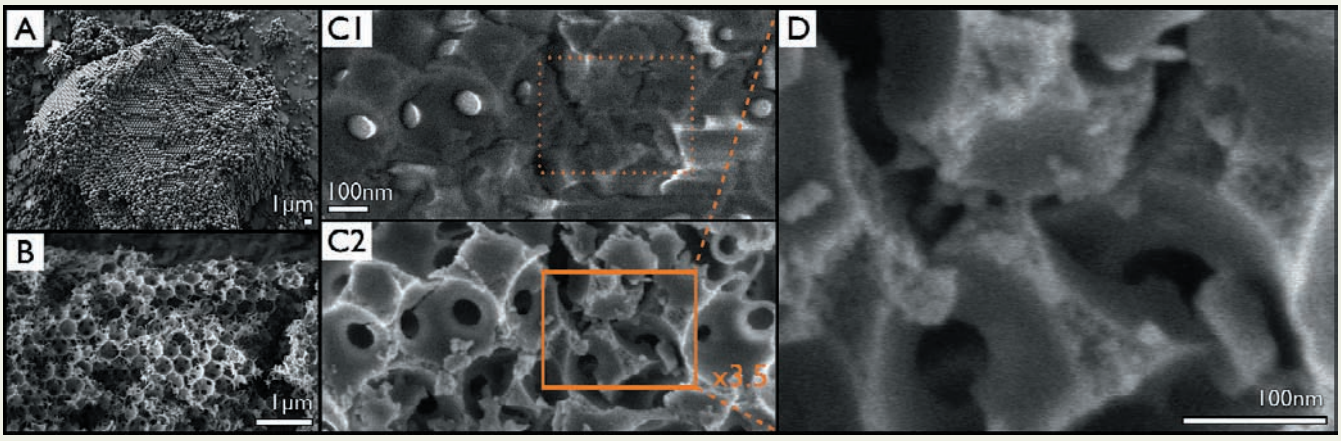


Fig.7 Hierarchical Porous Material. (A) polysterene spheres used to form macroporous template, (B) free powder, (C1) and (C2) taken without and with a 500 eV stage bias of the free powder lightly crushed exposing mesoporous network highlighted in(D). 3 keV column energy. In-lens detector, Sb mode.

range of desirable accelerating energies where charging is minimised, the diffraction error and chromatic aberration dramatically limit the minimum possible probe diameter and resolution drops below that required to image the important surface features [11].

To overcome the reduction in resolving power of the SEM at accelerating energies below 5 keV, the use of beam retardation, otherwise known as *gentle beam* mode, has been adopted. This is where the accelerating energy, which determines the minimum probe size and therefore the limit of the resolution when passing through the column (column energy), is retarded by a negatively charged stage bias to a lower, landing energy equal to the column energy minus the stage bias. The landing energy used is significantly lower than that used before in obtaining images of such high levels of resolution. Using this method it is possible to retain the advantage of high resolution imaging by having a high column energy but also reducing charging effects by operating at a lower landing energy.

A further benefit of gentle beam is that the electric field employed is orders of magnitude stronger, more homogenous and more stable than that of the small electric fields discussed above arising from sample surfaces with steep gradients or thin areas (i.e. tips and edges). This means that the stage bias supersedes the small fields and removes streaking and localised areas of charging, thus cancelling the disruption to the trajectory and energy of the emitted electrons. This can be seen in **Figure 7** where a hierarchical porous material [12] templated from polystyrene spheres (Figure 7A) is crushed producing many tips and edges. When imaged without and with a relatively small stage bias of 500 eV (Figure 7C1 to 7C2, respectively) the difference to the improvement of the contrast is striking. There is also an increased resolution that can be seen as the mesopores within the walls of the macropore owing to the higher column energy and the mesoporosity in the macroporous wall are now observable (Figure 7D).

Charging is just one way in which emitted electrons may lower the amount of information detected in an HRSEM image. By careful tuning of both the landing energy and the stage bias, it is possible to produce electrons with the maximum information desired by the user. We shall show in the next section how it is also possible to selectively tune the energy of emitted electrons and the corresponding information to be gleaned from such electrons.

## r-Filter Used To Separate Different Types of Contrast

As discussed in the overview section, electrons with different energies, intensities and trajectories are generated during SEM dependant upon different factors. Fortunately, the energy difference between secondary and backscattered electrons is very large and SEMs fitted with an r-Filter are capable of independently detecting these different electrons. This is done by placing a detector not at the side of the SEM chamber but inside the objective lens. These *in-lens detectors* not only have a higher signal-to-noise ratio (as they are catching high-angle scattered electrons which are more prevalent when using gentle beam) but also facilitate the incorporation of electrodes placed in the objective lens which are then able to gate out/in electrons of different energies.

This can be seen in **Figure 8**, where Au@$TiO_2$ *rattlespheres* [13] are observed in *Sb mode* (predominantly secondary electrons, Figure 8.1A) where the information is topographic in nature, all electrons (Figure 8.1B) and *Bs mode* (predominantly back scattered electrons, Figure 8.1C) is almost all compositional contrast. By using both modes we are able to observe gold nanoparticles both encapsulated inside and outside the macroporous $TiO_2$ hollow spheres. The gold appears as bright spots of contrast in Bs mode. As can be seen in the images, both the short penetration of impact electrons with low landing energies and large attenuity of SE electrons allow for observation of gold particles on the surface of the spheres (Figure 8.2A to 8.2B) but is unable to distinguish other gold particles that are visible in the Bs mode appearing as very bright spots of contrast below the surface, encapsulated within the $TiO_2$ shell. The composition of both the shell and the nanoparticles with smaller than 20 nm in diameter are confirmed by now highly spatially resolved EDS measurements in spectra 2 and 1, respectively in Figure 8.3 - the same area is chemically mapped in Figure 8.4 for both titanium and gold.

## Conclusion:

We have shown that HRSEM is a technique capable of extracting nanoscopic information both from the surface and inside nano-, meso- and macro porous materials. Such information is not readily accessible using other techniques such TEM and AFM. The information is maximized using a combination of technologies including; cross-section polishing; gentle beam and r-Filter. By using ultra-low landing energies whilst maintaining a highly stigmated electron probe we were able to produce images of extremely high resolution without charging masking the information. A more detailed account may be found in our upcoming review article [14].

## Acknowledgments

The authors wish to acknowledge The Knut & Alice Wallenberg Foundation, Swedish Research Council, Japan Science and Technology Agency, EPSRC and ExxonMobil Research and Engineering for their financial support, JEOL SAS (Europe) and JEOL Ltd., for their technical support and Mohammad Jalil, Peter Alberius and L. Itzel Meza for supplying their samples. OT & YS acknowledge Prof. Kazuyuki Kuroda (Waseda University) for his continued encouragement and support.

## References

[1] Yang et al. Revision of Charnell's procedure towards the synthesis of large and uniform crystals of zeolites A and X. *Microporous and Mesoporous Materials* **vol. 90 (1-3)** 53-61. (2006)

[2] Agger et al. Crystallization in Zeolite A Studied by Atomic Force Microscopy. *J. Am. Chem. Soc.* **vol. 120 (41)** 10754-10759. (1998) ; Sugiyama et al. AFM observation of double 4-rings on zeolite LTA crystals surface. *Microporous and Mesoporous Materials* **vol. 28 (1)** 1-7 (1999); Meza et al. Differentiating fundamental structural units during the dissolution of zeolite A. *Chemical Communications (Cambridge, United Kingdom)* **(24)** 2473-2475. (2007)

[3] Smaihi. Investigation of the Crystallization Stages of LTA-Type Zeolite by

Complementary Characterization Techniques. *European Journal of Inorganic Chemistry* **vol. 2003 (24)** 4370-4377. (2003)
[4] Che et al. Direct observation of 3D mesoporous structure by scanning electron microscopy (SEM): SBA-15 silica and CMK-5 carbon. *Angewandte Chemie* (International ed. in English) **vol. 42 (19)** 2182-5 (2003); Terasaki et al. Structural study of meso-porous materials by elecrron microscopy, "Mesoporous Crystals and Related Nano-Structured Materials", *Studies in Surface Science and Catalysis* **Vol. 148**, 261-288, Elsevier (2004);. Wakihara et al. Investigation of the surface structure of zeolite A. *Physical Chemistry Chemical Physics* **vol. 7 (19)** 3416-3418 (2005); Tueysuez et al. Direct imaging of surface topology and pore system of ordered mesoporous silica (MCM-41, SBA-15, and KIT-6) and nanocast metal oxides by high resolution scanning electron microscopy. *Journal of the American Chemical Society* **vol. 130 (34)** 11510-11517
[5] Terasaki. Electron Microscopy Studies in Molecular Sieve Science. *Molecular Sieves - Science and Technology* **vol. 2** 71-112 (1999)
[6] Reimer. Scanning Electron Microscopy. Berlin: Springer-Verlag (1998)
[7] Stevens et al. High-Resolution scanning electron and atomic force microscopies: observation of nanometer features on zeolite Surfaces. *Studies in Surface Science and Catalysis* **vol. 174 (2)** 775-780 (2008)
[8] Anderson Michael et al. Modern microscopy methods for the structural study of porous materials. *Chemical Communications* **(8)** 907-16 (2004)
[9] Erdman et al. Precise SEM cross section polishing via argon beam milling. Microscopy Today (2006) vol. May pp. 22-25; Takahashi et al. A New Method of Surface Preparation for High Spatial Resolution EPMA/SEM with an Argon Ion Beam. *Microchimica Acta* **vol. 155 (1-2)** 295-300 (2006)
[10] Cazaux. e-Induced secondary electron emission yield of insulators and charging effects. Nuclear Instruments & Methods in Physics Research, Section B: *Beam Interactions with Materials and Atoms* **vol. 244 (2)** 307-322 (2006); Rau et al. Second crossover energy of insulating materials using stationary electron beam under normal incidence. Nuclear Instruments and Methods in Physics Research Section B: *Beam Interactions with Materials and Atoms* **vol. 266 (5)** 719-729 (2008)
[11] Reimer. Image Formation in Low-Voltage Scanning Electron Microscopy. SPIE: Optical Engineering Press (1993); Mullerova and Frank. Scanning Low-Energy Electron Microscopy. *Advances In Imaging And Electron Physics* **vol. 128** 309-443 (2003)
[12] Loiola et al. Synthesis and characterization of hierarchical porous materials incorporating a cubic mesoporous phase. *Journal of Materials Chemistry vol.* **18 (41)** 4985-4993
[13] Schüth et al. To be published; Pablo M. Arnal et al. High-Temperature-Stable Catalysts by Hollow Sphere Encapsulation. *Angew. Chem. Int. Ed.* **45,** 8224-8227 (2006)
[14] Jansson et al. To be submitted.

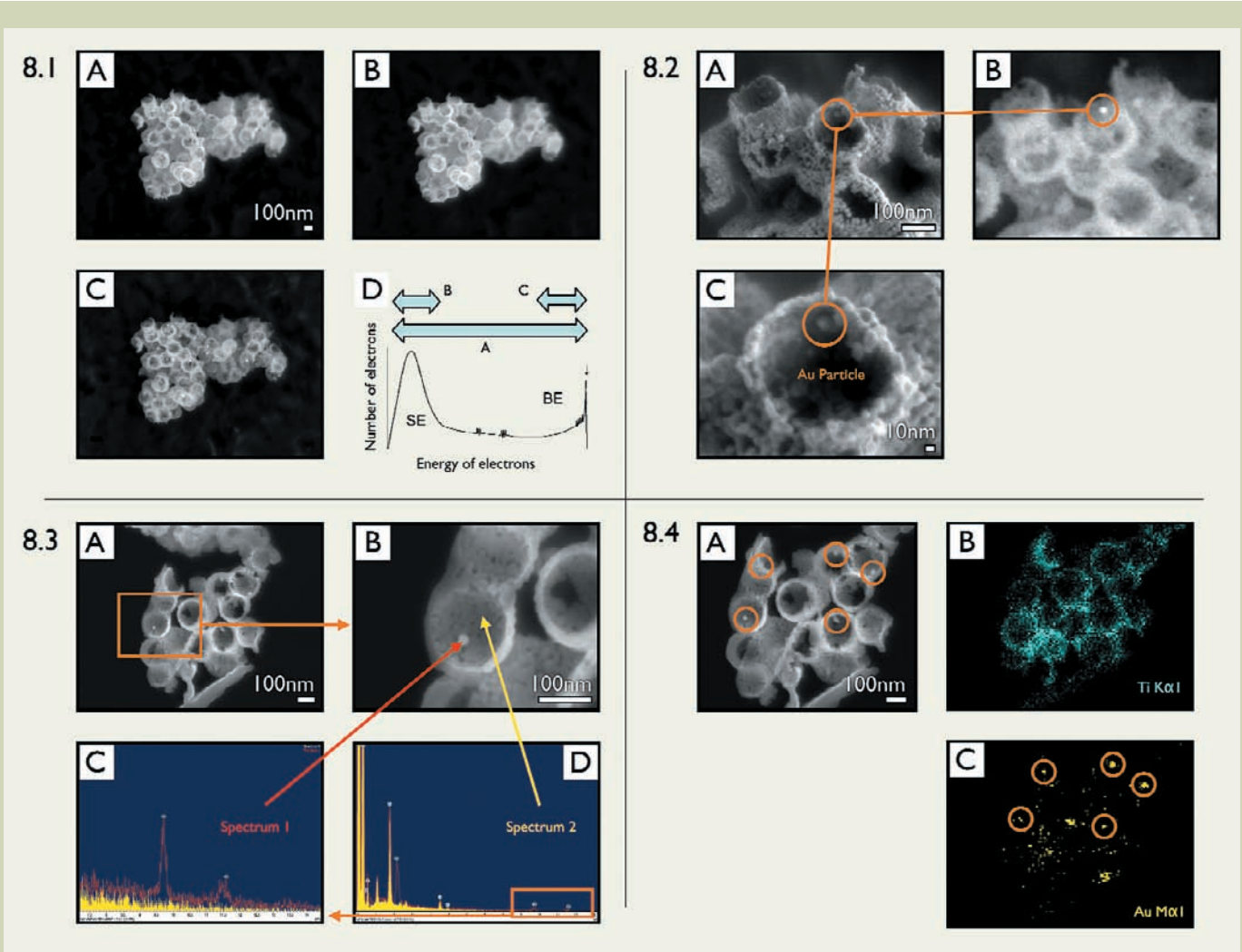


Fig.8.1 $Au@TiO_2$; Titanium nanoparticles creating interconnected macrospherical cavities, each encapsulating a gold nanoparticle. Images were taken at 3.0 kV with different ratios of SE (secondary) and BE (backscattered) electrons. Images constructed of only SE electrons (A), of a mixture of SE and BE electrons (Sb mode) using the r-Filter (B) and of only BE electrons (C).
8.2 A reduced landing energy of 500 eV (column energy 1.5 keV) produces topographical images (A and B) showing clearly the encapsulated gold (see as a compositional contrast change in top right image (C)- the position of the gold).
8.3 Confirmation, by EDS chemical analysis, of position of gold nanoparticle as found in Figure 8.2.
8.4 EDS mapping of spheres (A) showing titanium K-lines (B) and gold M-lines (C).

# Observation of Membrane Proteins Through An Electron Beam

**Yoshinori Fujiyoshi**

**Structural Physiology, Department of Biophysics, Graduate School of Science, Kyoto University**

Technological and instrumental advancements in electron microscopy have facilitated comprehension of structures of biological components. For example, electron crystallography of membrane proteins is now an established technique to analyze their structures in lipid bilayers which are close to the natural biological environment. By utilizing JEOL cryo-electron microscopes with originally developed helium cooled specimen stages, structures of membrane proteins were analyzed at a resolution better than 0.3 nm. Here some examples, such as water channels and gap junction channels, are discussed by focusing on their biological mechanisms through structural analyses of membrane proteins. Based on observation of structures of membrane proteins through an electron beam, we are trying to establish a new research field named structural physiology.

## Introduction

Electron microscopy made it possible to observe structures of biological components struggling against radiation damage by an electron beam. The induced problem caused by damage was avoided by staining and shadowing methods with many technological variations and these techniques have given us important structural knowledge about biological cells and tissues. Higher resolution analysis is however required to understand molecular mechanisms of biological functions, especially membrane proteins which were known to be key molecules for sensing and regulating signal transduction, and for keeping energy metabolism and functioning other activities of cells. While observation of these molecular structures at high resolution is essential, radiation damage to bio-molecules strongly restricts the resolution and forces us to average image signal to improve signal to noise ratio (S/N). As a powerful averaging technique using a computer, single particle analysis of cryo-electron microscopy is very widely used for structural studies of biological macromolecular complexes. The method gives us three-dimensional (3D-) structures without crystals, which are generally difficult to be grown, and is actively used for studying many important biological targets. Although the single particle method is growing into the most important technique in electron microscopy by achieving surely important structural analyses in a wide range of biological fields, there are some examples of inconsistent structures which were analyzed from a same sample by the same method. The analyzed resolution is also rather limited because of several difficulties of the method so far, while the single particle method has potential ability to reach a real atomic resolution.

On the other hand, electron crystallography is particularly a good candidate for structure analyses of membrane proteins in detail because of the following several reasons, while a rather smaller number of groups are so far interested in this method. 1) Structure can be analyzed in a membrane that gives environment for membrane proteins similar to native conditions. 2) Structure can be analyzed even by poor crystals while the resolution is strongly related to the quality of crystals. 3) Both sides of the crystal are kept open and have less influence from artificial crystal packing. This feature enables to use the freeze-trapping technique which was developed and actually used for studying the gating mechanism of Nicotinic Acetylcholine receptor (AChR) by N.Unwin [1]. 4) Phase for structure analysis is calculated directly from images and gives a better map than that of X-ray crystallography. Thus images and diffraction patterns of well-ordered, planar and tubular protein-lipid crystals are yielding atomic models, which show us how the proteins are designed in biological cells and function in native environment.

Electron crystallography for the first time gave us a real image of a membrane protein, bacteriorhodopsin whose structure was analyzed by R. Henderson and N. Unwin in 1975 [2]. Whereas this method is extremely powerful especially for structural study of membrane proteins as explained in the previous sentence and R. Henderson et al. analyzed for the first time an atomic structure of bacteriorhodopsin based on electron crystallography [3], this method has been spreading rather slowly in structural biology field presumably because of technological difficulties as well as difficulty of crystallization of proteins. I however believe electron crystallography could be the core method for establishing structural physiology because it enables us to analyze functional structures of membrane proteins in membrane layers at the high resolution that enables us to discuss physiological functions.

The radiation and dehydration sensitivities of biological molecules give us difficult challenge for high resolution structural study and these difficulties force us to develop an effective and stable cryo-electron microscope with a helium cooled specimen stage and a cryo-transfer system for ice embedded samples. Recent methodological as well as instrumental advances, and the inclusion of tomographic and cryo-sectioning techniques, are enabling detailed information to be obtained from increasingly more disordered and complex membrane assemblies, extending the potential of this approach.

## Development of stable and effective cryo-electron microscope

For high-resolution data collection, 2D-crystals are embedded in a thin layer of amorphous ice and/or a sugar solution for which trehalose is recommended [4]. The specimen is then mounted on the cryo-stage of an electron microscope using a cryo-transfer device. In

Oiwake, Kitashirakawa, Sakyo-ku, Kyoto, 606-8502, Japan

yoshi@em.biophys.kyoto-u.ac.jp

this case, the thickness of the ice layer has to be optimized for high resolution data collection, because the flatness of 2D-crystals is crucially important especially for data collection in the direction perpendicular to the tilting axis at a highly tilted condition as shown in **Fig. 1**. To make the crystal flat, a thinner ice layer is better as shown in **Fig. 2** but to the contrary, such a thin layer causes dehydration problem of sample. Namely, the best specimen preparation condition forms a very narrow hitting target and thus many trials are generally required for high resolution data collection, especially a resolution better than 0.3 nm. It is impossible to accurately regulate the best thin layer formation without dehydration because sample condition and other conditions, such as density of crystals, temperature and humidity, easily change the thickness of the water layer on the specimen grid. Therefore a cryo-electron microscope (cryo-EM) with a quick specimen exchange system and a stable stage, by which we can try many specimen preparation conditions, is inevitable. By the way, a multiple specimen loading system is not useful for this purpose because the optimization of water layer requires feedback procedure. We therefore developed a cryo-electron microscope with a stable helium stage as well as an effective cryo-transfer system by which we can take a 0.2 nm resolution image of a new sample just after finishing observation of the previous specimen in shorter than 10 minutes and therefore my own record of specimen exchange frequency in a day was 34 times.

The resolution of an image of a biological macromolecule is usually limited to a value much worse than 0.3 nm. This limitation is not due to the resolution of the instrument but to damage to the specimen by the electron beam. The irradiation damage to biological crystals was found to be reduced to about 1/10 to 1/20 with respect to the value at room temperature when the specimen was cooled to below 20K and 8K, respectively. We have therefore developed a super fluid helium stage that can achieve a resolution of 0.26 nm in 1991 [5]. Thermal shield by liquid Nitrogen and Helium tank is gold plated to minimize radiational heat. The pot cooling specimen is cooled down to 1.5K by superfluid helium and we call this a 1.5K pot. Although our target resolution of electron micrographs is some thing like 0.3 nm, an instrument yielding better resolution would be highly beneficial, because biological molecules consist mainly of light atoms that exhibit small atomic scattering factors in a high-resolution range. A resolution better than 0.25 nm might be required to identify water molecules. Then we improved the instrumental resolution to 0.2 nm and overcome the operational difficulties [6]. We could develop the third generation cryo-EM which is a mature instrument for electron crystallography (Fig. 3). We modified an effective cryo-transfer system for ice embedded specimens to an automatic one which is a user friendly system and is tested in our third generation cryo electron microscope. After the third generation cryo-EM, the fourth generation cryo-EM equipped with an automatic cryo-transfer system, a field emission gun and an omega filter was developed and the fifth generation cryo-EM was also developed mainly for the single particle method (**Fig. 3**). From the second generation cryo-EM, we made quite a bit effort to improve resolution as well as overcome operational difficulties of the cryo-EM with a top-entry type helium stage. Recently we developed a new cryo-microscope, the sixth generation cryo-EM with an outer control tilting device for electron tomography and some other analyses. We also improved the sixth generation cryo-EM to accommodate a eucentric top entry helium stage and this seventh generation cryo-EM is used for taking tomographic images (Fig. 3).

## Carbon Sandwich technique

When we attempted structure analysis of bacteriorhodpsin, we encountered a serious difficulty of image shift which could be induced by specimen charging, especially at tilted specimen conditions, resulting in a low probability to have good images. We took more than 10,000 bad images to get about 200 good images as shown in **Fig. 4**. This is the most serious problem for image data collection from the two-dimensional crystals of biological macromolecules. The image shift extinguishes optical diffraction spots perpendicular to the tilt axis even in a medium or low resolution area (Fig. 4). Almost all of the images from a tilted specimen prepared on a one-layer carbon support tend to be deteriorated by the image shift caused by beam-induced specimen charging. The success ratio for obtaining high resolution images from tilted specimens is therefore only 2% or so. To overcome the serious problem, the carbon sandwich preparation method, in which crystals are put between two sheets of carbon film, was investigated. When we used carbon sandwiched specimens, the ratio of images which showed clear asymmetric features in diffraction patterns due to the image shift was significantly decreased as compared to that obtained when the specimens was supported by a single carbon film. Thus, the carbon sandwich preparation method was confirmed to overcome the most difficult problem and contribute to more prompt structural analysis by electron crystallography [7].

Another benefit of the carbon sandwich technique was observed as shown by structure analysis of water channel aquaporin-(AQP)0. By the carbon sandwich technique, dehydration problem was minimized and the structure of AQP0 was analyzed at 0.19 nm [8]. At such a high resolution, lipid molecules in the AQP0 crystal were clearly discriminated as shown in **Fig. 5.**

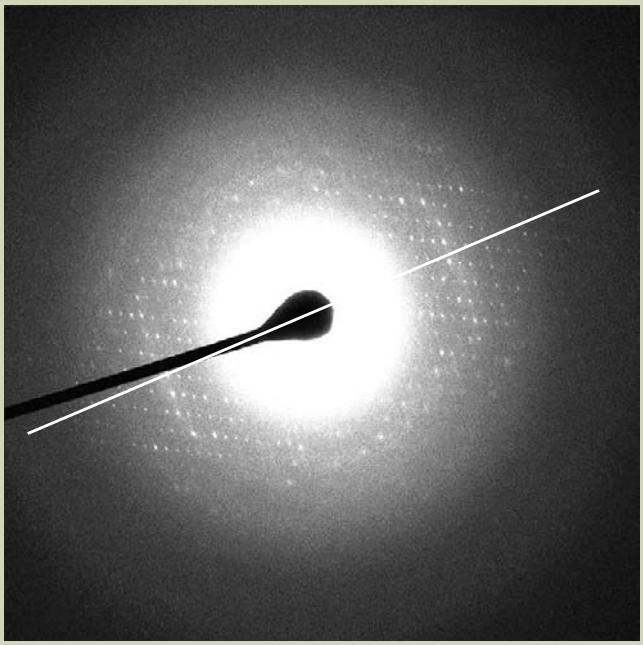

Fig. 1 Electron diffraction pattern of 2D-crystal of AQP4 at 60 degree tilt. White line indicates the tilt axis. Although diffraction spots at a resolution better than 0.2 nm are clearly observed in the direction of the tilting axis, spots perpendicular to the axis are blurred. The Blurring of diffraction spots could be attributed to the poor flatness of the crystal.

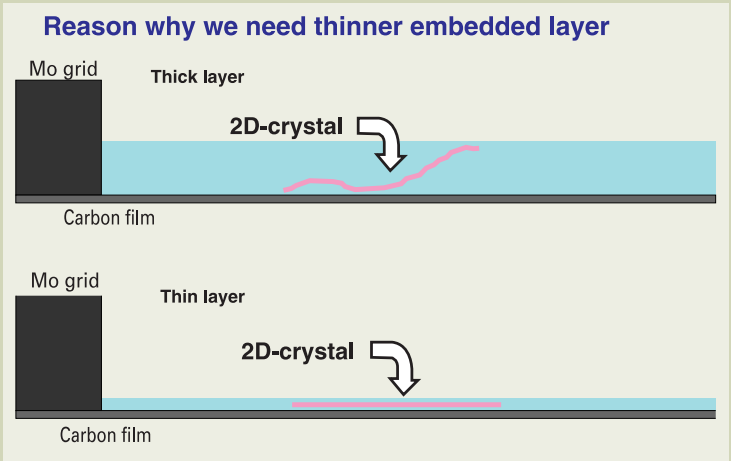


Fig. 2 Schematic drawing explaining the relationship between flatness of 2D-crystal and thickness of the embedded layer of it.

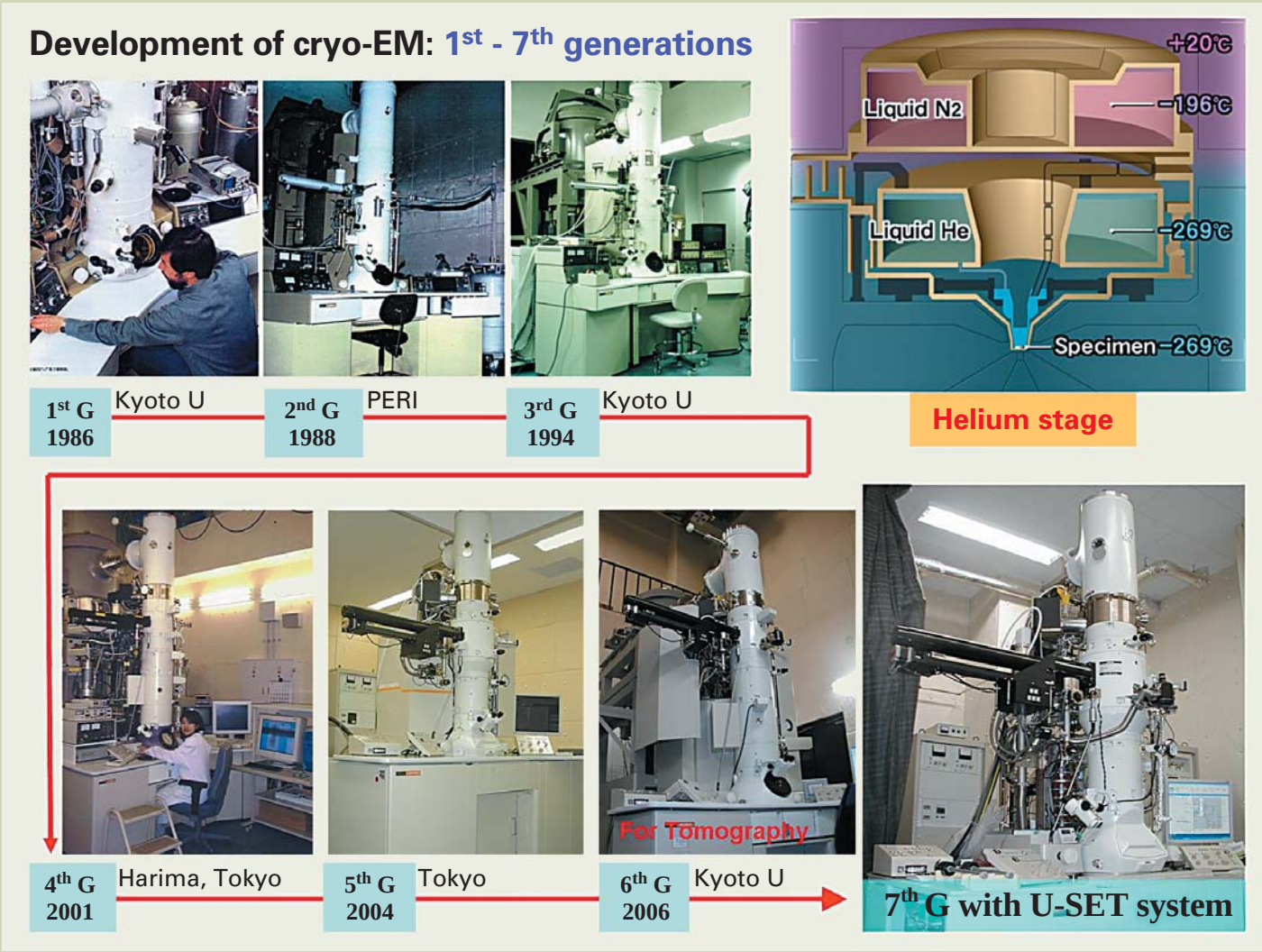


Fig. 3 History of development of JEOL cryo-electron microscopes with helium stage. From the first generation cryo-EM to the seventh generation one.

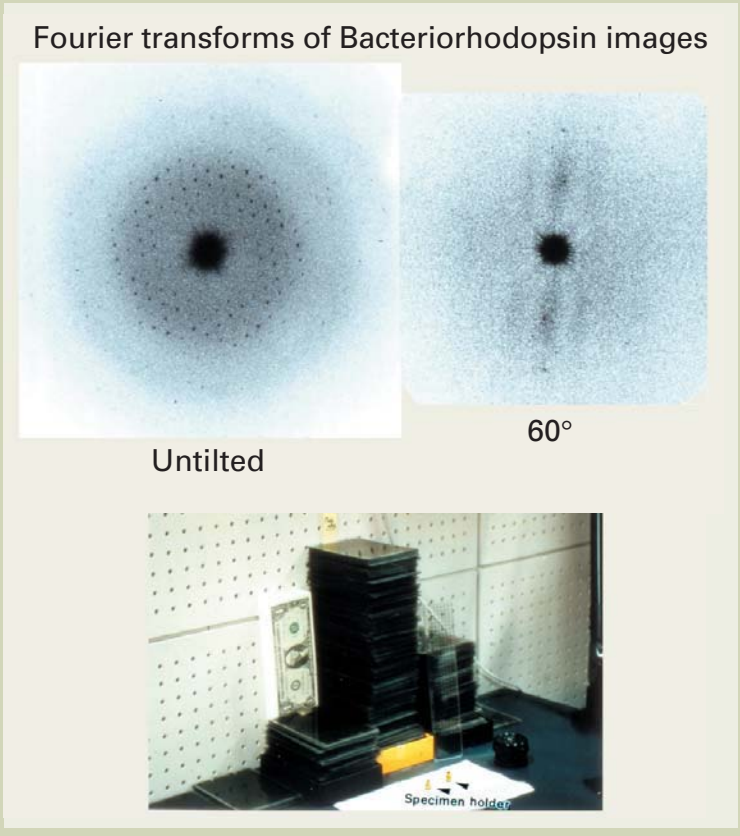


Fig. 4 At untilted condition, good quality images are relatively easy to be taken but at highly tilted condition, images tend to shift as shown in the upper optical diffraction patterns. We threw away more than 10,000 blurred images caused by the problem of charging for taking 200 good images. The lower photograph shows piling up EM films, all of which are bad images.

## Water channel aquaporin-1

Water is the most abundant molecule in any cells on the earth. The cell membranes therefore require an effective water channel function. In 1992, a 28kD membrane protein, which was eventually named AQP1, was identified in red blood cells and the water channel function was clearly shown in *Xenopus oocytes* [9] because only a limited amount of water can penetrate a simple lipid bilayer. The cell membrane exquisitely regulates entry and exit of ions because ion concentration and its dynamic change are strongly related with cell signalling functions. The water channels, therefore, need to keep ionic conditions in a cell, while these channels permeate a large amount of water. The pH regulation in the cell was well known to be also crucially important for cell functions. The AQP1 molecule attained effective water selective transport keeping the strict selectivity and it gave us puzzling questions. An atomic model analyzed at 0. 38 nm resolution by electron crystallography gave an answer to such puzzling questions and revealed a molecular contrivance of water selective channel [10]. The atomic model is interestingly a first structure of human source membrane proteins. For accomplishing the effective water channel functions, the structure showed peculiar structural determinants including an unusual fold (AQP fold) as shown in **Fig. 6**.

The handedness of the structure of aquaporin-1 was carefully examined and the right handed helical bundle structure of AQP1 was confirmed by using bacteriorhodopsin structure which was analyzed at an atomic resolution [11] before publication of a paper [12], because relatively low resolution, such as 0.6 nm, did not allow anyone to construct an atomic model but just assign a helix on a rod shape density and required confirmation of the handedness. The handedness was directly confirmed at a resolution of 0.38 nm or better at which an atomic model was constructed as shown in Fig. 6 in 2000 [10].

The critical function of AQP1 is exceptionally high water permeability, 2 billion water molecules per monomer per second. Almost all residues within a central 2 nm zone in the pore are highly hydrophobic, while one might expect that AQP1 has hydrophilic pore because of the water channel. A narrow part of the pore with about 0.3 nm in diameter is located at the middle of the membrane where short helices HB and HE interact with each other especially with proline 77 and 193 of the conserved NPA sequences. Despite the enormous capacity for water conductance, the AQP1 pore also exhibits marked selectivity. Water molecules were found to be strongly oriented in the channel interior, through alignment of their dipoles with the electric field exerted by the protein, causing water molecules to rotate by 180 degrees upon passage [10]. Two major interaction sites for water molecules were identified inside the channel:

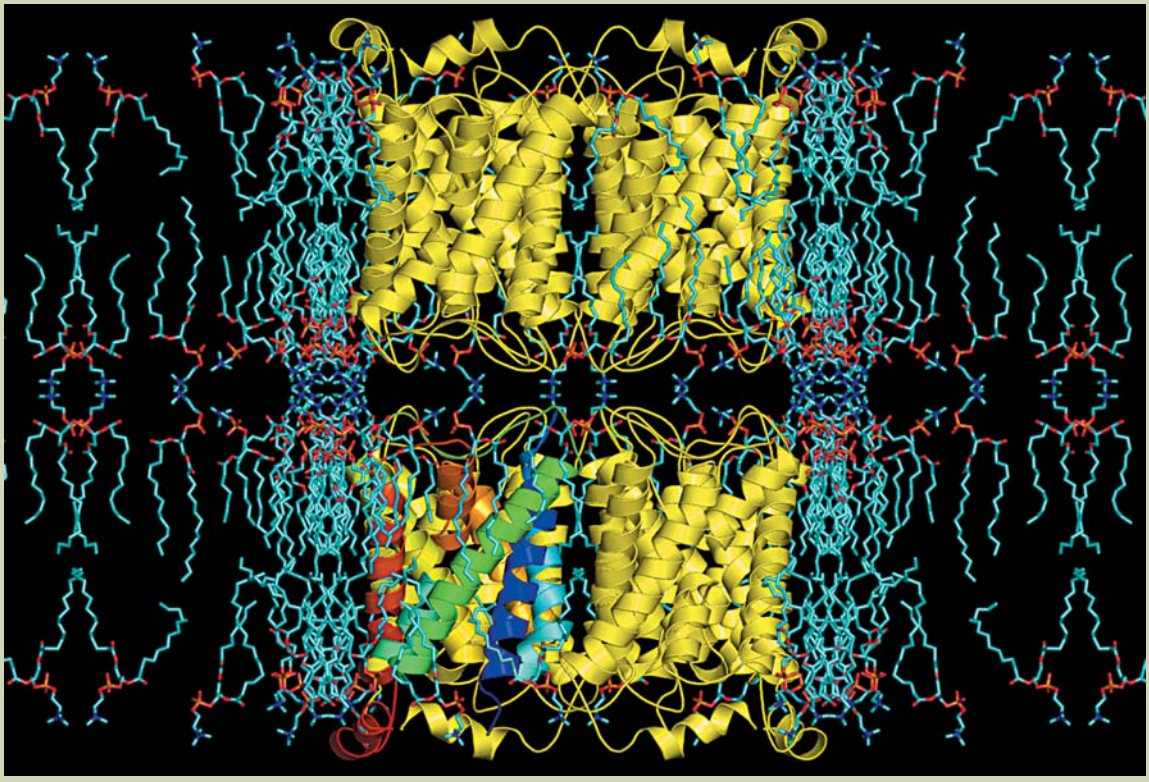

Fig. 5 Structure of AQP0 and lipid molecules in the 2D-crystal which is a double layered crystal.

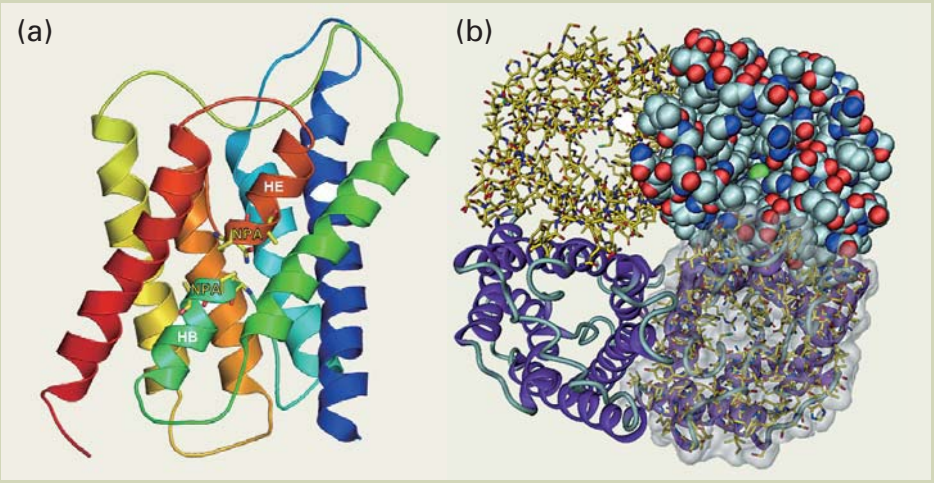


Fig. 6 Structure of AQP1 monomer (a) and tetramer (b) analyzed by electron crystallography. (a) shows characteristic AQP-fold. (b) shows end on structure with four different types of representation.

Fig. 7 Schematic drawing of the water channel, AQP1 explaining water selectivity and fast water permeation through the channel.

the NPA and ar/R regions. The two highest enthalpic barriers for water molecules are located directly adjacent to the NPA region. This, together with the water rotation that is centered also here, renders the NPA region a major selectivity filter as shown in **Fig. 7**. This mechanism was named as hydrogen bond isolation mechanism [10]. Contiguous hydrogen-bonded water chains are known to be efficient proton conductors. Aquaporin must prevent proton conduction along its pore, to maintain the proton gradient across the cell membrane that serves as a major energy storage mechanism. Water regulation is crucially important for every cells and therefore for all life forms on the earth. Unexpected structural features, such as right handed helical bundle and hydrophobic channel wall, were revealed to facilitate the water transport through the channel. All of these findings were impossible to predict without structure analysis at high resolution.

## Structure analysis of AQP4

AQP4 is the predominant water channel in the mammalian brain and we determined the AQP4 structure by electron crystallography of double-layered, two-dimensional (2D-) crystals. Analysis of the AQP4 structure was complicated by variations in the double-layered 2D crystals in terms of lateral alignment and distance between the two layers. Despite the high resolution of 0.32 nm, electron diffraction data proved not sufficiently sensitive to distinguish between different crystal variants. Phase data extracted from images even at medium resolution, on the other hand, were sensitive enough to discriminate between crystals with different arrangements of the two layers. The use of a helium-cooled electron microscope [6] and the carbon sandwich specimen preparation technique, which significantly increases the yield of good images [7], allowed us to also take an image of each crystal that produced a high-resolution diffraction pattern. Classification based on the image data, which provided phase information to better than 0.6 nm, identified one predominant crystal type, which accounted for about 70% of the analyzed crystals that yielded a high quality electron diffraction pattern. In this crystal type, the two layers have a spacing of 4.5 nm (molecule center to molecule center). The final intensity data set at 0.32 nm resolution was used to determine the AQP4 structure by molecular replacement using the AQP1 structure. The images (recorded after the corresponding electron diffraction patterns and used for classification) were also used to calculate a density map and confirmed the consistency of our structure.

Glial cells contain characteristic orthogonal arrays in the plasma membrane, which are especially prominent in glial end feet surrounding vascular capillaries in the brain. Immunogold labeling experiments showed that these arrays consist of AQP4 [13]. While AQP4 and AQP1 both function as very fast water-selective pores, AQP4 has distinctive biological characteristics as it forms orthogonal arrays in intact membranes. Furthermore, AQP4 exists in glial cells as a full-length protein starting with Met1 (AQP4M1) and an alternative shorter splicing isoform that starts with Met23 (AQP4M23). The structure allows us to discuss how the expression ratio between the long and short AQP4 splicing variant can determine the size of *in vivo* orthogonal arrays as shown in **Fig. 8**a [14].

AQP4 is also expressed in glial lamellae of the hypothalamus, where it may play a role in osmo-, thermo- and glucose-sensing. In glial lamellae the plasma membrane forms large junctions between individual layers, which have been shown to contain AQP4. Interestingly, another water channel, AQP0, forms the "thin junctions" between fiber cells. Structure analysis of AQP4 by double layered 2D-crystals revealed that the molecule contains a short $3_{10}$ helix in an extracellular loop, which mediates weak but specific interactions between AQP4 molecules in the adjoining membrane [14]. This finding suggests a previously unexpected role for AQP4 in cell adhesion as shown in Fig. 8b. This notion was corroborated by expression of AQP4 in L-cells, which resulted in clustering of the cells. Our AQP4 structure thus enables us to propose models for the size regulation of orthogonal arrays and channel-mediated cell adhesion as observed in glial lamellae of the hypothalamus. AQP4 membrane junctions may reduce the water permeability of glial cell plasma membranes, because the tight tongue-into-groove packing of the two crystalline layers results in a partial blockage of the extracellular pore entrances (Fig. 8b). While the packing of the AQP4 tetramers in the junctions must create resistance for water flowing across the two membranes, rapid water flow through the channels may also reduce the adhesion between adjoining membranes. This may establish the basis for a role of AQP4 in osmo-sensing. For example, a high AQP4M1/AQP4M23 expression ratio would produce small AQP4 arrays providing weak adhesion between membranes, which could easily be separated and thus react to small water flows resulting from small osmotic differences. A low AQP4M1/AQP4M23 expression ratio, on the other hand, would result in extensive AQP4 arrays providing relatively strong adhesion between membranes that would withstand large water flows associated with large osmotic differences. Although further experiments are needed to elucidate the interplay of the two functions in aquaporins and potentially other membrane channels with adhesive properties, we propose to name "adhennels" for adhesive water and ion channels [14].

## Higher resolution analysis of AQP4

Based on the electron crystallographic structure of AQP1, the hydrogen bond isolation mechanism was proposed to explain why AQPs are impermeable to protons despite their very fast water conduction. The mechanism by which AQPs exclude protons remained, however, is controversial. Therefore we present the structure of AQP4 by electron crystallography of double-layered two-dimensional crystals improving resolution from the previous 0.32 nm to 0.28 nm with an accompanying improvement in data quality resulting in the

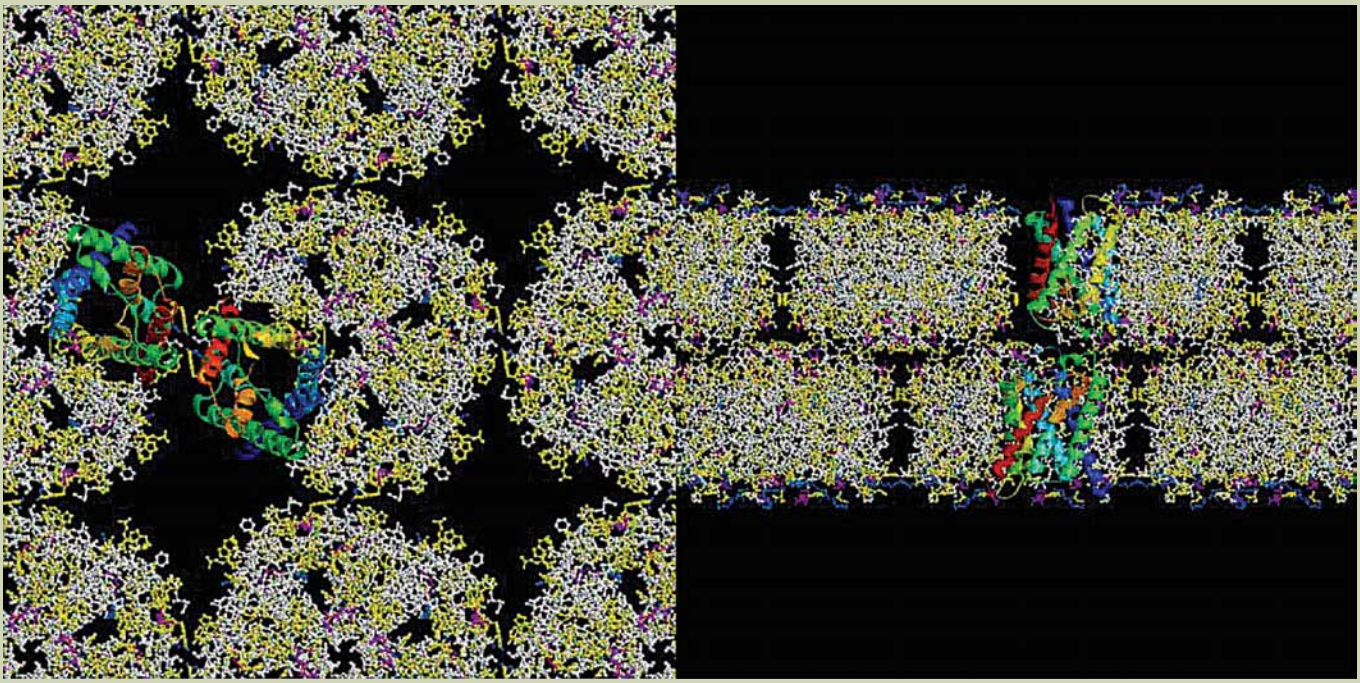

Fig. 8 Structure of AQP4 analyzed at 0.32 nm resolution. End on view (a) and a double layered structure of 2D-crystal of AQP4.

ability to identify seven individual water molecules in the channel as shown in **Fig. 9**a [15]. In addition, the Fo-Fc map showed an additional spherical density at the ar/R constriction site. Since the side chains of AQP4 around the ar/R region were represented by clear density (Fig. 9a) and the atoms of the protein molecule had low temperature factors in this region, we assigned an eighth water molecule to the spherical density at the ar/R site. The narrow diameter at this constriction would make it an unfavorable position for a water molecule, potentially explaining the weak density for the water at this position. The two neighboring water molecules on either side of the ar/R constriction, which form hydrogen bonds with the unstable water molecule in the constriction, showed higher temperature factors (35 Å$^2$) compared to those of all the other water molecules in the channel (2.9 Å$^2$ to 13.2 Å$^2$) (Fig. 9b). The temperature factor of each water molecule in the channel is indicated at the right side of Fig. 9b.

In X-ray crystallography, a resolution of 0.28 nm would be considered too low to see water and lipid molecules, but our density map resolved all water molecules in the channel as well as five lipid molecules as shown in **Fig. 10**. The B-factors of the water molecules in the pore are lower than 40 Å$^2$ (Fig. 9b), significantly lower than those of water molecules seen in membrane protein structures determined by X-ray crystallography. Since every exposure with the electron beam causes severe radiation damage to the specimen, each 2D crystal can only be used to collect one high-resolution image or electron diffraction pattern. Thus, to analyze the 3D structure of a membrane protein, data have to be collected from hundreds of 2D crystals, which has been considered a disadvantage of electron crystallography. However, our density map obtained by electron crystallography clearly, and counter-intuitively, resolved seven spherical densities that could be assigned to water molecules (Fig. 9a). The perceived weakness of electron crystallography, that data are collected from many different crystals, may in fact work in our favor. We collected more than a thousand diffraction patterns but selected only the 199 very best patterns [15], so that the final data set includes only information from the very best crystals. Furthermore, while we saw diffraction spots to a resolution of 0.19 nm, we truncated the resolution of our density map to 0.28 nm. Due to these procedures the final lattice line data were of exceptionally high quality.

Although we tried to prepare the specimens as consistently as possible during the months of data collection, there must have been variations among the specimens. As a consequence, our map represents an average of the specimen under various, slightly different conditions. As we were still able to resolve water molecules in the channel, these are presumably in defined positions. This notion is corroborated by the low temperature factors of the waters, ranging from 2.9 Å$^2$ to 35.3 Å$^2$ (Fig. 9b), which are significantly lower than those of the surrounding peptide main chain atoms. The same phenomenon was observed in the electron crystallographic structure of AQP0 at 0.19 nm [8]. The B-factor of the water molecule associated with the amide groups of the NPA motifs is 1.7 Å$^2$, while those of the surrounding main chain atoms are in the range of 30 Å$^2$ to 40 Å$^2$. The large difference in the B factors between the water and protein atoms might be due to the characteristic features of electron crystallography and/or the enhancement of the effect of the helical dipole moments due to the lipid environment. In X-ray structures of AQPs in detergent micelles, the water molecules sometimes also displayed lower temperature factors compared to those of the surrounding main chain atoms, but the difference is usually less than 20 Å$^2$. Another possible reason why we could observe water molecules in the AQP4 channel could be attributed to the data collection at liquid helium temperature. We collected all data for this structure analysis at stage temperature of 4.2K and such a low temperature could give clearly the lowest energy positions for water molecules in the channel.

The eight water molecules in the AQP4 channel are in a single-file arrangement (Fig. 9a, b). From the measured distances between successive water molecules in the channel (Fig. 9a), all water molecules appear to form hydrogen bonds with their neighbors (red dotted lines in Fig. 9b), except for the water at the NPA site and the one below it. These two waters thus seem to be separated from the other water molecules in the channel, lending support to the hydrogen bond isolation mechanism. The inside surface of water channels is largely hydrophobic except for a narrow, hydrophilic belt formed by the oxygen atoms of the main chain carbonyl groups of

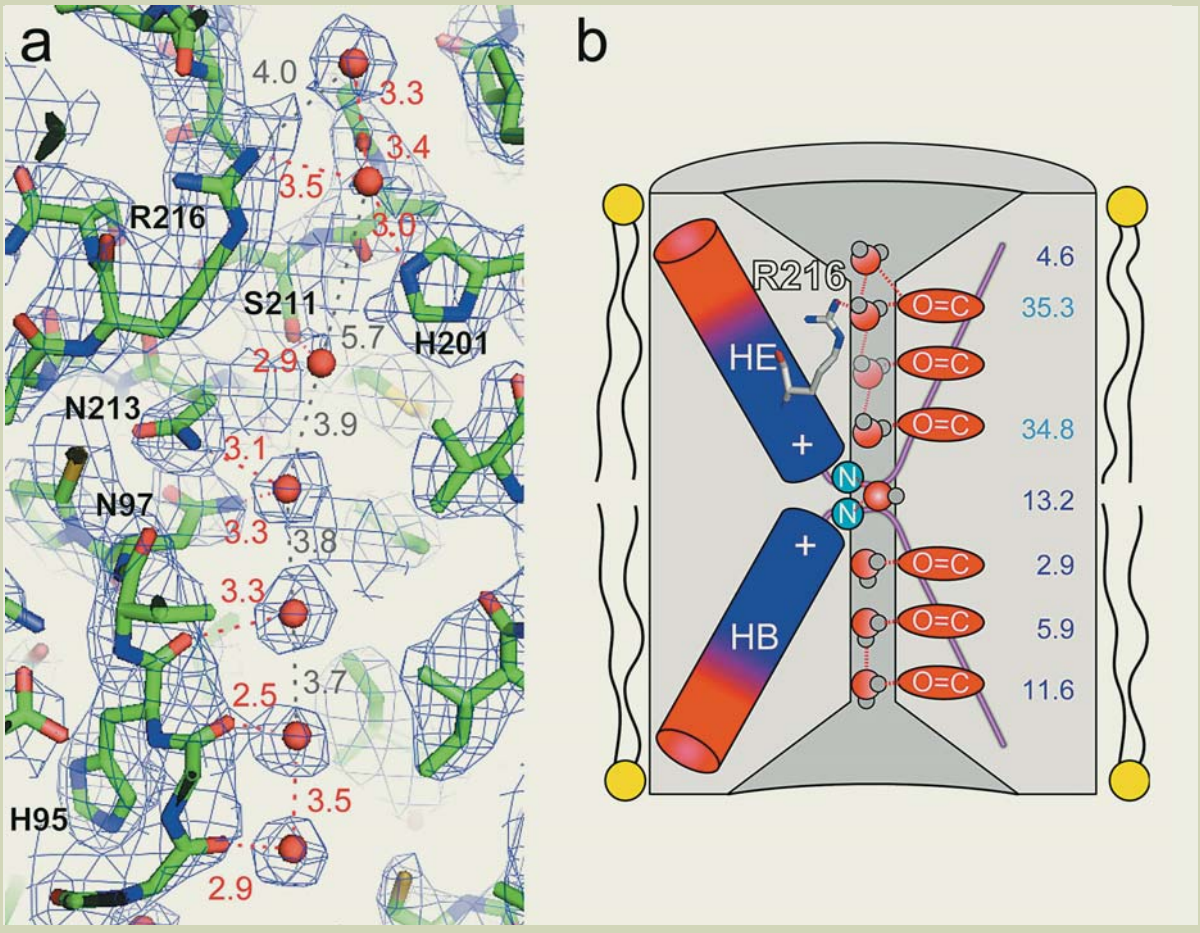


Fig. 9 Water molecules in AQP4 channel analyzed by electron crystallography at 0.28 nm resolution (a) and schematic drawing of the channel which explain the Hydrogen bond isolation mechanism. Temperature factor of each water molecule is indicated at the right side (b).

Gly209, Ala210, Ser211, His95, Gly94 and Gly93 and the nitrogen atoms of the side chain amide groups of Asn213 and Asn97 of the NPA motifs. The line of mechanically stable carbonyl groups provides "a guide rail" of hydrogen bonding partners for the hydrogen atoms of the permeating water molecules as illustrated by the red ovals in the schematic drawing shown in Fig. 9b. Each water molecule in the single file can thus form two or three hydrogen bonds. Since water in bulk solution usually forms three or four hydrogen bonds with neighboring water molecules, water molecules entering the channel only have to sacrifice a single hydrogen bond, an energy cost of about 3 kcal (per mole). The arrangement of carbonyl and amide groups in the AQP4 channel thus dramatically lowers the energy barrier for water molecules entering the narrow AQP channel and allows for the very fast water permeation through the otherwise hydrophobic channel.

The NPA motifs and the arrangement of the carbonyl groups in the hydrophobic channel together with the arrangement of the two short pore helices HB and HE are crucially important to break the hydrogen bond network, which prevents proton conduction while maintaining fast water permeation. The ar/R constriction site is important for blocking $H_3O^+$ but not for the separation of hydrogen bonds. Our higher-resolution structure of AQP4 supports the hydrogen bond isolation mechanism, which has previously been proposed based on the lower-resolution structure of AQP1 [10] to explain the puzzling mechanism by which water channels can conduct water at very high speed while completely blocking proton permeation.

## Gap junction channel

Gap junctions contain intercellular communication channels that allow a wide variety of solutes with different sizes to be transferred between the cytoplasm of adjacent cells. These solutes include ions, metabolites, nucleotides, peptides, and secondary messengers. Gap junction channels have critical roles in many biologically important processes including cardiac

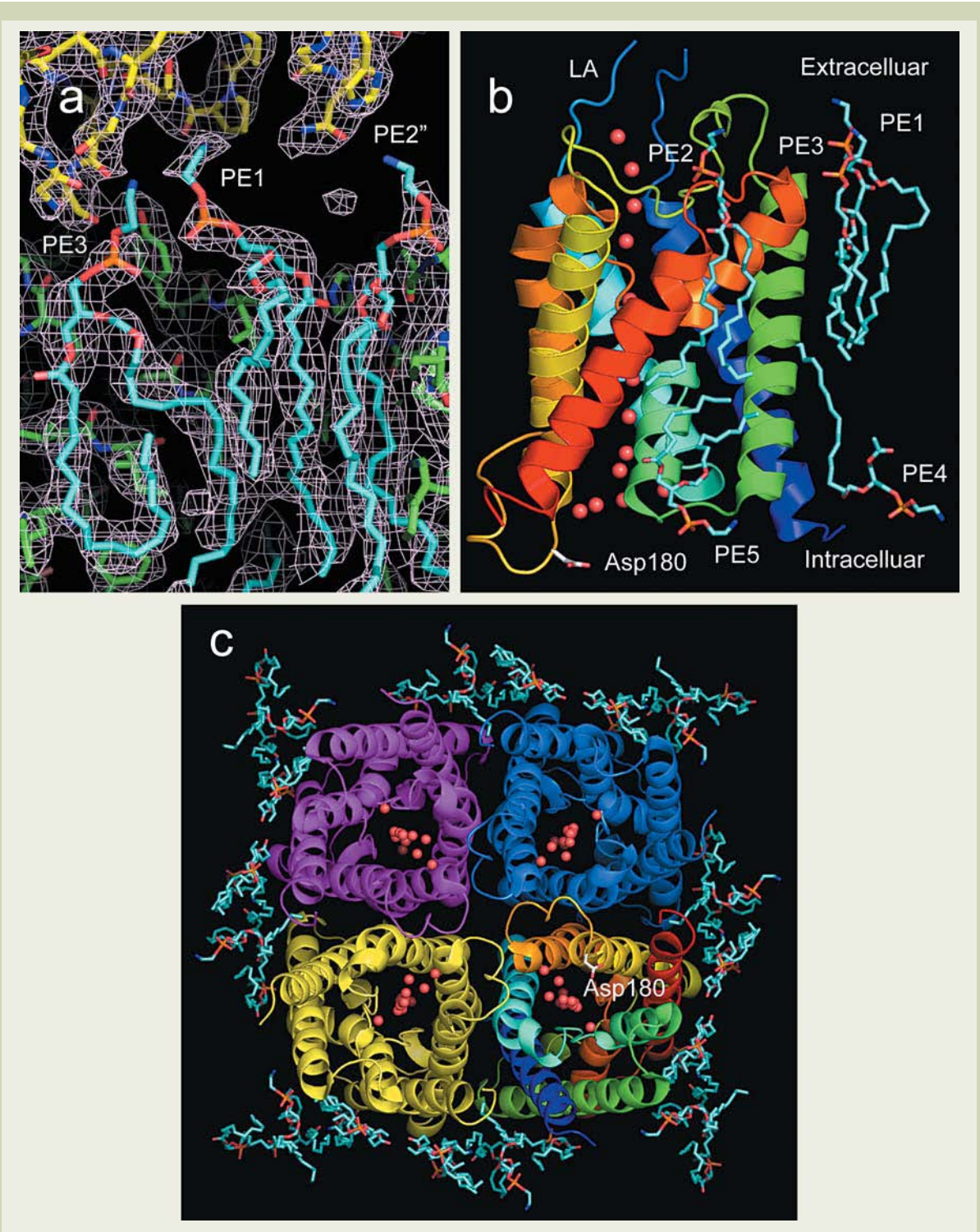


Fig. 10 Structure of lipid molecules and AQP4 analyzed by electron crystallography at 0.28 nm resolution.

development, fertility, the immune system, and electrical signaling in the nervous system. The diversely expressed Connexin26 (Cx26) is the second smallest member of the conserved mammalian gap junction protein family.

We focus on the structure of Cx26 gap junction channels and used a site specific mutant of human Met34, hCx26M34A, because this mutant expresses in baculovirus infected Sf9 cells at higher quantities than wild type Cx26 infected cells. The hCx26M34A mutant is a single site mutation at the same position as the hCx26M34T mutant, which can cause prelingual non-syndromic hereditary deafness [16]. Although the purified hemichannel is hexameric, the 2D arrays obtained by dialysis showed an orthorhombic crystal lattice. A side view of the 3D map reveals that the crystals have a thickness of about 24 nm and contain three lipid bilayers (labeled Mem-1, Mem-2 and Mem-3 in **Fig. 11**a). Remarkably, the map also shows that the hemichannels re-docked through their extracellular surfaces forming complete gap junction channels (Fig. 11b). This is consistent with published results proposing extensive hydrophobic surfaces in the gap region. In bilayers Mem-1 and Mem-3, the hemichannels show poorer density than in Mem-2 (Fig. 11c, d), presumably because of variability in the molecular packing due to the large cytoplasmic domains of the connexin subunits. The cytoplasmic structures in Mem-1 and Mem-3 may also be deformed by their contact with the carbon film to which the crystals are adsorbed in the sample preparation procedure for cryo-electron microscopy. By contrast, the hemichannels in Mem-2 are protected from any forces such as the surface tension upon specimen drying and mechanical interactions with the carbon film. Therefore, the structural features of the hemichannels in Mem-2 should be the most accurate and, in particular, preserve the structure of the flexible cytoplasmic domains of the connexins. Thus, the description of the gap junction structure is based on the hemichannels in Mem-2 unless noted otherwise.

The 3D map shows a novel density in the center of the pore (upper left of **Fig. 12**) [17]. Since this density was dramatically reduced in the structure of N-terminal deletion mutant, it was confirmed that the plug was formed by N-terminal helices of six subunits in the hemichannel. The plug is located inside of the membrane layer and forms contacts with the surrounding channel wall as shown in the upper left figure (Fig. 12), which at the constricted part of the vestibule is formed by the innermost helices 1 (Fig. 12-2). This density strongly suggests that a plug physically blocks the channel within the membrane. Each hemichannel has its own plug, conferring it the ability to gate its pore autonomously. It is possible that the transjunctional voltage sensor and the physical gate reside exclusively within a single hemichannel.

Our Cx26 gap junction crystal structure shows that the channel vestibule is blocked by a physical obstruction which we call the "plug". Structure analyzed by X-ray crystallography at higher resolution of the open state [18] provide more structural detail and supported our plug gating mechanisms in these widely expressed channels.

## Conclusions

The ability of electrons to form images, combined with advances in cryo-technology, are enabling us to acquire detailed structural and chemical information about membrane proteins in their physiological lipid and ionic settings as shown in **Fig. 13** where structures of membrane proteins analyzed by electron crystallography were indicated. This information complements that obtained by x-ray diffraction of proteins in detergent, where biological relevance of the structure is less certain. The development of cryo-electron tomography and real-space averaging methods together with instrumental developments such as the seventh generation cryo-EM will be extending the possibilities of obtaining high resolution information from increasingly complex protein-lipid arrays, and from membrane specialisations *in situ*.

## Acknowledgements

These studies were performed in a nice collaboration with many researchers whose names were recorded as authors in each referenced paper. The author thanks Dr K. Tani for preparation of figures. These works were supported by Grants-in-Aid for Specially Promoted Research and NEDO.

## References

[1] Unwin, N: *Nature*, **373**, 37-43 (1995).
[2] Henderson R, Unwin PN: *Nature*, **257**, 28-32 (1975).
[3] Henderson R, Baldwin JM, Ceska TA, Zemlin F, Beckmann E, Downing KH: *J. Mol. Biol*., **213**, 899-929 (1990).
[4] Hirai T, Murata K, Mitsuoka K, Kimura Y, Fujiyoshi Y: *J. Electron Microsc*., **48**, 653-658 (1999).
[5] Fujiyoshi Y, Mizusaki T, Morikawa K, Yamagishi H, Aoki Y, Kihara H, Harada Y: *Ultramicroscopy*, **38**, 241-251 (1991).
[6] Fujiyoshi Y: *Adv. Biophys*., **35**, 25-80 (1998).
[7] Gyobu N, Tani K, Hiroaki Y, Kmegawa A, Mitsuoka K, Fujiyoshi Y: *J. Struct. Biol*., **146**, 325-333 (2004).
[8] Gonen T, Cheng Y, Sliz P, Hiroaki Y, Fujiyoshi Y, Harrison SC, Walz T: *Nature*, **438**, 633-638 (2005).
[9] Preston GM, Carroll TP, Guggino WB, Agre P: *Science*, **256**, 385-387 (1992).
[10] Murata K, Mitsuoka K, Hirai T, Walz T, Agre P, Heymann JB, Engel A, Fujiyoshi Y: *Nature*, **407**, 599-605 (2000).
[11] Kimura Y, Vassylyev DG, Miyazawa A, Kidera A, Matsushima M, Mitsuoka K, Murata K, Hirai T, Fujiyoshi Y: *Nature*, **389**, 206-211 (1997).
[12] Walz Y, Hirai T, Murata K, Heymann JB, Mitsuoka K, Fujiyoshi Y, Smith BL, Agre P, Engel A: *Nature*, **287**, 624-627 (1997).
[13] Rash JE, Yasumura T, Hudson CS, Agre P, Nielsen S: *Proc. Natl. Acad. Sci. USA*, **95**, 11981-11986 (1998).
[14] Hiroaki Y, Tani K, Kamegawa A, Gyobu N, Nishikawa K, Suzuki H, Walz T, Sasaki S, Mitsuoka K, Kimura K, Mizoguchi A, Fujiyoshi Y: *J. Mol. Biol*., **355**, 628-639 (2006).
[15] Tani K, Mitsuma T, Hiroaki Y, Kamegawa A, Nishikawa K, Tanimura Y, Fujiyoshi Y: *J. Mol. Biol*., in press (2009).
[16] Oshima A, Tani K, Hiroaki Y, Fujiyoshi Y, Sosinsky GE: *Proc. Natl. Acad. Sci. USA*, **104**:10034-10039 (2007).
[17] Maeda S, Nakagawa S, Suga M, Yamashita E, Oshima A, Fujiyoshi Y, Tsukihara T: *Nature*, **458**, 597-602 (2009).

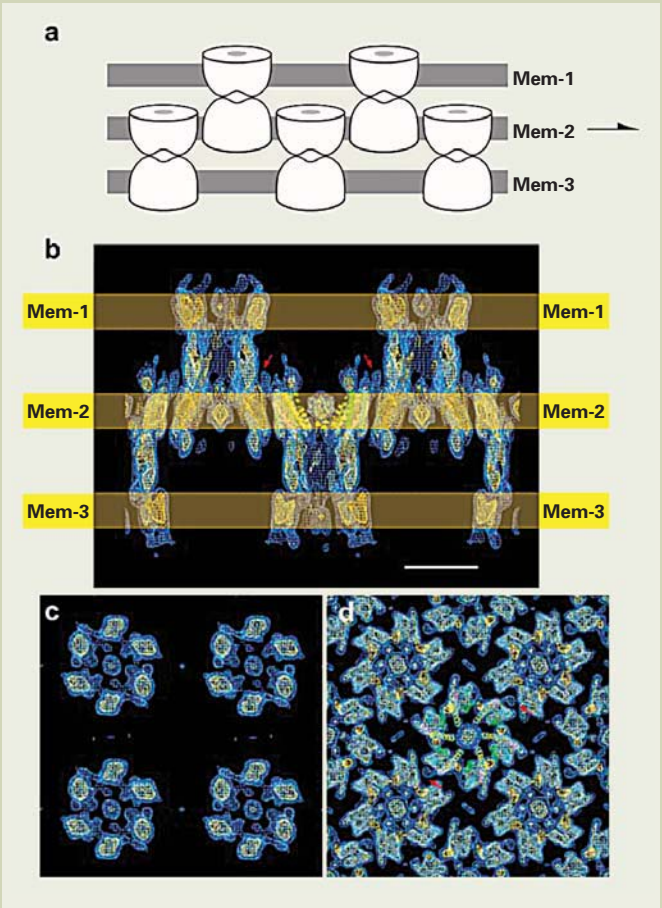


Fig. 11 Three membrane layered structure of 2D-crystal of gap junction channel, Cx26.

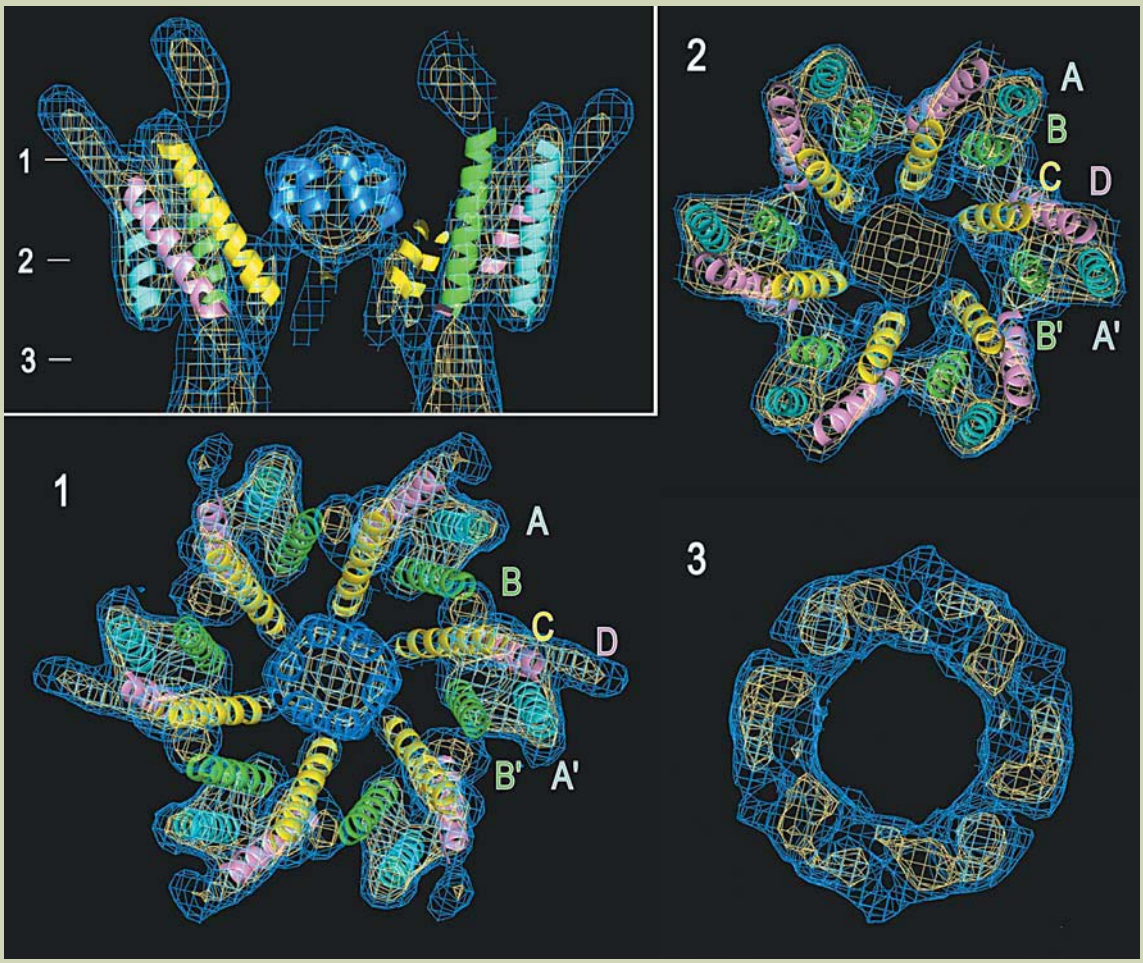


Fig. 12 Structure of Cx26. Upper left figure indicates sectional image perpendicular to membrane surfaces and numbers (1-, 2-, and 3-) at the upper left show the position of each sectional image parallel to the surfaces.

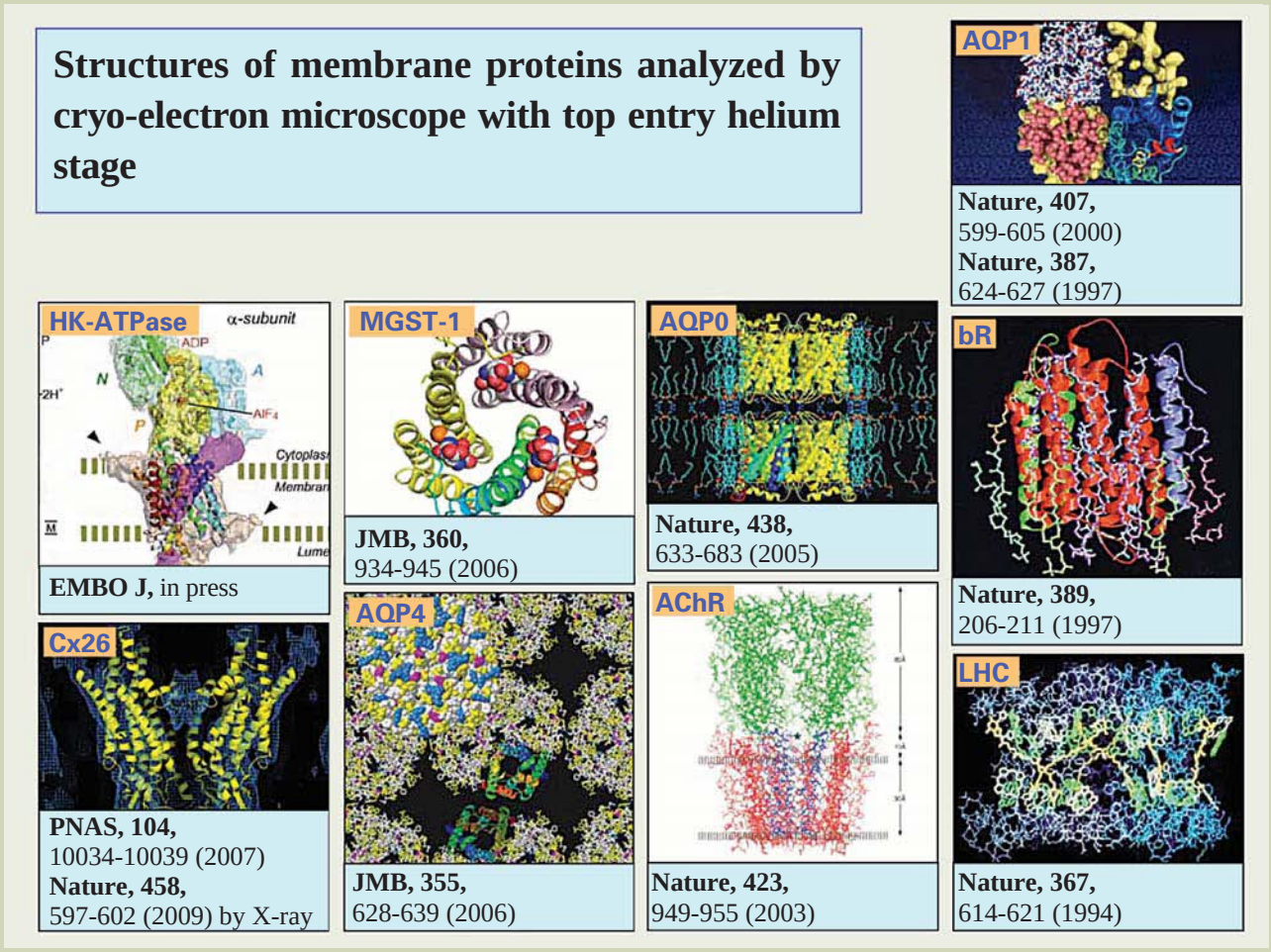


Fig. 13 Structures of membrane proteins analyzed by utilizing our cryo-EM systems.

# HR-TEM of Carbon Networks - Towards Individual C-C Bond Imaging -

**Kazu Suenaga, Yuta Sato, Zheng Liu, Masanori Koshino and Chuanhong Jin**

**National Institute of Advanced Industrial Science and Technology (AIST)**

Here we show some examples for atomic-level characterization of carbon nanostructures by means of a Cs-corrected HR-TEM operated at 120 kV. *In situ* imaging of the hexagonal network of carbon nanotube enables us to visualize the active topological defects, such as pentagons and heptagons, which are responsible for the plastic deformation of carbon nanotube. A single atomic chain of conjugated carbon (...-C=C-C=C-...) has been also successfully imaged and the *cis-/trans*-isomerization of retinal molecules is clearly identified. Individual molecular imaging has been also demonstrated for fullerene molecules and their derivatives. The structure and orientation of $C_{60}$ and $C_{80}$ molecules can be successfully identified at a single-molecular basis. Some recent progress for *in situ* observation of the carbon nanotube/fullerene growth and the defect dynamics is also presented.

## Introduction

The diversified properties of carbon nanostructures (nanotubes, graphenes, fullerenes and their derivatives) are related to their polymorphic arrangement of carbon atoms. Therefore the direct observation of carbon network is of great consequence in both scientific and technological viewpoints in order to predict the physical and chemical properties of carbon nano-structures. In order to identify the local configuration of pentagons and hexagons in carbon nanostructures, an electron microscope with higher spatial resolution and higher sensitivity is definitely required. Since the spatial resolution of the conventional TEM is limited by the spherical aberration coefficient (Cs) of its objective lens and the wave length ($\lambda$) of the incident electron beam, the Cs must be minimized to achieve the best performance because the reduction of the $\lambda$ is detrimental to the carbon based materials due to the higher knock-on probability. Lowering accelerating voltage is also beneficial to achieve the high sensitivity necessary to visualize individual carbon atoms. The spatial resolution of 0.14 nm (a typical C-C bond length) obtained at a moderate accelerating voltage can offer us a great advantage because we can realize the visualization of carbon atomic arrangement without massive electron irradiation damage.

## Experimental

A high-resolution transmission electron microscope (HR-TEM, JEOL JEM-2010F) equipped with a post-specimen aberration corrector (CEOS) was operated at a moderate accelerating voltage of 120 kV. The Cs was set to 0.5 ~ 10 μm in this work. The HR-TEM images were obtained under a slightly under-focus condition ($\Delta f$ = -2 to -7 nm) where a point resolution better than 0.14 nm was achieved at 120 kV. A CCD camera (Gatan 894) was used for the digital recording of the HR-TEM images. A typical exposure time is 0.5 ~ 1.0 sec for each frame and some of the frames are superimposed after drift-correction to enhance the contrast if necessary. In a typical high dose condition (~ 100,000 electrons/nm$^2$), the contrast of single carbon atoms can be well isolated with a SN ratio > 3, which guarantees us a confidence level of 80% for single carbon atom detection. A piezo-driven stage with a mobile electrode (Nanofactory) was used for *in situ* experiment of the carbon nanostructure growth.

## Defects in carbon nanotube

The physical properties of carbon nanotubes are strongly dependent on its chirality as well as atomic defects. The chiral index (*n, m*) for individual single wall carbon nanotubes (SWNTs) can be determined by either electron diffraction or HR-TEM [1, 2]. A great advantage of HR-TEM lies in its capability to determine the atomic defects as well [3]. Such defect structures of carbon materials have long been of great scientific and technological importance especially for nuclear research. Although single vacancies, topological defects, interstitials and their combination were theoretically predicted, no experimental evidence for these defects can be provided until they are directly identified. In order to visualize faithfully the atomic structures of carbon nanotubes, a high spatial resolution (~0.14 nm) is indispensable to resolve a typical C-C bond in the carbon networks. **Fig. 1**(a) shows a HR-TEM image of a single-wall carbon nanotube (SWNT). One can easily see the zig-zag chains contrast (0.21 nm apart) all over the SWNT. Especially in the region of a red rectangle the hexagonal structures of the carbon network are clearly recognized (Fig. 1(b)). Note that the hexagonal structure is only partly visible because the local distortion and/or inclination of the tube to the incident electron beam can largely critically affect the imaging conditions. By comparing the HR-TEM image with the image simulation and the structural model (Fig. 1(c) and 1(d)), the examined SWNT is proved to have a zig-zag structure with the index of (18, 0) and is slightly rotated around the tube axis (~ 2 degree). A contrast line profile along the two neighboring carbon atoms is shown in Fig. 1(e). The red dotted curve obtained from the line profile (experiment) in Fig. 1(b) is fitted with the blue line profile (model) in Fig. 1(c). Both profiles are identical and clearly show two minima corresponding to the carbon-carbon distance (0.14 nm), proving that the individual carbon atoms in the hexagon network have been faithfully imaged.

Non hexagonal rings such as pentagons or heptagons can be regarded as topological defects within the carbon network. Especially a C-C bond rotation has been expected by a theory (known as the Stone-Wales transformation) and was supposed to lead to the pentagon-heptagon pair defect. **Fig. 2** shows a HR-TEM image of the penta-

AIST Central 5, Tsukuba 305-8565 Japan,

suenaga-kazu@aist.go.jp

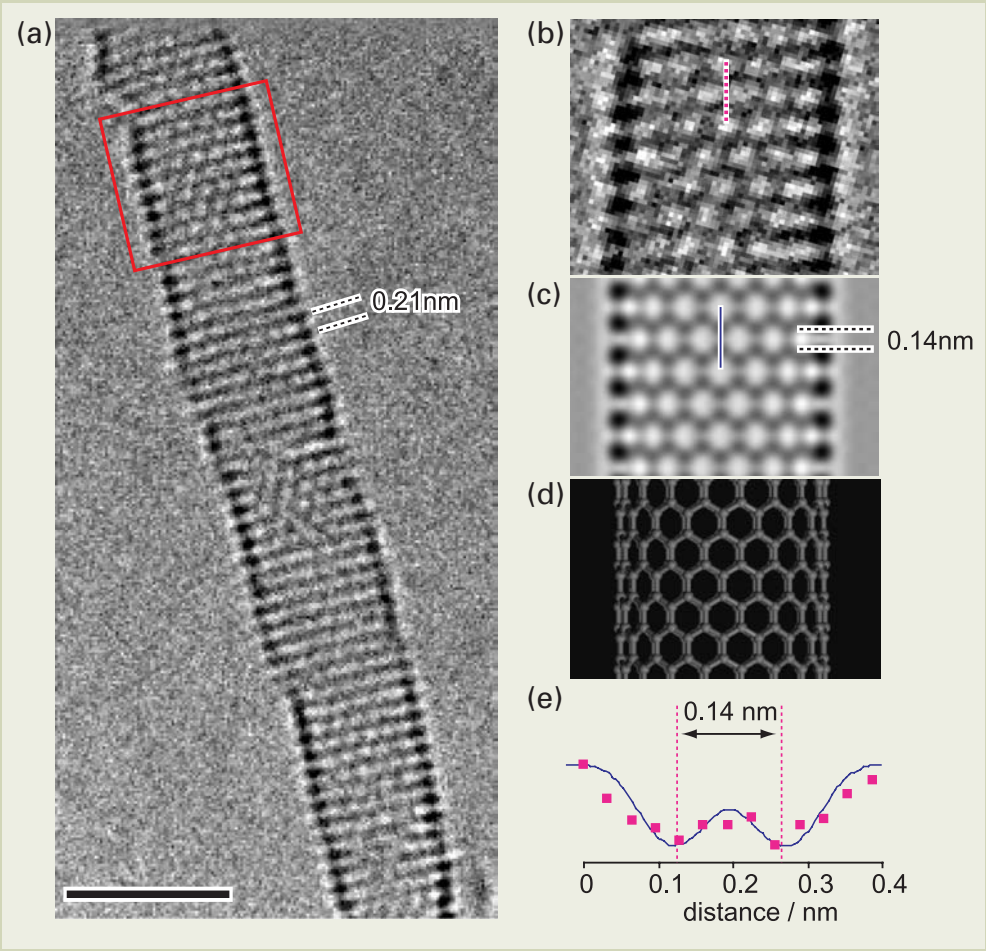


Fig. 1 (a) HR-TEM image of SWNT taken at 120 kV with a JEM-2010F equipped with a CEOS image corrector. The chiral index was assigned as (*18, 0*). (b) An enlarged image from the rectangle in (a). (c) Simulated image for (*18, 0*) SWNT and its atomic model (d). (e) Contrast profiles from indicated lines in (b) and (c), showing a typical C-C bond length (~ 0.14 nm) can be clearly resolved. Scale bar = 3 nm.

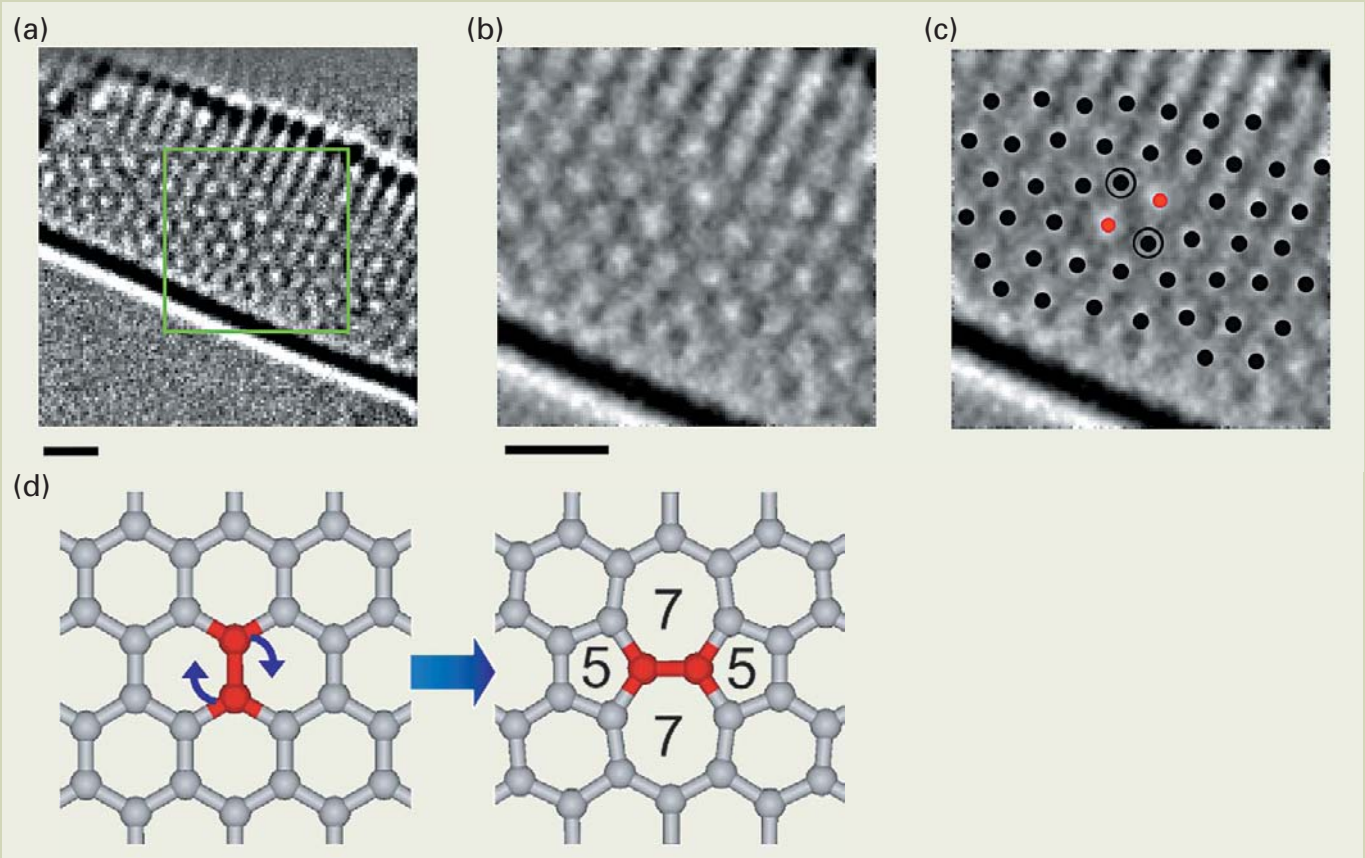


Fig. 2 (a)(b)(c) A pentagon-heptagon pair defect found on a SWNT after a heat treatment at 2000K. The defect is a proof of the Stone-Wales transformation due to the C-C bond rotation (d). Scale bar = 0.5 nm.

gon-heptagon pair defect of SWNT after a heat-treatment at 2000K [4]. An FFT analysis has been performed to eliminate one of the two layers overlapped for the SWNT. Plastic deformation of carbon nanotube indeed relies on the mobility of these topological defects. If any topological defect can migrate along the nanotube, this indeed means that the nanotube exhibits plasticity. The first experimental evidence for the active topological defects has been demonstrated by *in situ* HR-TEM [4]. **Fig. 3** shows a series of HR-TEM images of a SWNT after heat-treatment at 2000K. Here the hexagons are indicated by green whereas the pentagons and heptagons are indicated by blue and red, respectively. Although the structure on the other layer may have affected these HR-TEM images after the FFT analysis, these topological defects are indeed active and do migrate along the SWNT during the observation. This is the first atomistic proof that SWNT can exhibit an authentic plastic deformation which should rely on the active topological defects [5].

The other types of atomic defects rather than the topological defects have been also investigated seriously. *In situ* HR-TEM at elevated temperatures has shown the growth and migration of vacancies in carbon networks and given a rough estimation of the activation energy barrier for individual vacancies as ~2.2 eV [6]. Thermal relaxation of the Frenkel-type of defects (interstitial and vacancy pair) between the two layers of double wall carbon nanotubes has been also investigated *in situ* [7]. The critical temperature for the annihilation of the Frenkel defects was found around 450-500K which is very close to the annealing temperature for releasing the Wigner energy at 473 K. Therefore one can eventually conclude the Frenkel pair defects in graphite as the Wigner source which has been a well-known problem for half a century.

## Imaging single molecules

Another important usage of the HR-TEM with a moderate accelerating voltage is to visualize individual molecular structures. Organic molecules are known to suffer the irradiation damage due to the incident electrons and have been believed difficult to be imaged by HR-TEM. A common discussion about the difficulty in molecular imaging by HR-TEM often relies on the extremely small critical dose (typically several hundreds to thousands of electrons per $nm^2$ for protein specimens), with which any HR-TEM cannot attain an enough SN ratio to isolate the contrast of molecules. Such a discussion is valid for molecular crystal analysis because the critical dose is generally measured by the decrease of electron diffraction intensity. We should note that the major damage procedure in molecular crystal is attributed to the "cross-linking" of the adjacent molecules, which means that a broken bond due to the inelastic scattering will make a new bond to the adjacent molecules. Molecules in crystal will be heavily deformed due to the cross-link, which should lead to the decrease of diffraction intensities.

Damage process of isolated molecules should be completely different from that of molecular crystals. Even if the radical bonds are created due to inelastic scattering, there should be no adjacent molecules close to inter-link. The broken bonds can be instantly recovered unless any possibility to make other bonds. Consequently, no massive structural deformation could be observed on the isolated molecule except the knock-on displacements.

In order to observe the isolated molecules by HR-TEM, the SWNTs have been used as a specimen cell [8]. The inner surface of SWNTs is completely inert and is therefore very much suitable to hold the molecules inside because the broken bonds cannot easily make new bonds with the SWNT. By putting the damage-sensitive molecules inside the SWNTs, we have eventually succeeded to visualize the individual molecules in motion [9, 10, 11]. It is well-known that the *cis/trans* isomerization of the retinal chromophores triggers biological activity in rhodopsins. Also their conformation change is crucial for animal's vision. The isomerization and conformation changes of single

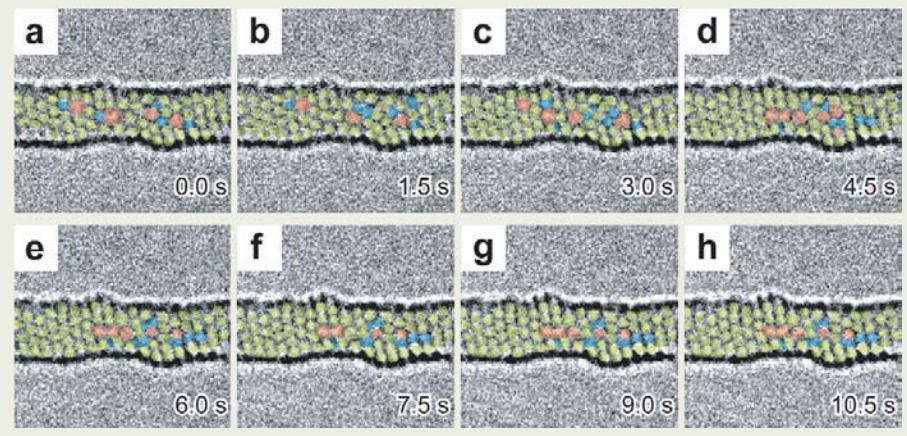


Fig. 3 A series of HR-TEM images showing the active topological defects. The hexagons are indicated by green whereas the pentagons and heptagons are indicated by blue and red. The regions are heavily deformed. Note that another layer has been eliminated by FFT analysis and may have some interference on the images.

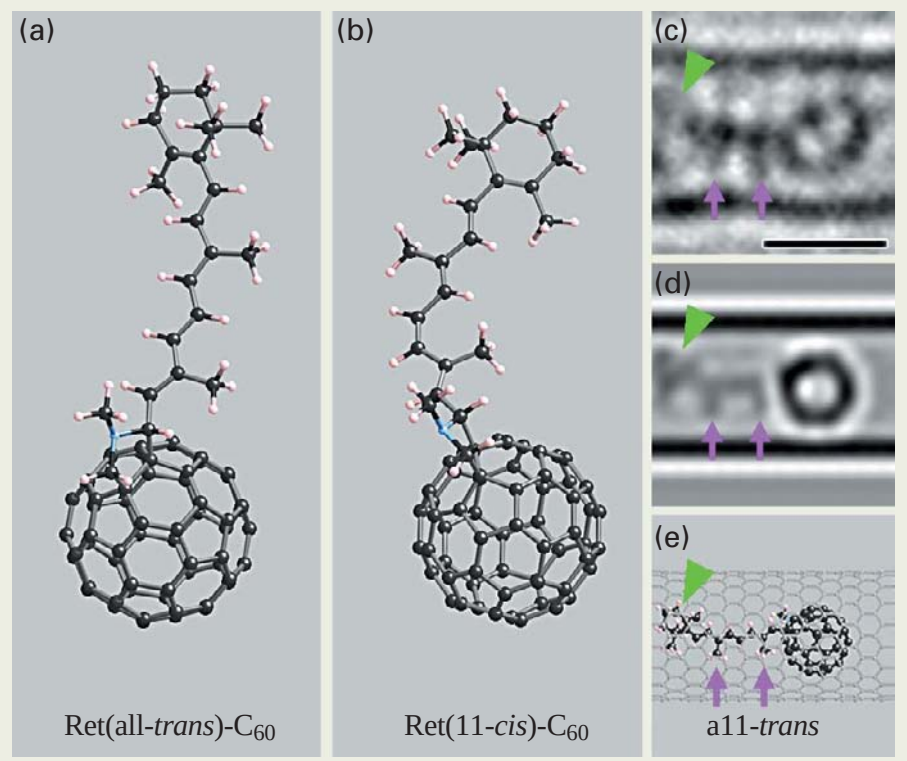


Fig. 4 Atomic models of the all-trans (a) and 11-*cis* (b) retinal chromophores attached to $C_{60}$ molecules. The carbon-carbon bonds around atom 11 are shown in red and the two methyl groups are highlighted in blue letters. In the *trans* form they point in the same direction, whereas in the *cis* form they do not. (c) An HR-TEM image of a Ret-$C_{60}$ molecule inside a SWNT, showing fine structures that correlate well with a simulation (d) and a best-fit model (e). General agreements of discontinuous contrast, corresponding to the methyl groups (red arrows) and cyclohexene (green arrow), can be found, suggesting that the image in (c) is of the all-*trans* isomer. Scale bar = 1 nm.

chains of carbon have been imaged for the first time [11]. **Fig. 4** shows an example for HR-TEM imaging of the $C_{60}$ fullerenes functionalized by retinal molecules. The retinal chromophores attached to the $C_{60}$ fullerenes are clearly visualized. The retinal chromophores consist of the conjugated carbon atomic chains (...-C=C-C=C-...) and have *cis/trans* isomers. The methyl groups as well as the cyclohexene are visible. Note that we need as much as 100,000 electrons/nm$^2$ in order to isolate the contrast of single retinal chromophores.

Isomer assignments of fullerene molecules have also been performed [12, 13]. A $C_{80}$ fullerene molecule consists of 80 carbon atoms, consequently 12 pentagons and 30 hexagons close the cage. Here we have chosen the $C_{80}$ molecule with the $D_{5d}$ symmetry among seven isomers. The $D_{5d}$-$C_{80}$ molecules were encapsulated in SWNTs and observed by HR-TEM. **Fig. 5** shows a series of HR-TEM images in which a $C_{80}$ molecule shows a rotational and translational movement inside the SWNT. At $t$ = 0 sec, a pair of pentagons are overlapped in projection (colored in orange). In the next frame at $t$ = 45 sec, the molecule shows the four bright spots corresponding to the pyrene-like tetracyclic components on the both sides (colored in orange), therefore one of the five mirror planes of the $D_{5d}$ symmetry is projected. In the last frame at $t$ = 79 sec, a pair of two dark lines appear and are attributed to the zig-zag chains of the anthracene-like tricyclic component (colored in orange). The individual molecules can be monitored as such during the rotational movements in SWNTs, so that the orientation changes can be investigated at

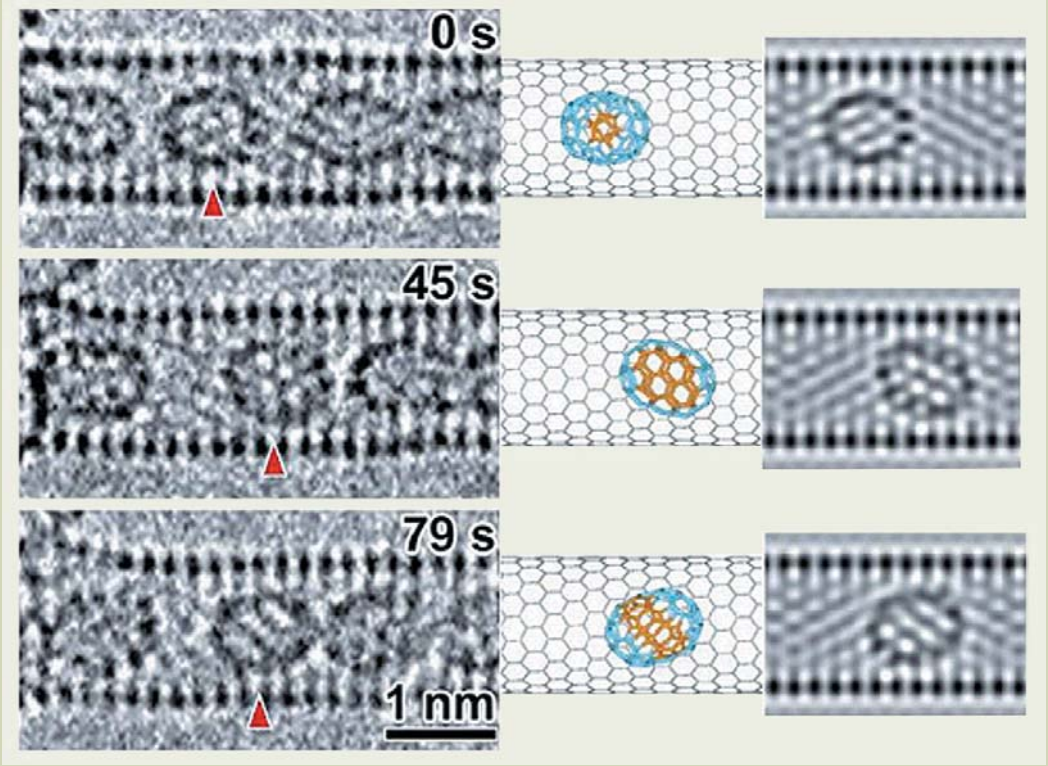


Fig. 5 A series of HR-TEM images of a same $C_{80}$ ($D_{5d}$) molecule (indicated by red arrows).

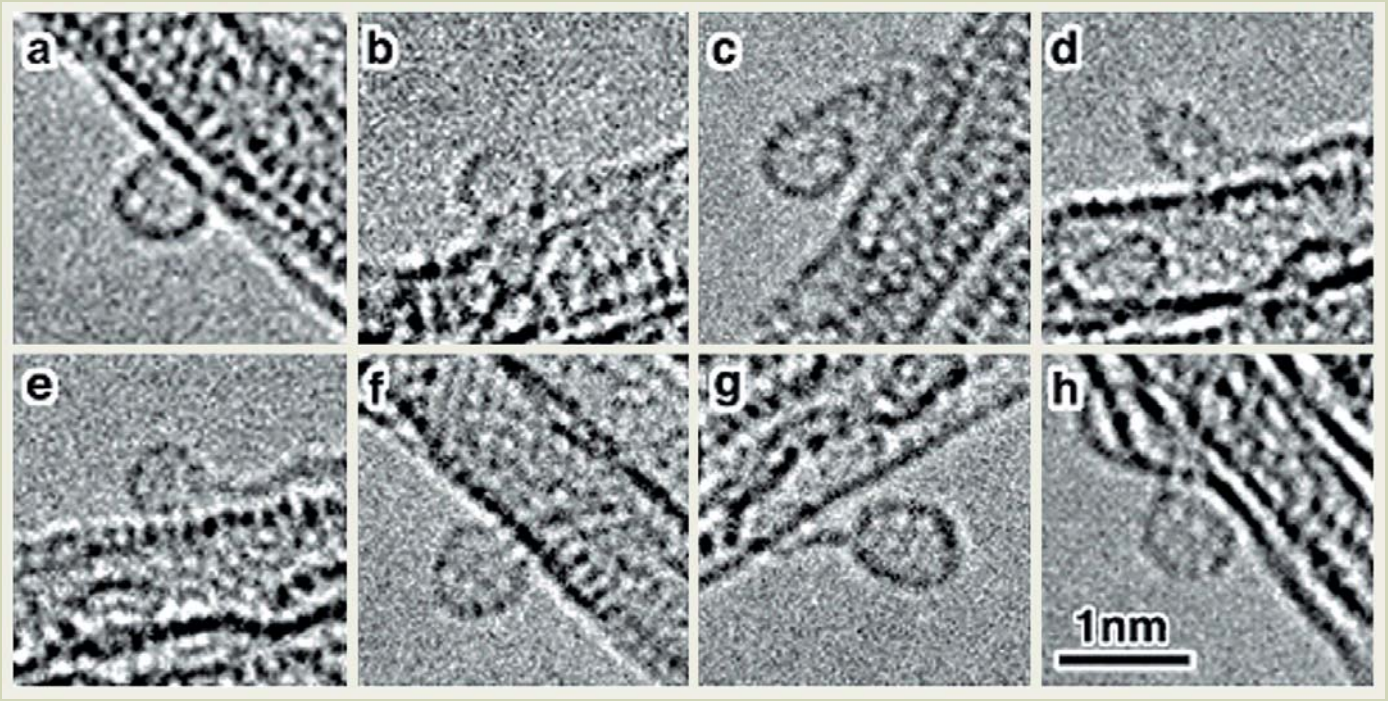


Fig. 6 (a)-(h) HR-TEM images of fullerene molecules. $C_{60}$-$C_3NH_7$ derivatives are attached to the surface of SWNTs. The intra-molecular structures are clearly visible for each fullerene. Some of them suffer a considerable deformation and deviate from the spherical shape ((d) and (g) for example).

each frame. In such a case, structural analysis and isomer identification are more reliably possible for the specific molecule. See the ref. [12] for detailed analysis.

One of the disadvantages for the use of SWNT as a specimen cell is that the HR-TEM contrast of SWNT walls often disturbs the molecular images and makes it difficult to analyze an individual molecular structure. In such a case one could try to fix the molecules outside the SWNTs so that the contrast of SWNT does not interfere with the molecular images. **Fig. 6** shows the HR-TEM of $C_{60}$ fullerene molecules outside the SWNTs. Each molecule has been fixed to the SWNTs by using a functional group of pyrrolidine ($C_{60}$-$C_3NH_7$) as an anchor and does exhibit some intramolecular features. To corroborate the observed HR-TEM images, the image simulations for the $C_{60}$ fullerene molecules were systematically made in more than 30 different orientations considering the $I_h$ symmetry (only 16 types are shown in **Fig. 7**). Comparing the HR-TEM images with the image simulations, the molecular orientation can be reasonably assigned for some of the experimental images. The molecule in Fig. 6(a) shows a six-membered ring contrast inside which is quite close to the simulated image of Fig. 7(I) corresponding to the $C_{60}$ molecule aligned parallel to the six-fold symmetry axis. Similarly the image in Fig. 6(b) corresponds to the simulation in Fig. 7(II), in which two pentagons are overlapped in projection and thus give rise to a small circle contrast in the middle of the $C_{60}$ fullerene. The image in Fig.6(c) is closely equivalent to the simulated image in Fig. 7(III). It is interesting to note that the molecule observed in Fig. 6(d) shows roughly ten dark spots around the fullerene cage and therefore may correspond again to the simulation in Fig. 7(II) although this molecule exhibits a large deformation. The image in Fig. 6(e) again corresponds to the Fig. 7(I) in spite of a slight misorientation. Besides all the above, we were unable to convincingly identify the other three molecules in Fig. 6(f, g, h) for any orientation in simulated images. It strongly suggests that the observed molecules could have suffered a considerable deformation [13].

## *In situ* observation of nano-carbon growth

One of the central topics in the nano-carbon research field has been the growth mechanism of the carbon nanostructures. Most important question is how the extra carbon atoms can be incorporated into the carbon networks during the growth. Do they need an open edge with the dangling bonds to accommodate the carbon atoms? How can the catalytic particles help the carbon atoms to be incorporated into the carbon network? We have started a systematic study by using an *in situ* HR-TEM to answer these fundamental questions.

Jin et al. reported a non-catalytic growth of carbon nanotube [14]. In this report a growing carbon nanotube with the "closed cap" has been directly observed for the first time at high temperatures inside HR-TEM. An asymmetric cap of the growing nanotube (attributed to the accumulated pentagons) has been identified as the growing sites, where the carbon dimers from the vapor can be incorporated into the carbon networks. It has been therefore proved that any open edge with the carbon dangling bonds is not necessary for the nanotubes to grow.

In the case of fullerene growth, we have introduced the tungsten (W) particles as a catalyst to promote its enlargement [15]. **Fig. 8** shows a series of HR-TEM images for the W catalyzed enlargement of fullerenes. A W cluster (marked as white arrowhead) suddenly jumped onto a large fullerene (~0.9 nm in diameter, roughly $C_{84\pm4}$ as shown in Fig. 8 (a). Upon the adsorption of this W cluster, the fullerene immediately started to grow as shown in Fig. 8(b)-(e). The W cluster was found to migrate continuously on the fullerene cage, and induced some local distortions on the cage. The fullerene cage grew radially (inflation in its diameter), instead of being elongated, confirming that the fullerene energetically prefers to keep a round shape. Formation and annihilation of sharp edges on the fullerene cage were also frequently observed during the growth. After the W cluster detached, the fullerene did not grow any more as shown in Fig. 8(f). The final diameter of the fullerene reached ~ 1.1 nm, which can be roughly assigned as $C_{136\pm8}$, corresponding to an average growth speed

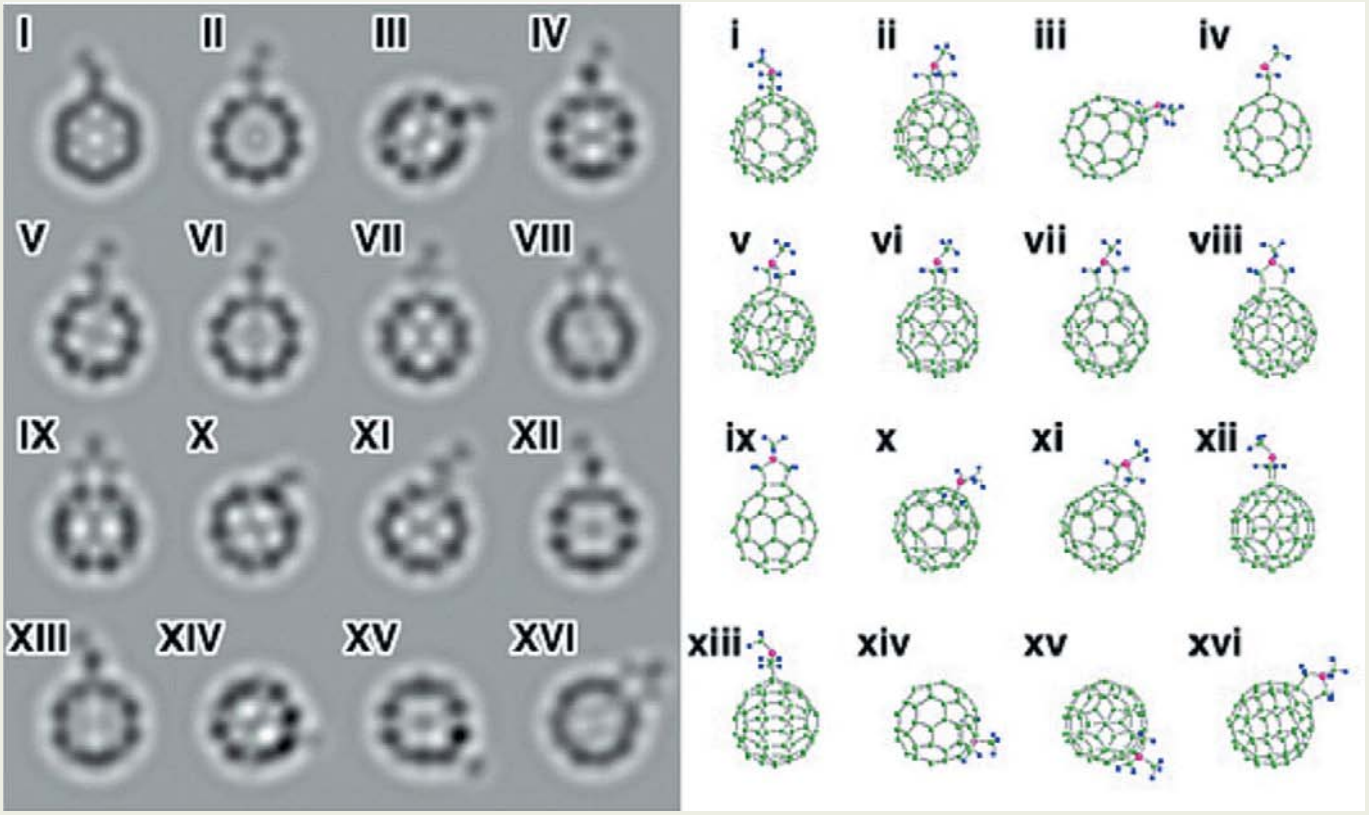


Fig. 7 Image simulations of $C_{60}$ fullerene derivatives for various orientations (left) to be compared with the Fig. 6. Corresponding atomic models are also shown (right). The pyrrolidine type functional groups are attached arbitrarily in the image simulations. The simulated image for the molecule oriented to the six-fold axis (I) fits quite well with the observed images of Fig. 6(a) for example.

of about 0.5 atom/sec.

From the experiments shown above we can reasonably derive that a major growth mechanism of fullerene or nanotube should be the carbon atoms incorporation into the adjacent pentagon sites and the re-arrangement of carbon networks afterwards possibly due to the Stone-Wales transformations. However this, the open edges with the carbon dangling bonds have been also identified for the nanotube and graphene layers during or after the high-temperature heat treatments [16, 17].

## Conclusion

We have shown here how a Cs-corrected HR-TEM at a moderate accelerating voltage (120 kV) can be applied to visualize the carbon nanostructures. In order to isolate the single atom contrast of a light element (Z = 6 for carbon) from the noise level, a relatively large number of electrons are required. We estimate that ~ 100,000 electrons/nm$^2$ are required to achieve a confidence level of 80% for the single carbon atom detection with the spatial resolution of ~ 0.14 nm. It is easy to see the carbon atoms if they were completely immobile during the observation because we can simply increase the exposure time to achieve a higher SN ratio and a higher spatial resolution. In most cases the carbon atoms and molecules are constantly moving during the observations due to the impact of the incident electron beam and therefore HR-TEM imaging of these atoms and molecules requires the minimum electron doses. Employing higher accelerating voltage is completely disadvantageous for the faster HR-TEM imaging of light elements because it should merely increase the knock-on probabilities. Both of Low-voltage TEM with a sophisticated electron optics and a high efficiency detector are required for the further *in situ* observations of moving atoms (e.g., chemical reactions).

## Acknowledgments

The research presented here has been supported by JST-CREST, NEDO, JST-ERATO and Grant-in-aid from the Ministry of Education, Culture, Sports, Science and Technology (MEXT) of Japan.

## References

[1] J. M. Zuo, I. Vartanyants, M. Gao, R. Zhang, and L.A. Nagahara, *Science* **300**, 1419-1421 (2003)
[2] R. R. Meyer et al., *J. Microsc.* **212**, 152-157 (2003)
[3] A. Hashimoto, K. Suenaga, A. Gloter, K. Urita and S. Iijima, *Nature* **430**, 870-873 (2004)
[4] K. Suenaga, H. Wakabayashi, M. Koshino, Y. Sato, K. Urita and S. Iijima, *Nature Nanotech*. **2**, 358-360 (2007).
[5] C. Jin, K. Suenaga and S. Iijima, *Nature Nanotech*. **3** (2008) 17-21.
[6] C. Jin, K. Suenaga and S. Iijima, *Nano Letters*, **8** (2008) 1127-1130.
[7] K. Urita, K. Suenaga, T. Sugai, H. Shinohara and S. Iijima., *Phys. Rev. Lett.* **94** (2005) 155502.
[8] K. Suenaga et al., *Science* **290** (2000) 2280-2282.
[9] Z. Liu, M. Koshino, K. Suenaga, A. Mrzel, H. Kataura and S. Iijima, *Phys. Rev. Lett*. **96** (2006) 088304.
[10] M. Koshino, T. Tanaka, N. Solin, K. Suenaga, H. Isobe and E. Nakamura, *Science* **316** (2007) 853.
[11] Z. Liu, K. Yanagi, K. Suenaga, H. Kataura and S. Iijima, *Nature Nanotech*. **2** (2007) 422-425.
[12] Y. Sato, K. Suenaga, S. Okubo, T. Okazaki and S. Iijima, *Nano Letters*, **7** (2007) 3704-3708.
[13] Z. Liu, K. Suenaga and S. Iijima, *J. Am. Chem. Soc.*, **129** (2007) 6666-6667.
[14] C. Jin, K. Suenaga and S. Iijima, *ACS Nano*, **2** (2008) 1275-1279.
[15] C. Jin, H. Lan, K. Suenaga, L.-M. Peng and S. Iijima, *Phys. Rev. Lett*. **101** (2008) 176102
[16] C. Jin, K. Suenaga and S. Iijima, *Nano Research*, **1** (2008) 434-439.
[17] Z. Liu, K. Suenaga, P.J.F. Harris and S. Iijima, *Phys. Rev. Lett.*, **102** (2009) 015501

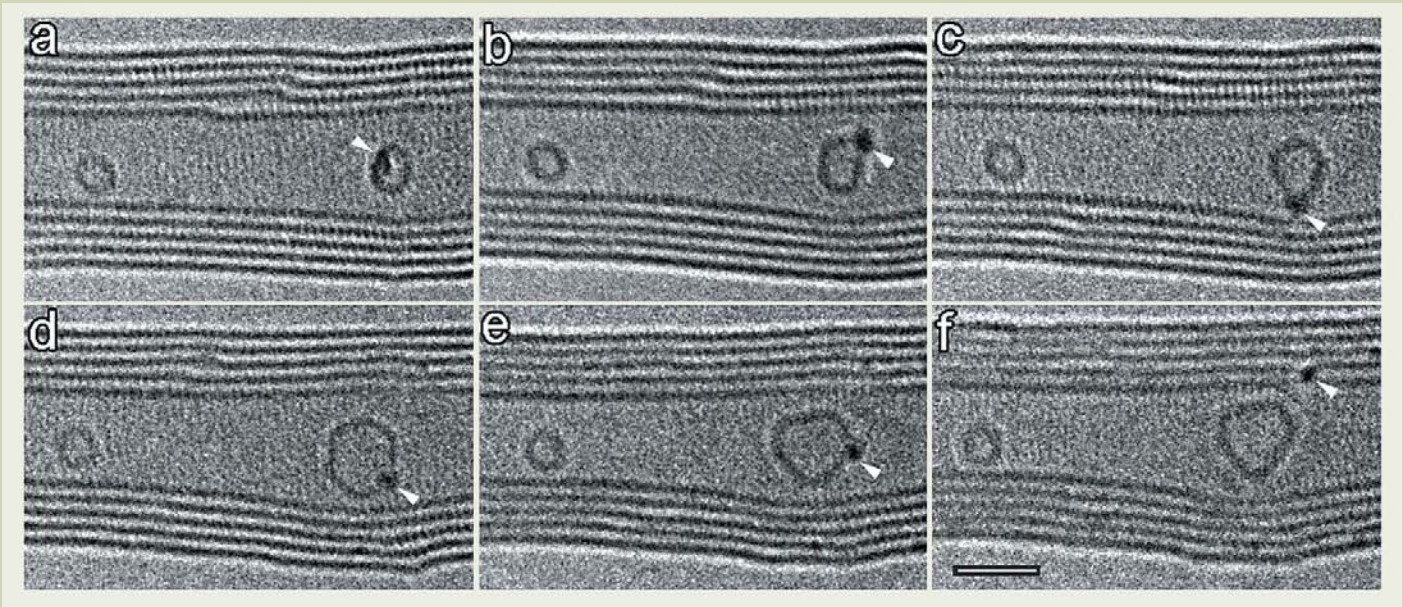


Fig. 8 *In situ* HR-TEM images of the fullerene growth at high temperatures. The W clusters act as catalyst (indicated by arrows) [15]. Scale bar = 2 nm.

# Studies on Natural Antioxidant Derivatives: Enhanced Radical-Scavenging and Reduced Prooxidant Activities

**Kiyoshi Fukuhara**

**Division of Organic Chemistry, National Institute of Health Sciences**

## Introduction

Flavonoids are plant phenolic compounds that are widely distributed in foods and beverages [1]. They have been extensively studied with regard to their antioxidative and cytoprotective properties in various biological models [2-5]. They can protect against oxidative stress by scavenging reactive oxygen intermediates [6-8] and also by chelating iron [9]. Since oxidative damage to biomolecules, such as DNA and carbohydrate, proteins or polyunsaturated fatty acids is thought to play a significant role in mutagenesis, cancer, aging, and other human pathologies, considerable attention has been focused on the development of antioxidants to prevent or to treat diseases associated with oxidative stress [3, 10]. However, there is also some evidence that flavonoids themselves are mutagenic [11-14] and carcinogenic [15, 16] in both bacterial and mammalian experimental systems. The process that damages DNA, and is thus responsible for DNA alterations and genotoxicity, could be accelerated by the effects of metal ions, as naturally occurring metal constituents of the nucleus. Indeed, while quercetin is known to be a powerful antioxidant that scavenges free radicals associated with lipid peroxidation, the dietary administration of excessive quercetin has been reported to induce renal tubule adenomas and adenocarcinomas in male rats [15], as well as intestinal and bladder cancer in rats [16]. There is also considerable evidence that quercetin induces extensive DNA damage and forms 8-oxodG by reacting with Cu(II) [17]. Therefore, in order to develop an antioxidant for clinical use, a compound having a strong antioxidative activity but with a weak prooxidant effect has been desired.

Kamiyoga 1-18-1, Setagaya, Tokyo 158-8501, Japan

e-mail: fukuhara@nihs.go.jp

## Planar Catechin Analogue

Quercetin protects against oxidant injury and cell death [18] by scavenging free radicals [19, 20], thereby preventing lipid peroxidation [21] and terminating chain-radical reactions [22]. However, in the case of (+)-catechin (Cat), there have only been a few reports on this use for the treatment of free radical-associated disease, even though the mechanism of oxygen radical scavenging has been well studied [23, 24]. The superior antioxidant ability of quercetin results from the formation of a stable radical, due to the C2-C3 double bond and the resulting planar geometry which delocalizes the radical throughout the entire molecule [25]. Since the B ring in Cat is known to be perpendicular to the A ring [26], the radical-scavenging ability of Cat might be improved by constraining the geometry of Cat to be planar. Therefore, planar catechin analogue (PC1) with respect to the chroman and catechol moieties of Cat was synthesized via oxo-Pictet-Spengler reaction, by taking advantage of the formation of a bridge between the 3-OH group on ring C and C6' on ring B as shown in **Figure 1** [27]. Typically, Cat and 1.2 equivalents of acetone in THF were treated with 1.2 equivalents of trimethylsilyl trifluoromethane sulfonate at -5°C to form the PC1 in 3 hours. The planarity of PC1 was confirmed by single-crystal X-ray crystallography. X-ray analysis also showed that the stereochemistry of 3-H on ring C was maintained throughout the reaction without any acid-catalyzed racemization. Although the PC1 synthesized by the reaction has two methyl groups as side chains, it is possible to synthesize planar catechin analogues so that the lipophilicity is controlled by varying the length of the alkyl side chains in place of methyl groups, by using ketones with alkyl side chains in this reaction.

### Antioxidative properties

The radical-scavenging activities of Cat and PC1 as well as that of quercetin were compared using the galvinoxyl radical ($G^{\bullet}$) as an oxyl radical species (**Figure 2**) [27]. Upon addition of Cat to a deaerated acetonitrile (MeCN) solution of $G^{\bullet}$, the absorption band at 428 nm due to $G^{\bullet}$ disappeared immediately. This indicated that hydrogen abstraction from one of the OH groups on the B ring of Cat by $G^{\bullet}$ had taken place to give the (+)-catechin radical and hydrogenated $G^{\bullet}$ (GH). The decay of the absorbance at 428 nm due to $G^{\bullet}$ obeyed pseudo-first-order kinetics when the concentration of Cat was maintained at more than 10-fold excess of the $G^{\bullet}$ concentration. From the linear plot of the observed pseudo-first-order rate constant ($k_{obs}$) vs. the Cat concentration,

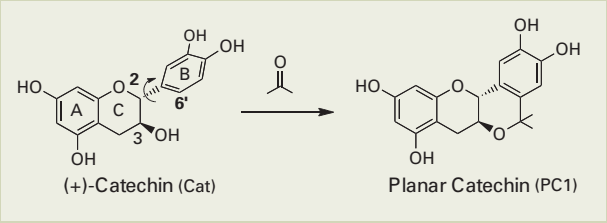


Fig. 1 Synthesis of planar catechin (PC1).

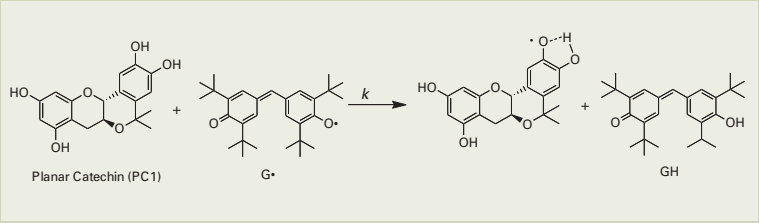


Fig. 2 Radical scavenging reaction of PC1 with galvinoxyl radical (G•).

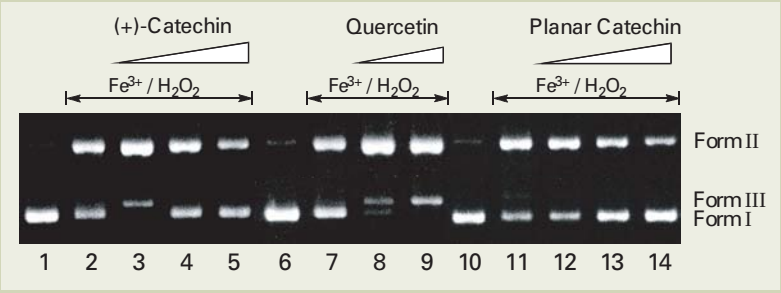


Fig. 3 Effects of (+)-catechin, quercetin and PC1 on DNA breakage induced by $Fe^{3+}/H_2O_2$. Assays were performed in 50 mM sodium cacodylate buffer, pH 7.2, containing 45 µM of pBR322DNA, for 1h at 37°C. Lanes 1, 6, and 10; DNA alone, lanes 2, 7, and 11; 10 mM $H_2O_2$ and 10 µM $FeCl_3$, lanes 3–5, 8 and 9, and 12–14; 10 mM $H_2O_2$ and 10 µM $FeCl_3$ in the presence of 0.25, 1.25, and 2.5 mM (+)-catechin (lanes 3–5), 0.25 and 1.25 mM quercetin (lanes 8 and 9), and 0.25, 1.25 and 2.5 mM PC1 (lanes 12–14).

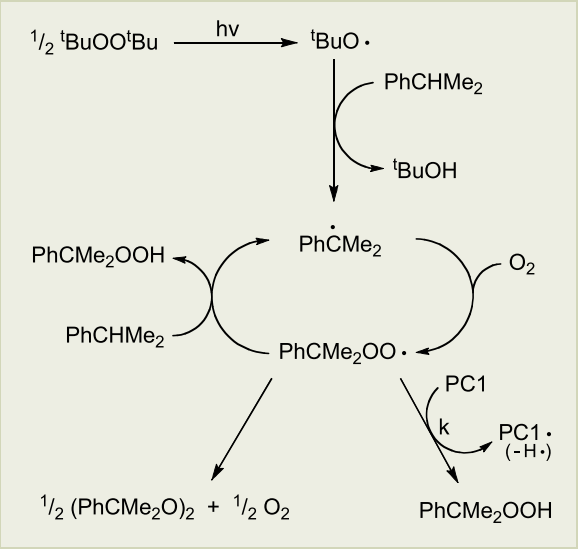


Fig. 4 Formation of cumylperoxyl radical from photoirradiation of $^t$BuOO$^t$Bu and its reaction with PC1.

we determined that the second-order rate constant ($k$) for hydrogen abstraction of CA by G• was $2.34 \times 10^2$ $M^{-1}$ $s^{-1}$. The $k$ values for PC1 and quercetin were determined in the same manner to be $1.12 \times 10^3$ $M^{-1}$ $s^{-1}$ and $1.08 \times 103$ $M^{-1}$ $s^{-1}$, respectively. Thus, the k values for PC1 and quercetin are about 5-fold larger than that for Cat. These results suggest that molecular planarity is essential for the radical-scavenging ability of antioxidants.

The hydroxyl radical is the most reactive oxygen-derived free radical and is responsible for aging and free radical-mediated injury. Therefore, the effects of Cat, PC1, and quercetin on hydroxyl radical-mediated DNA breakage were investigated. DNA-strand scission in supercoiled pBR322DNA was induced by a hydroxyl radical-generating system using hydrogen peroxide in the presence of $Fe^{3+}$ (Fenton reaction). As shown in **Figure 3**, Cat at a high concentration (1.25 and 2.5 mM) suppressed DNA strand breakage, while at a low concentration (0.25 mM) it exhibited pro-oxidant properties, consistent with enhanced DNA cleavage in comparison to cleavage without antioxidant. Quercetin only showed pro-oxidant effects at 0.25 and 1.25 mM. The measured pro-oxidant effects of Cat and quercetin may be attributed to autoxidation of the antioxidant in the presence of transition metal, leading to the generation of primary radicals such as the hydroxyl radical. In contrast to the pro-oxidant effects of Cat and quercetin, the addition of PC1 protected DNA from Fenton reaction-mediated damage at all concentrations tested. PC1 exhibited marked hydroxyl radical-scavenging ability, which exceeded that of Cat. Since PC1 is very lipophilic compared to Cat (data not shown), the high radical-scavenging ability of PC1 might be very useful for suppressing free-radical associated events, especially in the cell membrane.

## Radical scavenging mechanism

Considering the radical scavenging mechanism of phenolic compounds, there are two possibilities in the mechanism of hydrogen transfer reactions: either a one-step hydrogen atom transfer or an electron transfer followed by proton transfer. We have recently reported that the hydrogen transfer from Cat to G• or cumylperoxyl radical proceeds via electron transfer from Cat to G• or cumylperoxyl radical [28]. This transfer is accelerated in the presence of metal ions such as $Mg^{2+}$ or $Sc^{3+}$, followed by proton transfer. In such cases, the coordination of the metal ion to the one-electron reduced species of G• or cumylperoxyl radical may stabilize the product, resulting in acceleration of the electron transfer process. On the other hand, the hydrogen transfer reaction of vitamin E proceeds via a one-step hydrogen atom transfer process, in this case there is no effect of metal ions on the hydrogen transfer rate from vitamin E analogues to the G• [29-31]. Therefore, the effect of a metal ion on the rate of hydrogen transfer from PC1 to cumylperoxyl radical can distinguish between one-step hydrogen atom transfer and electron transfer mechanisms in the radical scavenging reaction of PC1.

The kinetics of hydrogen transfer from Cat and PC1 to cumylperoxyl radical has been examined in propionitrile (EtCN) at low temperature (203K) by use of ESR [32]. The photoirradiation of an oxygen-saturated EtCN solution containing di-*t*-butylperoxide ($^t$BuOO$^t$Bu) and cumene with a 1000 W high-pressure mercury lamp results in formation of cumylperoxyl radical ($PhCMe_2OO$•), which was readily detected by a JEOL X-band spectrometer (JES-ME-1X). The cumylperoxyl radical is formed via a radical chain process shown in **Figure 4**. The photoirradiation of $^t$BuOO$^t$Bu results in the homolytic cleavage of the O–O bond to produce $^t$BuO•, which abstracts a hydrogen from cumene to give cumyl radical, followed by the facile addition of oxygen to cumyl radical. The cumylperoxyl radical can also abstract a hydrogen atom from cumene in the propagation step to yield cumene hydroperoxide, accompanied by regeneration of cumyl radical. When the light is cut off, the ESR signal intensity decays obeying second-order kinetics due to the bimolecular reaction. In the presence of PC1, however, the decay rate of cumylperoxyl radical after cutting off the light becomes much faster than that in the absence of PC1. The decay rate in the presence of PC1 ($1.0 \times 10^{-4}$ M) obeys pseudo-first-order kinetics. This decay process is ascribed to hydrogen transfer from PC1 to cumylperoxyl radical (Figure 4). From the slope of the linear plot of $k_{obs}$ vs concentration of PC1 is determined the second-order rate constant ($k$) for the hydrogen transfer from PC1 to cumylperoxyl radical as $9.7 \times 10^2$ $M^{-1}$ $s^{-1}$ in EtCN at 203K. The $k$ value for Cat was also determined in the same

manner as $6.0 \times 10^2$ $M^{-1}$ $s^{-1}$, showing that the hydrogen transfer rate from PC1 to cumylperoxyl radical is significantly faster than that from Cat. By using this system, the effect of a metal ion on the *k* value of PC1 was examined. As in the case of Cat, the hydrogen transfer from PC1 to cumylperoxyl radical was significantly accelerated by the presence of $Sc(OSO_2CF_3)_3$ as shown in **Figure 5**. Thus, the hydrogen transfer from PC1 to cumylperoxyl radical also proceed via electron transfer from PC1 to cumylperoxyl radical followed by proton transfer from $PC1^{\bullet+}$ to one-electron reduced species cumylperoxyl radical as shown in **Figure 6**.

## One-electron oxidation potential

The larger *k* value of PC1 as compared to that of Cat may be ascribed to the stability of the radical cation of PC1 ($PC1^{\bullet+}$), which is produced in the electron transfer from PC1 to cumylperoxyl radical. The electron-donating *i*-propyl group at the B ring of PC1 may significantly stabilize $PC1^{\bullet+}$, resulting in the acceleration of the electron-transfer step. In such a case, the oxidation potential of PC1 is expected to be more negative than that of Cat. To determine the oxidation potential of PC1, the cyclic voltammogram of PC1 was recorded in MeCN containing 0.1 M TBAP as a supporting electrolyte at 298K. Two irreversible oxidation (anodic) peaks were observed at 1.22 V and 1.41 V vs SCE. A similar cyclic voltammogram was obtained for Cat, which exhibits irreversible oxidation peaks at 1.16 V and 1.35 V vs SCE. This indicates that the radical cation of Cat is too unstable at the time scale of CV measurements. The second-harmonic alternating current voltammetry (SHACV) method is known to provide a superior approach to directly evaluating one-electron redox potentials in the presence of follow-up chemical reaction, relative to the better-known DC and fundamental harmonic AC method, the SHACV method is applied to determine the oxidation potentials ($E^0_{ox}$) of PC1 and Cat in MeCN containing 0.1 M TBAP at 298K [40]. The $E^0_{ox}$ value of PC1 thus determined (1.01 V vs SCE) is significantly more negative than that of Cat (1.18 V vs SCE) as expected above [32]. Thus, PC1 may undergo one-electron oxidation by cumylperoxyl radical more easily than Cat, showing excellent radical-scavenging ability.

## Reduced prooxidant property

The antioxidant effects of flavonoids undoubtedly contribute to their chemopreventive activities. However, the fact that flavonoids themselves have antibacterial and bactericidal activities, as well as being mutagenic and pro-/co-carcinogenic, should be considered when contemplating their clinical use. Their harmful effects are thought to be due to their prooxidant activities. In the presence of Cu(II), Cat induces oxidative DNA damage and fatty acid peroxidation, due to production of reactive oxygen species via electron transfer from Cat to molecular oxygen mediated by Cu(II). However, this prooxidant effect is also observed for the dianion of Cat produced by the reaction between Cat and 2 equiv. of tetramethylammonium methoxide [33, 34]. The one electron-transfer reaction from dianion to molecular oxygen proceeds to form $O_2^{\bullet-}$. The same reaction is also shown by the dianion ($PC1^{2-}$) of PC1, forming $O_2^{\bullet-}$ by electron-transfer oxidation from $PC1^{2-}$ to $O_2$ as confirmed by a JEOL X-band spectrometer (JES-FA100) [35]. A characteristic ESR $g_{//}$ value of 2.070 due to $O_2^{\bullet-}$, together with an ESR $g_{//}$ value of 2.050 for protonated $O_2^{\bullet-}$ ($HO_2^{\bullet}$) was observed for an $O_2$-saturated MeCN solution of PC1 and 2 equiv of methoxide ($MeO^-$) at 77K, as shown in **Figure 7**b. During $O_2^{\bullet-}$ generation, the resultant radical anion from PC1 underwent an intramolecular proton transfer to give an *o*-semiquinone radical anion form ($PC1^{\bullet-}$), with a characteristic ESR g value of 2.0048 at 298K, as shown in Figure 7a.

If one molecule of $PC1^{2-}$ reacts with one molecule of $O_2$, the rate of electron transfer from $PC1^{2-}$ to molecular oxygen should show first-order dependence. In fact, the increase in absorbance at 485 nm due to the radical anion of PC1 obeyed pseudo-first-order kinetics under conditions where the $O_2$ concentration was maintained at more than 10-fold excess relative to the $PC1^{2-}$ concentration. The $k_{obs}$ increases linearly with increases in $O_2$ concentration. The slope of

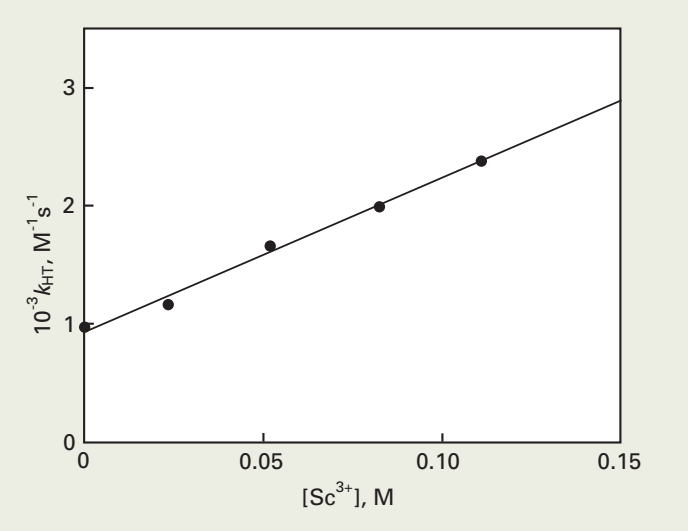


Fig. 5 Plot of k vs [$Sc^{3+}$] in the reaction of PC1 to cumylperoxyl radical in the presence of $Sc(OSO_2CF_3)_3$ in EtCN at 203K.

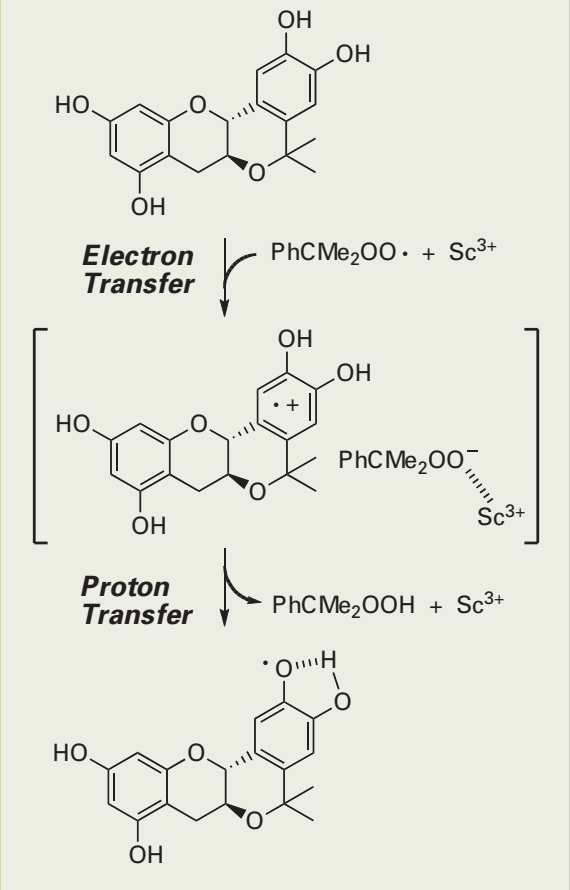


Fig. 6 $Sc^{3+}$-accelerated $G^{\bullet-}$-scavenging reaction by PC1 via an electron transfer.

the linear plot of $k_{obs}$ vs. [$O_2$] gave the second-order rate constant of the electron transfer ($k_{et}$) from $PC1^{2-}$ to $O_2$: $2.8 \times 10^{-2}$ $M^{-1}s^{-1}$. This $k_{et}$ value is about half of that determined for Cat ($5.8 \times 10^{-2}$ $M^{-1}s^{-1}$), indicating that electron transfer from $PC1^{2-}$ to $O_2$ proceeds slower than from Cat. While PC1 provides efficient protection against DNA strand breakage induced by Fenton reaction, the low $k_{et}$ value implies that, in physiologically relevant systems, the ability of PC1 to generate oxygen radicals responsible for its prooxidant activity might not be as high as that of Cat. Among natural antioxidants, α-tocopherol and ascorbic acid are typical compounds which are useful for the treatment or prevention of diseases associated with oxidative stress. However, administrating a large amount of such antioxidants is unfavorable because of their prooxidant properties, similarly to Cat or quercetin. Therefore, the use of PC1, rather than natural antioxidants such as Cat, quercetin, α-tocopherol, ascorbic acid, etc., might be favorable for the treatment of diseases associated with oxidative stress due to suppression of oxidant injury as a side-effect arising from the antioxidant itself.

## Biological properties

In addition to antioxidant ability, catechin is known to have several biological activities, including anti-allergic effects, inhibition of α-glucosidase, antibacterial, antivirus, and antitumor activities, though none of these activities are particularly strong. Therefore, the inhibitory effects of PC1 on α–glucosidase from *Saccharomyces cerevisiae* and *Bacillus stearothermophilus* were evaluated [36]. Surprisingly, in contrast to the relatively weak inhibitory effect of catechin with an $IC_{50}$ > 500 μM, PC1 exhibited strong inhibitory effects of the respective α–glycosidases with $IC_{50}$ = 1.2 μM (*S. cerevisiae*) and 0.7 μM (*B. stearothermophilus*). As α–glycosidase catalyzes the final step in the digestive process of carbohydrates, the strong inhibitory effect on α–glycosidase suggested that PC1 may be used as a lead compound for the development of antidiabetic therapeutics, similar to Acarbose and Voglibose which are known to reduce postprandial hyperglycemia primarily by interfering with carbohydrate digesting enzymes and delaying glucose absorption.

Potent antiviral activity of PC1 was also shown by significant inhibition of Newcastle Disease Virus infection of BHK cells [36]. Considering the strong inhibitory effect on α–glucosidase, the antiviral activity of PC1 may be attributed to inhibition of α- glucosidase during protein synthesis that is essential for virus proliferation [37].

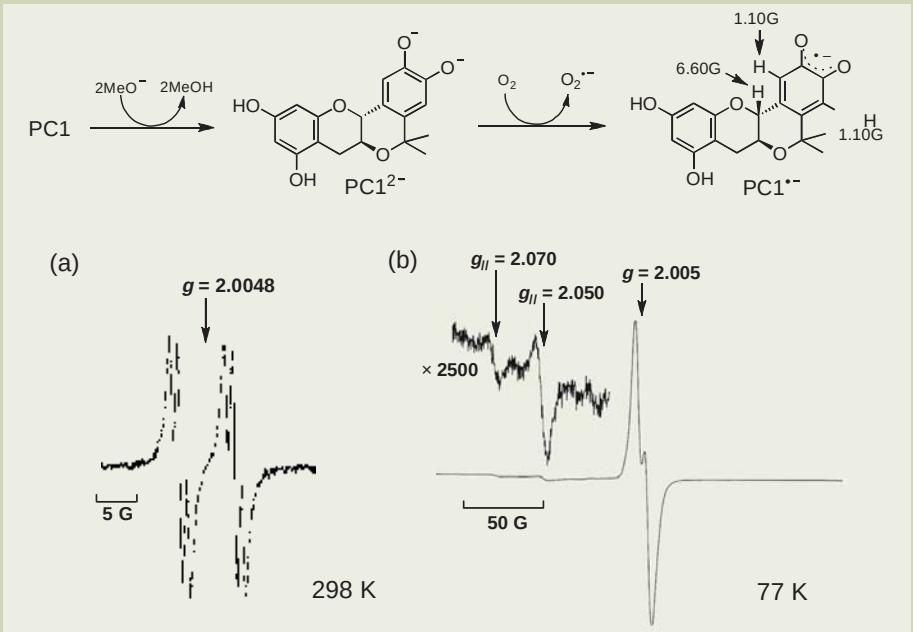


Fig. 7 ESR spectra of $PC1^{\bullet-}$ (a) and $O_2^{\bullet-}$ (b) generated in the reaction of $PC1^{2-}$ with $O_2$ in MeCN.

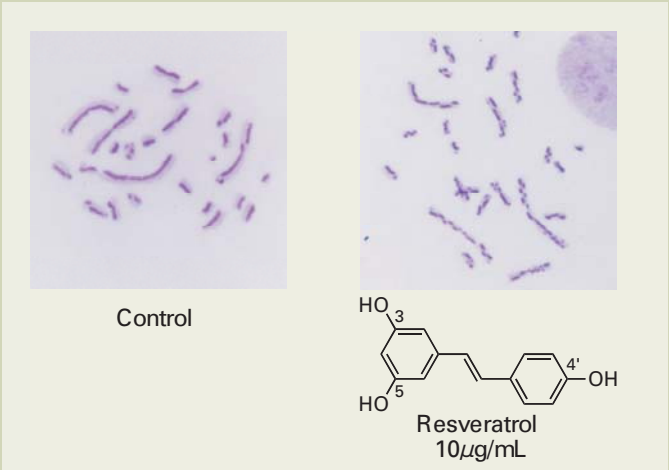


Fig. 8 Micrograph of representative sister-chromatid exchange (SCE) in SPD8 cells treated with 2.5 μg/ml of resveratrol for 48 h.

# Methyl Resveratrol

## Resveratrol

Resveratrol (3,4',5,4'-trihydroxy-*trans*-stilbene*trans*-3,4',5-trihydroxystilbene) is a natural phytoalexin present in grapes and wine, which that has been shown to play an essential role in the prevention of several human pathological processes including, such as inflammation [38], atherosclerosis [39] and carcinogenesis [40]. The cancer preventive activity of resveratrol is linked to its ability to eliminate free radicals and to reduce oxidative and mutagenic stress. It has been demonstrated that resveratrol suppresses lipid peroxidation by both scavenging of the free radicals and chelation of copper [41]. Among three hydroxyl groups in resveratrol, and 4'-hydroxyl group is essential for radical-scavenging activities [42-44]. Besides, 4'-hydroxyl group has been primarily responsible for copper binding property [45]. In addition to the meritoriousits beneficial effects, resveratrol is genotoxic, inducing a high frequency of chromosomal aberrations (CA), micronucleus, and sister chromatid exchanges (SCE) in vitro [46]. SCE is induced during DNA replication, and the formation is a result of homologous recombination. As shown in **Figure 8**, resveratrol is a potent inducer of SCE.

In this regard, we have shown that resveratrol is able to mediate Cu(II)-dependent DNA strand scission under neutral conditions [47]. It has also been shown that DNA cleavage is more likely caused by a copper-peroxide complex as the reactive species rather than by a freely diffusible oxygen species. However, the structural feature of resveratrol that is effective for DNA cleavage is still unknown. We have then designed to explore the substrate specificity of synthesized hydroxystilbene derivatives for Cu(II) and DNA binding [48]. To confirm the electrostatic interaction of hydroxylated stilbene with both Cu(II) and DNA, ESR signals of Cu(II) were observed in the presence of resveratrol or its analogues together with calf thymus DNA by using a JEOL X-band spectrometer (JES-FE 2XG). Once the ternary complex of Cu(II)-resveratrol-DNA, which is due to the efficient binding affinities of resveratrol with both Cu(II) and DNA, is formed, the complex may result due to its high DNA-cleaving ability. **Figure**

**9** shows that an ESR signal of Cu(II) became multiple upon the addition of DNA, consistent with the fact that Cu(II) complexes DNA. In fact, the decrease in the peak height of Cu(II) in a solution of calf thymus DNA is due to the intercalation of Cu(II) with a large molecule of DNA, which limits the mobility of Cu(II). When resveratrol was added to the solution of Cu(II)-DNA complex, the peak height of the ESR signal was reduced to one-half of that of the Cu(II)-DNA complex and the resonance was weakened, suggesting that resveratrol was bound to Cu(II)-DNA complex and thus induced the reduction of Cu(II), which was converted to an ESR-silent species, very likely Cu(I). If the binding of Cu(II) to DNA decreases with the addition of resveratrol, the signal of Cu(II) should increase to the height of unbound Cu(II). An increase in peak height was also not observed for other resveratrol analogues, suggesting that Cu(II) remains in a complex with DNA even after the addition of resveratrol and its analogues. Compared to the reduction of Cu(II) to Cu(I) by resveratrol, an efficient reduction of the peak height of Cu(II)-DNA complex was not observed with the addition of isoresveratrol (**d**). It is possible that the insufficient binding affinity of **d** with both DNA and Cu(II) may impair the highly efficient reduction of Cu(II) to Cu(I). Similarly, **e** affected the spectra of Cu(II)-DNA with efficient reducing and broadening, whereas there was no effect on the spectra of Cu(II)-DNA upon the addition of **f**, indicating that the reductive activation of Cu(II) is accelerated by electrostatic interaction of a hydroxyl group at the 4'-position .

## Methyl resveratrol

Structure-activity relationship studies of resveratrol analogues revealed that the 4'-hydroxyl group, besides being essential for antioxidative activity, is also responsible for the in vitro cytogenetic activity of resveratrol [45, 48]. In this regard, our challenge is to create novel resveratrol analogues that not only exert enhanced antioxidative abilities but also have reduced in vitro genotoxicity. Such analogues could lead to the development of new drugs against various diseases, particularly those related to oxidative stress. In our attempt to design new resveratrol analogues, we focused on the methyl groups of the tocopherol due to their proven antioxidative effects on the aromatic ring [29]. In particular, methyl groups at the ortho position to the hydroxyl group contributes to delocalization of the unpaired electron of the corresponding phenoxyl radical, which is generated in the reaction with radical species, due to hyperconjugation. In this study, we describe resveratrol analogues where methyl groups are introduced into the ortho position of 4'-hydroxyl group as shown in **Figure 10** [49]. Methyl groups were also introduced at the 4' position para to the 4'-hydroxyl group. These designed methyl derivatives (**11** and **12**) of resveratrol, 4-methylresveratrol (**13**) and its methyl derivatives (**14** and **15**) were synthesized by means of Wittig-Horner reactions between appropriate dibenzyloxybenzylphosphonic acid diethylesters (**1**, **2**) and benzyloxybenzaldhydes (**3**, **4**, **5**), followed by deprotection using $AlCl_3$ and *N*,*N*-dimethylaniline. Trans geometries of these compounds were confirmed by their coupling constants (16.0–16.4 Hz) for the olefinic proton.

## Effect on the antioxidative property

The radical scavenging activities of resveratrol and its analogues were evaluated by the hydrogen transfer reaction using G• as an oxyl radical species [49]. The hydrogen abstraction from resveratrols by G• in deaerated MeCN was monitored the decrease of absorbance at 428 nm due to G• that obeyed pseudo-first-

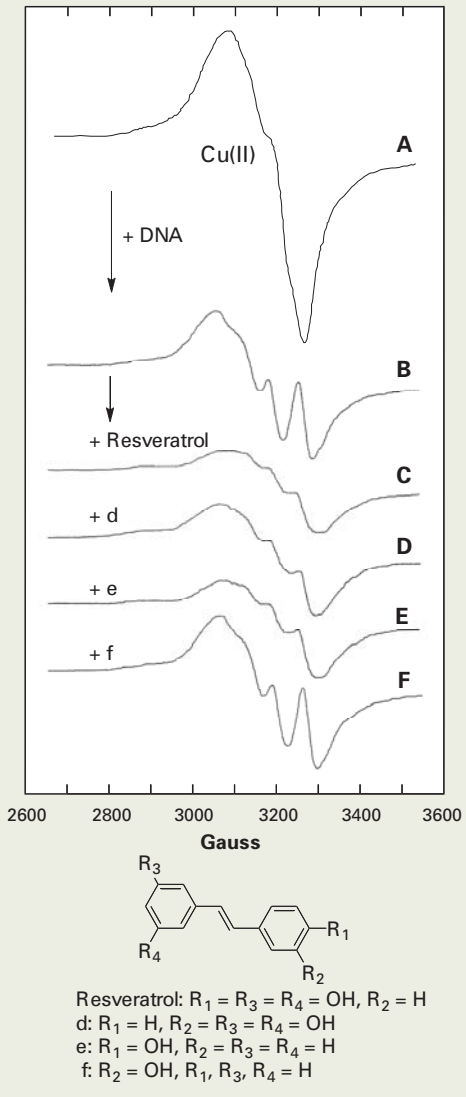


Fig. 9 Effect of resveratrol and its analogues on the ESR spectra of Cu(II) in the presence of calf thymus DNA. Spectra A is $CuCl_2$ and spectra B-F show after addition of 2 mM nucleotide phosphate of calf thymus DNA in the absence (B) or presence of 1 mM chemicals (C: resveratrol; D: **d**; E: **e**; F: **f** ). All spectra were recorded after incubation for 30 min at room temperature.

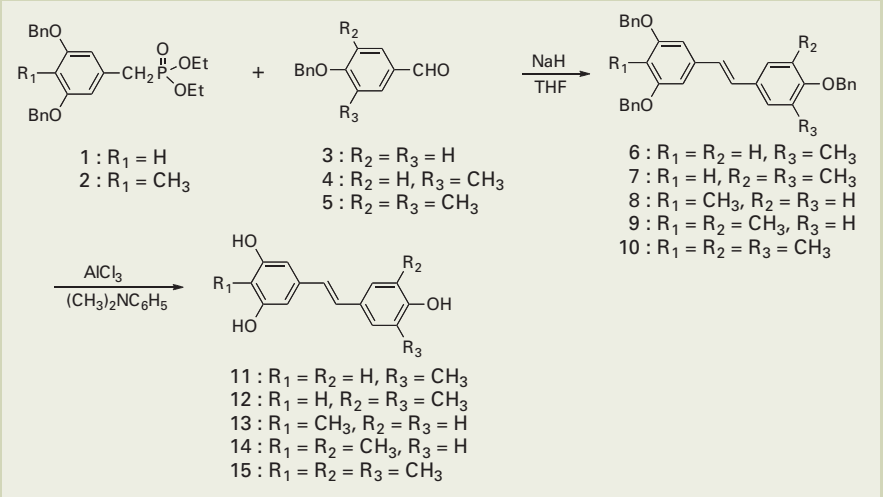


Fig. 10 Synthesis of methyl analogues of resveratrol.

order kinetics, when the concentration of resveratrols was maintained at more than a 10-fold excess of the G• concentration. The second-order rate constant ($k$) for hydrogen abstraction was determined from the linear plot of pseudo-first-order rate constant vs the resveratrol concentration. 3'-Methylresveratrol (**11**), where one methyl group was introduced at the ortho position relative to the 4'-hydroxyl group, showed a significantly increased radical scavenging activity compared to resveratrol. A greater $k$ value was also obtained in compound **12**, which has methyl groups at both positions ortho to 4'-hydroxyl group. In comparison to resveratrol, a 6-fold greater $k$ value was observed with 4-methylresveratrol (**13**), indicating that the 4-methyl group also affects the radical scavenging activities of the 4'-hydroxyl group. Similar to the methyl analogues (**11** and **12**) of resveratrol, the $k$ value of **13** was increased by the introduction of methyl ortho to the 4'-hydroxyl group. Among resveratrol and its derivatives, compound **15** had the strongest antioxidative activity with a 60-fold greater $k$ value than that of resveratrol.

In order to verify that the *o*-methyl group contributes to delocalization of the unpaired electron in the corresponding phenoxyl radical, the ESR spectrum was measured for a solution containing **15** and G• by a JEOL X-band spectrometer (JES-FA100) as shown in **Figure 11**a. The observed ESR signals were characterized as the phenoxyl radical derived from **15** by computer simulation with the hyperfine splitting (hfs) values ($a_{CH3}^{3'}$(3H), $a_{CH3}^{5'}$(3H) = 0.141 mT, $a_H^{\alpha}$(1H) = 0.601 mT) as shown in **Figure 11**b. We clearly demonstrated that the delocalization of the unpaired electron to the *o*-methyl groups by hyperconjugation results in the stronger antioxidative ability of *o*-methyl derivatives as compared to resveratrol.

## Effect on the genotoxicity

We next considered the effect of the *o*-methyl group on genotoxicity of resveratrol by means of the frequency of CA [49]. Chinese hamster lung (CHL) cells were incubated with resveratrol and its analogues for 48 h, and the number of cells with structural CAs was counted after chromosome preparation. **Figure 12**a is a typical result of CA tests and

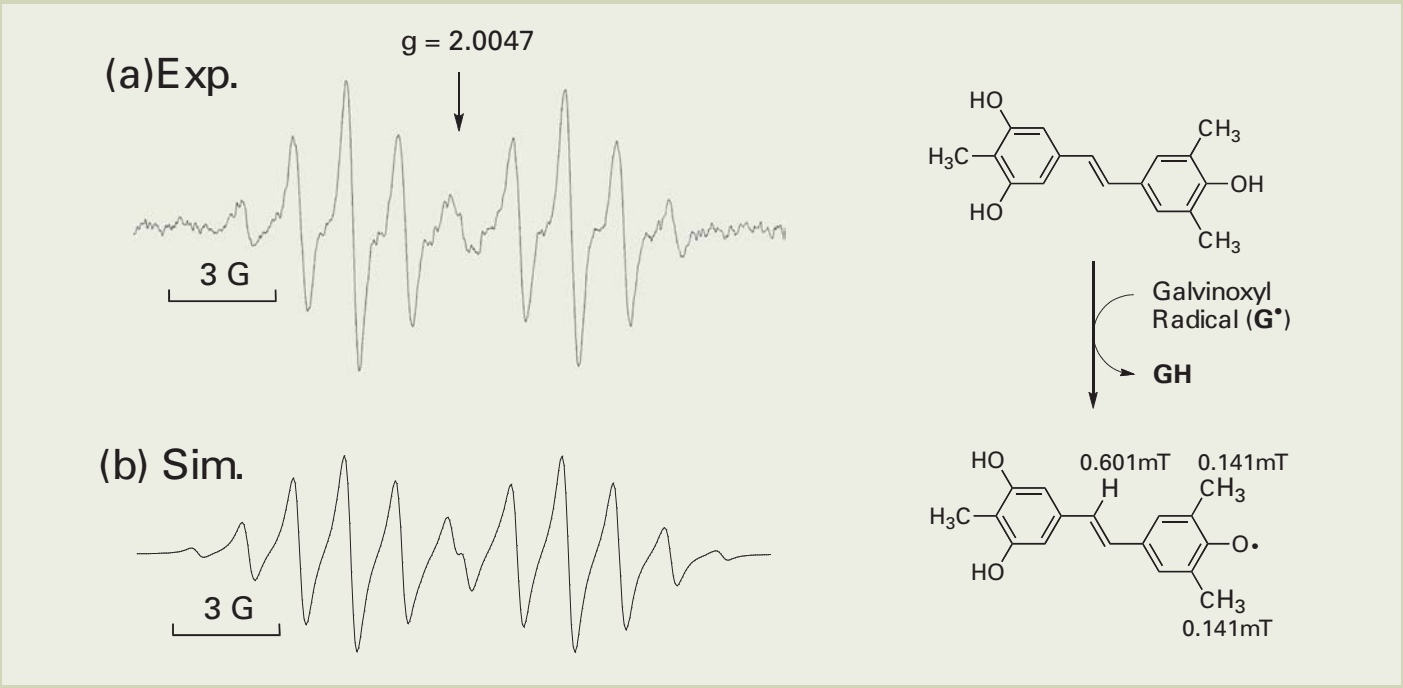


Fig. 11 (a) ESR spectrum of phenoxyl radical generated in the reaction of 15 ($5.0 \times 10^{-4}$ M) with G• ($5.0 \times 10^{-5}$ M) in deaerated MeCN at 298K. (b) The computer simulation spectrum.

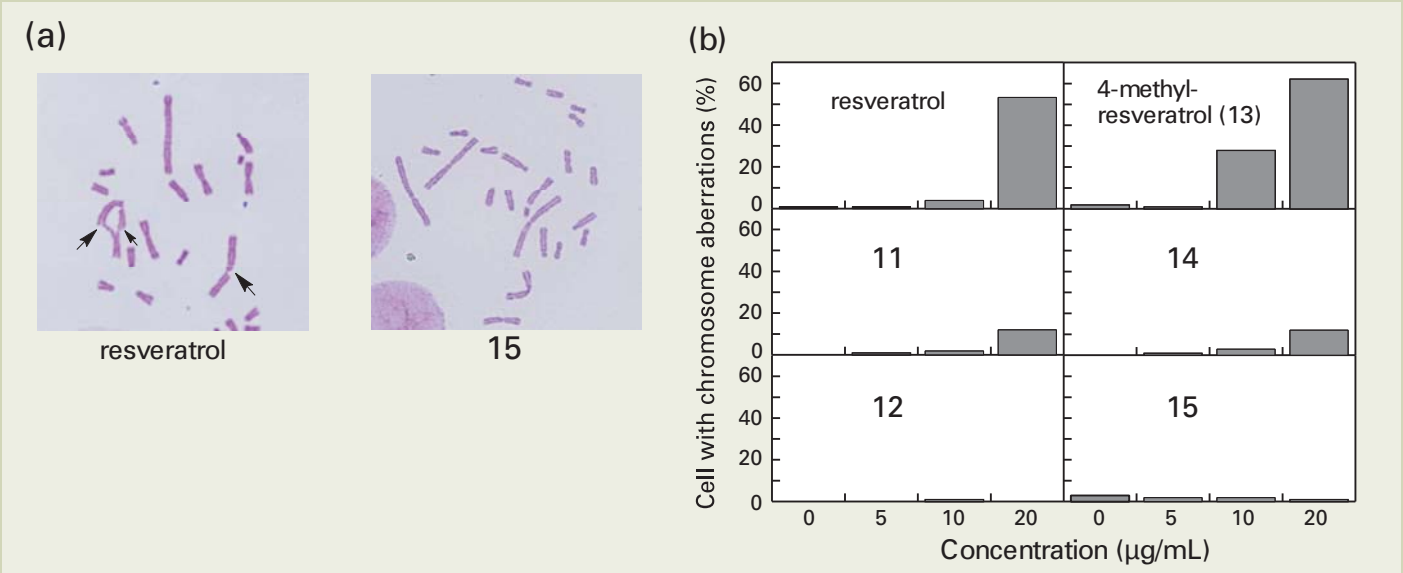


Fig. 12 (a) Micrograph of representative chromosomes in CHL cells treated with 20 μg/ml of resveratrol or **15** for 48 h. Arrows indicate the structural CA. (b) Results of CAs induced in vitro by resveratrol and methyl analogues.

the frequency of CA is summarized in Figure 12b. In agreement with a previous report, resveratrol induced a high frequency of CA consisting of obvious chromatid gaps and chromatid breaks. 4-Methylresveratrol (**13**) showed a slightly higher frequency of CA compared to resveratrol. Remarkably, *o*-methyl groups relative to 4'-hydroxyl group resulted in reduced genotoxicity. In the case of **15**, chromosomes were almost normal as shown in Figure 12a. It is noteworthy that the frequency of CA induced by **11** and **14** was low, whilst CA induced by **12** and **15** was almost insignificant. These results suggest that two methyl substitutions reduce CA even more significantly than a single methyl substitution.

## Conclusion

The primary goal of this project was to develop a novel antioxidant, with potential for clinical usage and/or chemoprevention of diseases associated with reactive oxygen species. The planar catechin analogue that we synthesized from Cat was constrained to be planar compared with the structure of Cat, by taking advantage of the formation of a bridge between the 3-OH group on ring C and C6' on ring B. As compared with Cat, PC1 showed strong radical scavenging activities towards both galvinoxyl radicals and cumylperoxyl radicals. The $O_2^{\bullet-}$ generating ability of the dianion form of PC1 was much lower than that of Cat, suggesting that PC1 may be a promising novel antioxidant with reduced prooxidant activity. In fact, PC1 inhibited DNA-strand scission induced by the Fenton reaction efficiently, whereas Cat exhibited not only antioxidant properties in the same reaction but also prooxidant properties consistent with enhanced DNA strand cleavage. The prevention of polyphenols toward coronary diseases and cancer is due to antioxidant properties of polyphenols which should rely, at least in part, on their ability to inhibit lipid peroxidation in plasma low-density lipoproteins (LDL). The proper lipophilicity of PC1 owing to its molecular planarity might be favorable for its antioxidant effect into LDL or cell membrane. If the hydrophobicity of PC1 could be controlled so as to fine-tune its membrane binding and penetration into the phospholipid bilayer, PC1 might be valuable in the development of a new type of clinically useful antioxidant. Therefore the synthesis of planar catechin analogues, the lipophicity of which is controlled by changing the length of the alkyl chains instead of methyl group in PC1 and their antioxidant abilities are currently underway in our laboratories [50].

We have also described the synthesis, antioxidative ability and genotoxicity of resveratrol analogues with methyl groups ortho to the 4'-hydroxyl group. We demonstrated enhanced antioxidative activity coupled with reduced genotoxicity, rendering the methyl analogues **11–15** potentially valuable for development of drugs effective for various types of diseases caused by oxidative stress. The genotoxicity of resveratrol has been attributed to scavenging of tyrosyl free radicals in the R2 subunit of ribonucleotide reductase that catalyzes the rate limiting step of de novo DNA synthesis [51]. We previously reported that the 4'-hydroxyl group is responsible for scavenging tyrosyl radicals, which cause SCE and CA [52]. Therefore, it is possible that the lower CA frequency for **11–15** as compared to resveratrol could be explained by the steric hindrance of the o-methyl group with respect to the radical scavenging reaction between the 4'-hydroxyl group and the tyrosyl radical. Comparison of resveratrol and its o-methyl analogue (**11** and **12**) to the 4-methyl analogues (**13-15**), which have increased CA, shows a potential functional relationship between structure and enhanced radical scavenging activity. Further detailed insight and in vivo studies to fully exploit these potential benefits are currently underway.

## Acknowledgment

I thank Dr. I. Nakanishi at National Institute of Radiological Sciences and my colleagues at National Institute of Health Sciences for their enthusiasm in pursuing this field of research. I thank Dr. H. Okuda at National Institute of Health Sciences and Dr. N Miyata at Nagoya City University for helpful discussions. This work was supported by Grant-in-Aids for Scientific Research (B) (No. 17390033, 20390038) from the Ministry of Education, Culture, Sports, Science and Technology, Japan.

## References

[1] Kühnau, J. (1976) The flavonoids. A class of semi-essential food components: their role in human nutrition. *Word Rev. Nutr. Diet* **24**, 117-191.

[2] Havsteen, B. (1983) Flavonoids, a class of natural products of high pharmacological potency. *Biochem Pharmacol.* **32**, 1141-1148.

[3] Terao, J., Piskula, M. and Yao, Q. (1994) Protective effect of epicatechin, epicatechin gallate and quercetin on lipide peroxidation in phospholipid bilayers. *Arch. Biochem. Biophys.* **308**, 278-284.

[4] Salah, N., Miller, N.J., Paganga, G., Tijburg, L., and Bolwell, G.P., Rice-Evans, C.A. (1995) Polyphenolic flavonoids as scavengers of aqueous phase radicals and as chain breaking antioxidants. *Arch. Biochem. Biophys.* **322**, 339-346.

[5] Rice-Evans C.A., Miller, N.J., and Paganga, G. (1996) Structure-antioxidant activity relationships of flavonoids and phenolic acids. *Free Radic. Biol. Med.* **20**, 933-956.

[6] Jovanovic, S.V., Streenken, S., Tosic, M., Marjanovic, B., and Simic, M. G. (1994) Flavonoids as antioxidants. *J. Am. Chem. Soc.* **116**, 4846-4851.

[7] Hanasaki, Y., Ogawa, S. and Fukui, S. (1994) The correlation between active oxygen scavenging and antioxidative effects of flavonoids. *Free Radic. Biol. Med.* **16**, 845-850.

[8] Hu, J. P., Calomme, M., Lasure, A., De Bruyne, T., Pieters, L., Vlietinck, A. and Vanden Berghe, D.A. (1995) Structure-activity relationships of flavonoids with superoxide scavenging ability. *Biol. Trace. Elem. Res.* **47**, 327-331.

[9] Morel, I., Lescoat, G., Cogrel, O., Sergent, O., Pasdeloup, N., Brissot, P., Cillard, P., and Cillard, J. (1993) Antioxidant and iron-chelating activities of the flavonoids catechin, quercetin and diosmetin on iron-loaded rat hepatocyte cultures. *Biochem. Pharmacol.* **45**, 13-19.

[10] Elangovan,V.,Sekar,N.,and Govindasamy, S.(1994) Chemopreventive potential of dietary bioflavonoids against 20-methylcholanthrene induced tumorigenesis. *Cancer Lett.* **87**, 107-113.

[11] Ochiai, M., Nagao, M., Wakabayashi, K., and Sugimura, T. (1984) Superoxide dismutase acts an enhancing factor for quercetin mutagenesis in rat-liver cytosol by preventing its decomposition. *Mutat. Res.* **129**, 19-24.

[12] Rueff, J., Laires, A., Borba, H., Chaveca, T., Gomes, M. I. and Halpern, M. (1986) Genetic toxicology of flavonoids: the role of metabolic conditions in the induction of reverse mutation, SOS functions and sister-chromatid exchanges. *Mutagenesis* **1**, 179-183.

[13] Popp, R. and Schimmer, O. (1991) Induction of sister-chromatid exchanges(SCE), polyploidy, and micronuclei by plant flavonoids in human lymphocyte cultures. A comparative study or 19 flavonoids. *Mutat. Res.* **246**, 205-213.

[14] Sahu, S.C. and Washington M.C. (1991) Effects of antioxidants on quercetin-induced nuclear DNA damage and lipid peroxidation. *Cancer Lett.* **60**, 259-264.

[15] Pamukcu, A.M., Yalciner, S., Hatcher, J.F. and Bryan, G.T. (1980) Quercetin, a rat intestinal and bladder carcinogen present in bracken fern (Pteridium aquilinum). *Cancer Res.* **40**, 3468-3472.

[16] Toxicology and carcinogenesis studies of quercetin in F344 rats (1992) National Toxicology Program (NTP) Technical Report, NTP TR 409, NIH publication No.93-147478.

[17] Yamashita, N., Tanemura, H. and Kawanishi, S. (1999) Mechanism of oxidative DNA damage induced by quercetin in the presence of Cu(II). *Mutat. Res.* **425**, 107-115.

[18] Greenspan, H.C. and Aruoma, O.I. (1995) Oxidative stress and apoptosis in HIV infection: a role for plant-derived metabolites with synergistic antioxidant activity. *Immunol Today.* **15**, 209-213.

[19] Bors, W., Michel, C. and Saran, M. (1994) Flavonoid antioxidants: rate constants for reactions with oxygen radicals. *Methods Enzymol,* **234**, 420-429.

[20] Jovanovic, S.V., Steenken, S., Tosic, M., Marjanvic, B. and Simic, M.G. (1994) Flavonoids as antioxidants. *J*

*Am Chem Soc*. **116**, 4846-4851.
[21] Decharneux, T., Dubois, F., Beauloye, C., Wattiaux-De Coninck, S. and Wattiaux, R. (1992) Effect of various flavonoids on lysosomes subjected to an oxidative or an osmotic stress. *Biochem Pharmacol*. **44**, 1423-1428.
[22] Torel, J., Cillard, J. and Cillard, P. (1986) Antioxidant activity of flavonoids and reactivity with peroxy radical. *Phytochemistry*. **25**, 383-385.
[23] Dangles, O., Fargeix, G. and Dufour, C. (2000) Antioxidant properties of anthocyanins and tannins: a mechanistic investigation with catechin and the 3,4,7-trihydroxyflavylium ion. *J Chem Soc Perkin Trans 2*. 1653-1663.
[24] Valcic, S., Burr, J.A., Timmermann, B.N. and Liebler, D.C. (2000) Antioxidant chemistry of green tea catechins. New oxidation products of (-)-epigallocatechin gallate and (-)-epigallocatechin from their reactions with peroxyl radicals. *Chem Res Toxicol*. **13**, 801-810.
[25] Rice-Evans CA, Miller NJ, Paganga G. (1996) Structure-antioxidant activity relationships of flavonoids and phenolic acids. *Free Radic Biol Med*. **20**, 933-956.
[26] van Acker, SABE., de Groot, M.J., van den Berg, D.J., Tromp, MNJL., Doone-Op den Kelder, G., van der Vijgh, WJF. and Bast, A. (1996) A quantum chemical explanation of the antioxidant activity of flavonoids. *Chem Res Toxicol*. **9**, 1305-1312.
[27] Fukuhara, K., Nakanishi, I., Kansui, H., Sugiyama, E., Kimura, M., Shimada, T., Urano, S., Yamaguchi, K. and Miyata, N. (2002) Enhanced radical-scavenging activity of a planar catechin analogue. *J. Am. Chem. Soc*. **124**, 5952-5953.
[28] Nakanishi, I., Miyazaki, K., Shimada, T., Ohkubo, K., Urano, S., Ikota, N., Ozawa, T., Fukuzumi, S. and Fukuhara K. (2002) Effects of metal ions distinguishing between one-step hydrogen- and electron-transfer mechanisms for the radical-scavenging reaction of (+)-catechin. *J. Phys. Chem.* A **106**, 11123-11126.
[29] Nakanishi, I., Fukuhara, K., Shimada, T., Ohkubo, K., Iizuka, Y., Inami, K., Mochizuki, M., Urano, S., Itoh, S., Miyata, N. and Fukuzumi S. (2002) Effects of magnesium ion on kinetic stability and spin distribution of phenoxyl radical derived from a vitamin E analogues: mechanistis insight into antioxidative hydrogen transfer reaction of vitamin E. *J. Chem. Soc. Perkin2*, 1520-1524.
[30] Nakanishi, I., Matsumoto, S., Ohkubo, K., Fukuhara, K., Okuda, H., Inami, K., Mochizuki, M., Ozawa, T., Itoh, S., Fukuzumi, S. and Ikota, N. (2004) EPR study on stable magnesium complexes of phenoxyl radicals derived from a vitamin E model and its deuterated derivatives. *Bull. Chem. Soc. Jpn.* **77**, 1741-1744.
[31] Nakanishi, I., Kawashima, T., Ohkubo, K., Kanazawa, H., Inami, K., Mochizuki, M., Fukuhara, K., Okuda, H., Ozawa, T., Itoh, S., Fukuzumi, S. and Ikota, N. (2005) Electron-tansfer mechanism in radical-scavenging reactions by a vitamin E model in a protic medium. *Org. Biomol. Chem*. **3**, 626 – 629.
[32] Nakanishi, I., Ohkubo, K., Miyazaki, K., Hakamata, W., Urano, S., Ozawa, T., Okuda, H., Fukuzumi, S., Ikota, N. and Fukuhara, K. (2004) A planar catechin analogue having a more negative oxidation potential than (+)-catechin as an electron–transfer antioxidant against a peroxyl Rradical. *Chem. Res. Toxicol*. **17**, 26-31.
[33] Nakanishi, I., Fukuhara, K., Ohkubo, K., Shimada, T., Kansui, H., Kurihara, M., Urano, S., Fukuzumi, S. and Miyata, N. (2001) Superoxide anion generation via electron-transfer oxidation of catechin dianion by molecular oxygen in an aprotic medium. *Chem. Lett.* 1152-1153.
[34] Nakanishi, I., Miyazaki, K., Shimada, T., Inami, K., Mochizuki, M., Urano, S., Okuda, H., Ozawa, T., Fukuzumi, S., Ikota, N. and Fukuhara, K. (2003) Kinetic study on the electron-transfer oxidation of the phenolate anion of a vitamin E model by molecular oxygen generating superoxide anion in an aprotic medium. *Org. Biomol. Chem*. **1**, 4085-4088.
[35] Fukuhara, K., Nakanishi, I., Shimada, T., Miyazaki, K., Hakamata, W., Urano, S., Ikota, N., Ozawa, T., Okuda, H., Miyata, N. and Fukuzumi S. (2003) A planar catechin analogue as a promising antioxidant with reduced prooxidant activity. *Chem. Res. Toxicol*. **16**, 81-86.
[36] Hakamata, W., Muroi, M., Nishio, T., Oku, T., Takatsuki, A., Osada, H., Fukuhara, K., Okuda, H. and Kurihara, M. (2006) N-linked oligosaccharide processing enzymes as molecular targets for drug discovery. *J. Appl. Glycosci*, **53**, 149-154.
[37] Mehta, A., Zitzmann, N., Rudd, P.M., Block, T.M. and Dwek, R.A. (1998) a-Glucosidase inhibitors as potential broad based anti-viral agents. *FEBS Letters*, **430**, 17-22.
[38] Rotondo, S., Rajtar, G., Manarini, S., Celardo, A., Rotillo, D., de Gaetano, G., Evangelista, V. and Cerletti, C. (1998) Effect of trans-resveratrol, a natural polyphenolic compound, on human polymorphonuclear leukocyte function. *Br J Pharmacol* **123**, 1691-1699.
[39] Delmas, D., Jannin, B. and Latruffe, N. (2005) Resveratrol: preventing properties against vascular alterations and ageing. *Mol Nutr Food Res* **49**, 377-395.
[40] Jang, M., Cai, L., Udeani, G. O., Slowing, K. V., Thomas, C. F., Beecher, C. W., Fong, H. H., Farnsworth, N. R., Kinghorn, A. D., Mehta, R. G., Moon, R. C. and Pezzuto, J. M. (1997) Cancer chemopreventive activity of resveratrol, a natural product derived from grapes. *Science* **275**, 218-220.
[41] Fremont, L., Belguendouz, L. and Delpal, S. (1999) Antioxidant activity of resveratrol and alcohol-free wine polyphenols related to LDL oxidation and polyunsaturated fatty acids. *Life Sci* **64**, 2511-2521.
[42] Belguendouz, L., Fremont, L. and Linard, A. (1997) Resveratrol inhibits metal ion-dependent and independent peroxidation of porcine low-density lipoproteins. *Biochem Pharmacol* **53**, 1347-1355.
[43] Stojanovic, S., Sprinz, H. and Brede, O. (2001) Efficiency and mechanism of the antioxidant action of trans-resveratrol and its analogues in the radical liposome oxidation. *Arch Biochem Biophys* **391**, 79-89.
[44] Nakanishi, I., Shimada T., Ohkubo K., Shimizu T., Urano S., Okuda H., Miyata N., Ozawa T., Anzai K., Fukuzumi S., Ikota N. and Fukuhara K. (2007) Involvement of electron transfer in the radical-scavenging reaction of resveratrol, *Chem. Lett*., **36**, 1276-1277.
[45] Matsuoka, A., Takeshita, K., Furuta, A., Ozaki, M., Fukuhara, K. and Miyata, N. (2002) The 4'-hydroxy group is responsible for the in vitro cytogenetic activity of resveratrol. *Mutat Res* **521**, 29-35.
[46] Matsuoka, A., Furuta, A., Ozaki, M., Fukuhara, K. and Miyata, N. (2001) Resveratrol, a naturally occurring polyphenol, induces sister chromatid exchanges in a Chinese hamster lung (CHL) cell line. *Mutat Res* **494**, 107-113.
[47] Fukuhara, K. and Miyata N. (1998) Resveratrol as a new type of DNA-cleaving agent. *Bioorg. Med. Chem. Lett*. **8**, 3187-3192.
[48] Fukuhara, K., Nagakawa, M., Nakanishi, I., Ohkubo, K., Imai, K., Urano, S., Fukuzumi, S., Ozawa, T., Ikota, N., Mochizuki, M., Miyata, N. and Okuda, H. (2006) Structural basis for DNA-cleaving activity of resveratrol in the presence of Cu(II). *Bioorg Med Chem* **14**, 1437-1443.
[49] Fukuhara, K., Nakanishi, I., Matsuoka, A., Matsumura, T., Honda, S., Hayashi, M, Ozawa, T., Miyata, N., Saito, S., Ikota, N. and Okuda, H. (2008) Effect of methyl substitution on antioxidative property and genotoxicity of resveratrol. *Chem. Res. Toxico*l., **21**, 282-287.
[50] Hakamata, W., Nakanishi, I., Masuda, Y., Shimizu, T., Higuchi, H., Nakamura, Y, Oku, T., Saito, S., Urano, S., Ozawa, T., Ikota, N., Miyata, N., Okuda, H. and Fukuhara, K. (2006) Planar catechin analogues with alkyl side chains, as a potent antioxidant and an a-glucosidase inhibitor. *J. Am. Chem. Soc*. **128**, 6524-6525.
[51] Fontecave, M., Lepoivre, M., Elleingand, E., Gerez, C. and Guittet, O. (1998) Resveratrol, a remarkable inhibitor of ribonucleotide reductase. *FEBS Lett* **421**, 277-279.
[52] Matsuoka, A., Lundin, C., Johansson, F., Sahlin, M., Fukuhara, K., Sjoberg, B. M., Jenssen, D. and Onfelt, A. (2004) Correlation of sister chromatid exchange formation through homologous recombination with ribonucleotide reductase inhibition. *Mutat Res* **547**, 101-107.

# Development of Nanoimprint Mold Using JBX-9300FS

**Morihisa Hoga[†], Mikio Ishikawa[†], Naoko Kuwahara[†]**
**Tadahiko Takikawa[††] and Shiho Sasaki[††]**

**Dai Nippon Printing Co., Ltd [†]Research & Development Center**
**[††]Electronic Device Laboratory**

Nanoimprint attracts attention as a mass production technique in nano-scale fabrication. One of the key issues of nanoimprint is mold fabrication; because its resolution limit depends on mold. Since electron-beam (e-beam) writers for semiconductor photomask fabrication have difficulties in writing such a very fine pattern, we introduced a JEOL JBX-9300FS. As a result, the trial production of the 22 nm half pitch nanoimprint mold for the CMOS process development TEG has become possible. Furthermore, using this accomplishment, we have been developing the mold fabrication processes for patterned media. In this paper, we demonstrate that the JEOL JBX-9300FS is an effective electron-beam writer for the mold fabrication with a pattern of 30 nm or less.

## Introduction

Development of the nanoimprint is progressing as a technique which makes nanometer-scale patterns. Nanoimprint is a technique extended from hot embossing which uses a heat-cycle process, or 2P method (Photo Polymerization) which uses photo-sensitive polymer. Nanoimprint lithography was proposed by S. Chou, then-Professor of University of Minnesota in 1995. He showed that nanoimprint was able to be used as lithography by removing residual layer with oxygen ashing, and demonstrated that this technique can transfer a fine pattern of 200 nm or less [1], and he named it "Nanoimprint Lithography (NIL)." This proposal is a starting point which attracts attention as mass production technique in the nanotechnology field in recent years. At present, two techniques are being studied for practical applications of NIL. One is Next Generation Lithography (NGL) for semiconductor, and another is patterned media for hard disk drive that is aimed at high-density magnetic recording.

[†]250-1 Wakashiba, Kashiwa-shi, Chiba, Japan

houga_m@mail.micro.dnp.co.jp

NIL was selected as one of candidate techniques of semiconductor lithography as NGL in the 2003 edition of the International Technology Roadmap for Semiconductor (ITRS). Since then, we have been developing the nanoimprint mold because we situated mold technology as an extension of photomask technology. Furthermore, utilizing the technique cultivated through this development, we have undertaken the mold development for patterned media. This paper shows the progress of these developments by summarizing the reports presented at various technical symposiums up to now.

## Writing Accuracy of JBX-9300FS

For writing advanced photomask patterns, an electron-beam writer such as the JEOL JBX-3050MV, which uses a Variable Shaped (Electron) Beam (VSB) with an accelerating voltage of 50 kV, is generally used. However, at present, it is difficult to write a pattern of 30 nm or less by the 50 kV-VSB technique. Then, a JEOL JBX-9300FS, a 100 kV spot beam (SB) writer, was introduced. The JBX-9300FS uses the same platform as the JEOL JBX-9000MV which is well-used for the fabrication of photomasks, and also incorporates an advanced electron optical system that can focus an electron beam down to 10 nm in diameter.

In semiconductor lithography, it is necessary to form the layer-on-layer by accurately overlaying them. For NGL, the required overlay accuracy is as small as 10 nm or less. In order to perform high-accuracy mold writing that meets this demand, it is required to eliminate the influence of various kinds of external noise; therefore, the JBX-9300FS is installed in a high-precision thermal chamber with magnetic-shield.

Hereinafter, we report the writing accuracy of the introduced JBX-9300FS. ZEP520A resist was used in all experiments. In the experiments except for the CD (critical dimension) linearity test, a quartz substrate for photomask, which has 6 inch squares and 6.35 mm thickness, was used. As for the experiments for the CD linearity, a silicone (Si) wafer was used. A CD-SEM was used for CD measurement, whereas a coordinate-measuring apparatus with a laser interferometer was used for image position measurement.

The CD uniformity accuracies in a deflection field, which is usually called local CD accuracy, are shown in **Fig 1**. This result shows the measurements of respective 25

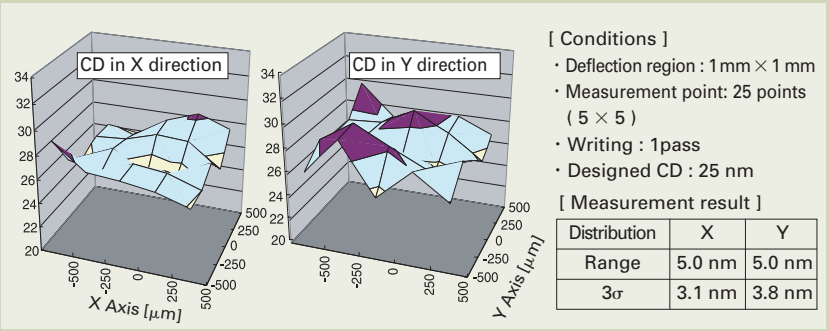


Fig. 1 CD uniformity in a deflection field.

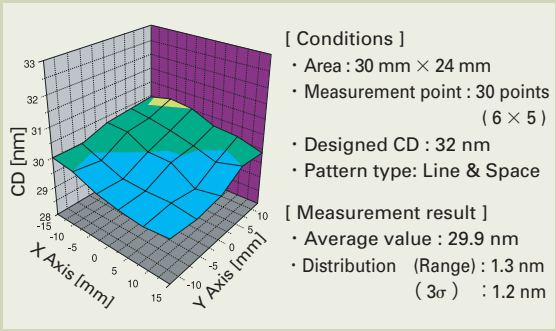


Fig. 2 CD uniformity in a mold area.

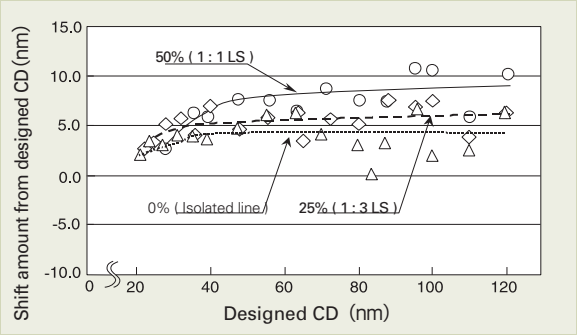


Fig. 3 CD linearity from 22 nm to 120 nm.

Table 1 Image position accuracy in two kinds of deflection field.

1 pass writing

| Deflection field size | | 1mm × 1mm | | 500μm × 500μm | |
|---|---|---|---|---|---|
| Measurement result (map output) | | 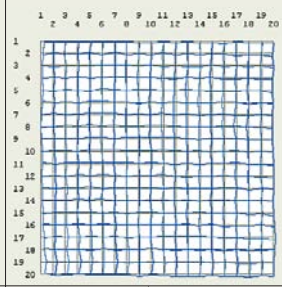 | | 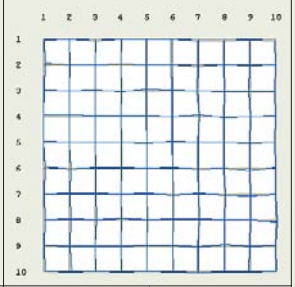 | |
| Distribution | Direction | X | Y | X | Y |
| | Range | 18.5nm | 10.6nm | 8.0nm | 7.5nm |
| | 3σ | 8.2nm | 6.0nm | 5.3nm | 5.0nm |

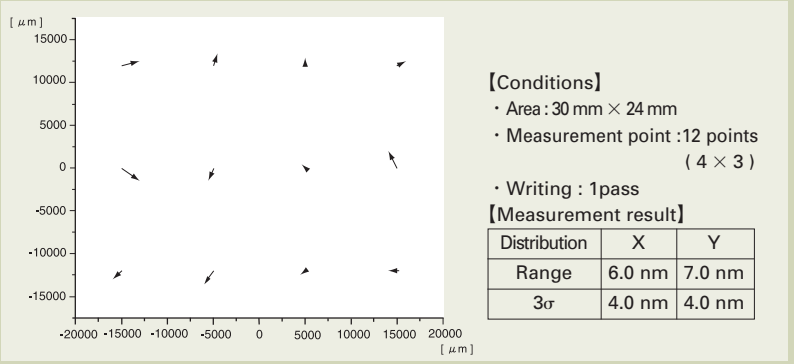


Fig. 4 Image position accuracy in a mold area.

points in both X and Y directions on a isolated line in a deflection field whose area is 1 mm squares and designed CD is 25 nm. As for CD distribution, the ranges are 5.0 nm in both the X and Y directions, and 3σ values are 3.1 nm in the X direction and 3.8 nm in the Y direction. These measurement results demonstrate good CD distributions.

The CD uniformity accuracy in a mold, which is usually called global CD accuracy, is shown in **Fig 2**. This result shows the measurements of 30 points within an area of 30 mm × 24 mm in Line & Space (LS) patterns with a designed CD of 32 nm. The average value is 29.9 nm. As for CD distribution, the range is 1.3 nm, and 3σ value is 1.2 nm. It is noted that local CD accuracy is mainly attributed to e-beam writer, whereas global local CD accuracy is mainly attributed to coating, developing and etching process.

If an accelerating voltage is large, the region of backscattered electrons from a substrate will become as large as 30 μm or more, resulting in a large CD error due to the proximity effect. This effect changes with a designed CD and the coverage factor of patterns in a local area. The CD error due to the proximity effect is evaluated by using the designed CD dependence, which is usually called CD linearity. This CD linearity is shown in **Fig. 3**. This result shows the measurements of the designed CD dependence of three kinds of patterns for designed CD from 22 nm to 120 nm. These three kinds of patterns are an isolated line (one line), LS pattern (line part : space part = 1 : 3) with a coverage factor of 25%, and LS pattern (line part : space part = 1 : 1) with a coverage factor of 50%. The horizontal axis corresponds to the designed CD and the vertical axis indicates the shift amount from the designed CD. By performing a dose correction using a newly developed proximity-effect-correction program, a good linearity is obtained as small as down to 30 nm for the isolated line and 40 nm for the LS pattern of 1 : 1. In addition, the CD error between the isolated line and the LS pattern of 1 : 1 is confined within 5 nm. Moreover, optimizing relevant parameters may be considered to further decrease the error.

The image position accuracy in deflection field (local position accuracy) in two kinds of deflection field is shown in **Table 1**. The two kinds of filed sizes are 1 mm squares and 500 μm squares. 3σ values for 500 μm squares are 5.3 nm in the X direction and 5.0 nm in the Y direction, indicating a high accuracy. In general, if the amount of deflections is increased, a throughput will improve, but the position accuracy will deteriorate. In this experiment, although one-pass writing was adopted, multiple writing will improve the placement accuracy in general. In actual writing, the filed size and multiplicity of writing are selected depending on the accuracy required.

The image position accuracy in a mold area (global position accuracy) is shown in **Fig 4**.

This result shows the measurements of 12 points within an area of 30 mm × 24 mm. 3σ values are 4.0 nm in the X direction and 4.0 nm in the Y direction, indicating a high accuracy.

As presented above, the main writing accuracies of the JBX-9300FS demonstrate that sufficiently high accuracies are obtained with the JBX-9300FS for the present mold development for semiconductor NGL. The following sections show the details of our mold development status.

## Development of Fine Pattern Fabrication Process for Qz and Si Substrates

The diagram of the mold fabrication process flow is shown in **Fig 5**. A quartz or a Si substrate, on which a hard mask is formed for dry etching, is prepared; and then an electron-beam resist film is formed by spin coating. For the material of hard mask, chromium (Cr) membrane is used in the case of a quartz substrate, whereas $SiO_2$ membrane is used in the case of a Si substrate. Using an electron-beam lithography system (for example, the JBX-9000FS), a part to be patterned is irradiated with an electron beam and a resist pattern is formed after development. A hard mask is etched using this resist pattern as a mask, then substrate etching is performed, and next the resist and hard mask are removed. Finally, a master mold which has a relief pattern on its surface is formed. This hard mask process is developed based on the already developed processes for alternating phase shift mask in the case of quartz substrate [2] or for stencil mask used for electron-beam lithography in the case of Si substrate [3]. This process is also subjected to optimization of film thickness compatible with a decreased pattern size. It is noted that when the amount of etchings is small in the case of Si wafer process, a hard mask may not be used and Si may be directly etched using resist layer as a mask.

Examples of LS patterns, which were fabricated on quartz substrates using the JBX-9300FS, are shown in **Fig. 6** [4]. SEM micrographs show that minimum feature size is down to 18 nm half-pitch (hp).

Examples of LS patterns, which were fabricated on Si wafers using the same JBX-9300FS, are shown in **Fig. 7**. SEM micrographs also show that minimum feature size is down to 18 nmhp. However, tilted SEM micrographs show that some adjacent lines are connected. This phenomenon is due to

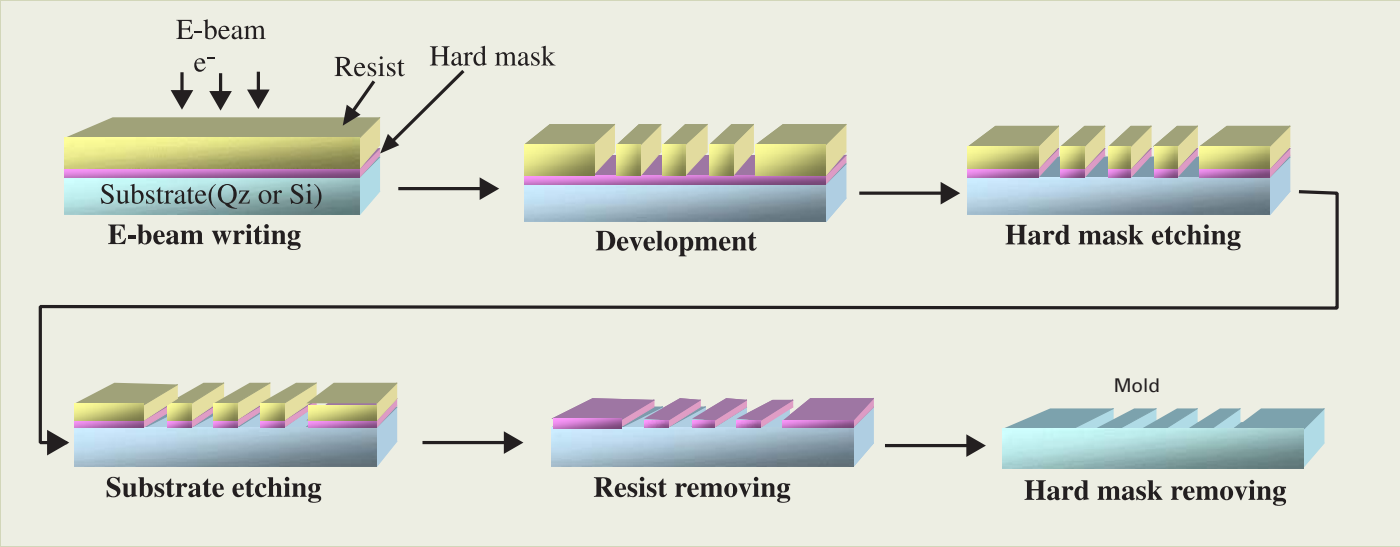


Fig. 5 Mold fabrication process flow.

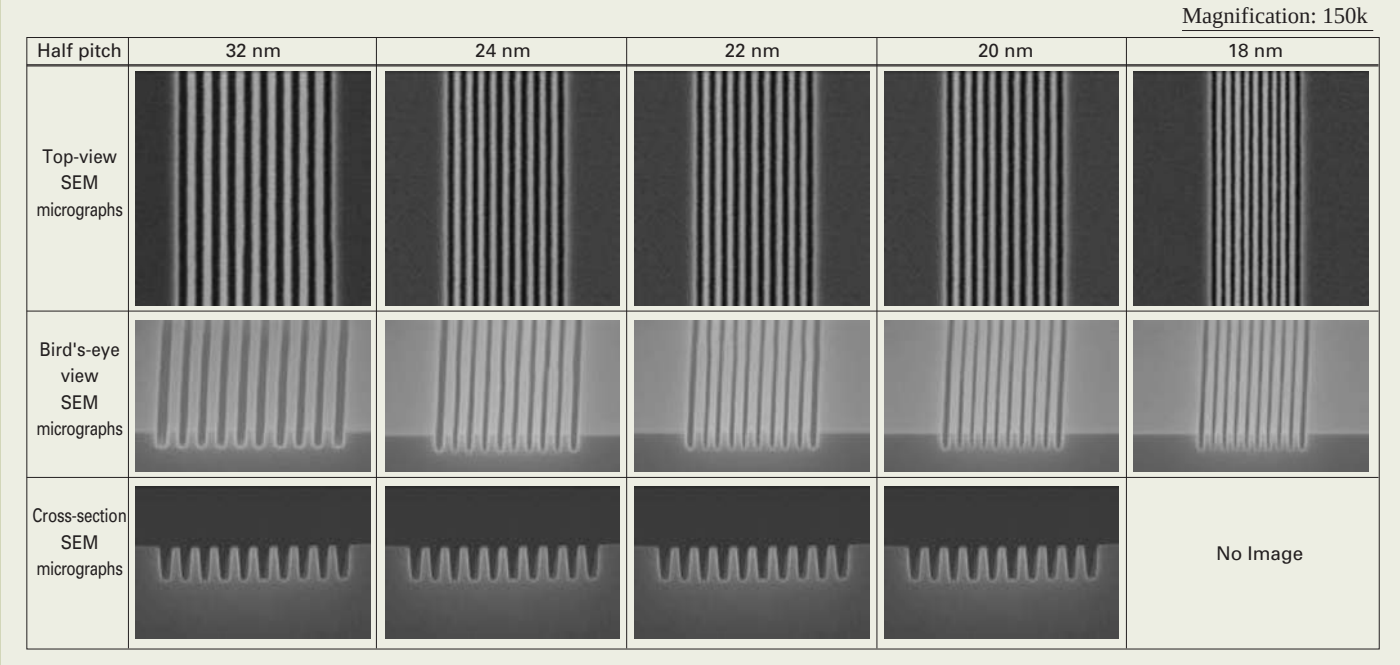


Fig. 6 SEM micrographs of various pitch LS patterns after quartz etching on 6-inch square quartz substrates.

collapse of the resist image in the development process.

## Trial Fabrication of Nanoimprint Mold

At present, the standard specifications for the form factor of the mold are not determined. These specifications are different depending on nanoimprint equipment. Generally, a quartz mold is cut from a 6 inch square quartz substrate and Si-mold is cut from a Si-wafer.

Examples of quartz molds are shown in **Fig. 8**. The left-side photo shows a mold used for nanoimprint equipment of U.S. Molecular Imprints Inc (MII)., and it has 65 mm squares in size. Relief patterns are formed at the center of the mold. This relief-pattern area is 15 μm higher than outer surfaces, constructing a mesa structure. The right-side photo shows a mold used for nanoimprint equipment of Toshiba Machine Co., Ltd. Its bottom surface has 45 mm squares in size, whereas its upper surface has 40 mm squares in size, constructing a trapezoid. LS patterns of 100 nmhp are formed with 35 mm square area on the upper surface. Both of the two molds in Fig. 8 are cut from 6 inch square quartz substrates after relief patterns had been formed.

Trial fabrication of molds for the 22 nmhp CMOS process development was performed. Line-type and hole/pillar-array-type quartz mold patterns of 32 nmhp, 24 nmhp and 22 nmhp, which were written by the JBX-9300FS, are shown in **Fig. 9**. Also **Fig. 10** shows a cross-section SEM micrograph and a top-view SEM micrograph of 22 nmhp nanoimprinted resist image, which was transferred from a quartz mold using nanoimprint equipment of MII [5]. It is seen from the SEM micrographs that resist with a height of 47.5 nm is formed. In addition, LWR (Line Width Roughness) and LER (Line Edge Roughness) values, both of which show the pattern-edge roughness quality are respectively 3.1 nm and 3.5 nm for 3σ values, indicating a sufficiently high roughness quality compared to other lithography techniques.

In the mold pattern writing for patterned media, it is necessary to write a concentric circle pattern on a quartz wafer, therefore, an electron-beam lithography system with a rotation stage is required. We are using the JBX-9300FS for this purpose, that is, for the development of this mold fabrication process. An example of LS patterns of 24

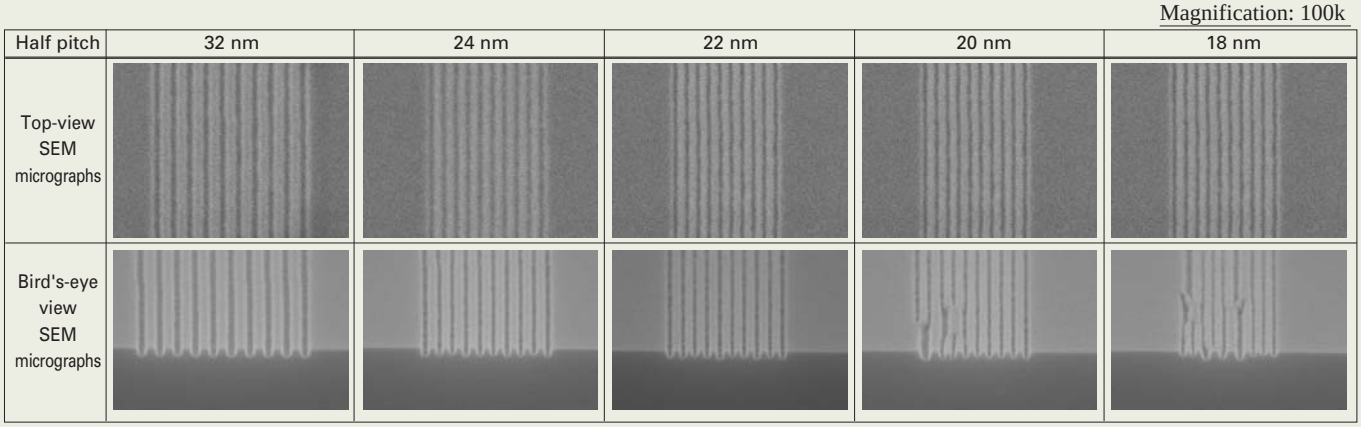


Fig. 7 SEM micrographs of various pitch LS patterns after silicone etching on 200-mm Si wafers.

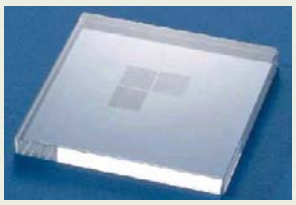

Quartz mold for nanoimprint equipment of Molecular Imprints ( 65 mm × 65 mm )

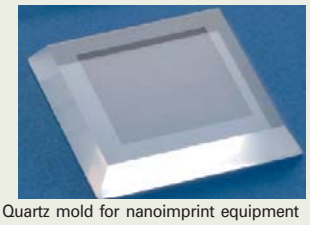

Quartz mold for nanoimprint equipment of Toshiba Machine ( 45 mm × 45 mm )

Fig. 8 Photographs of the outer shapes of quartz molds.

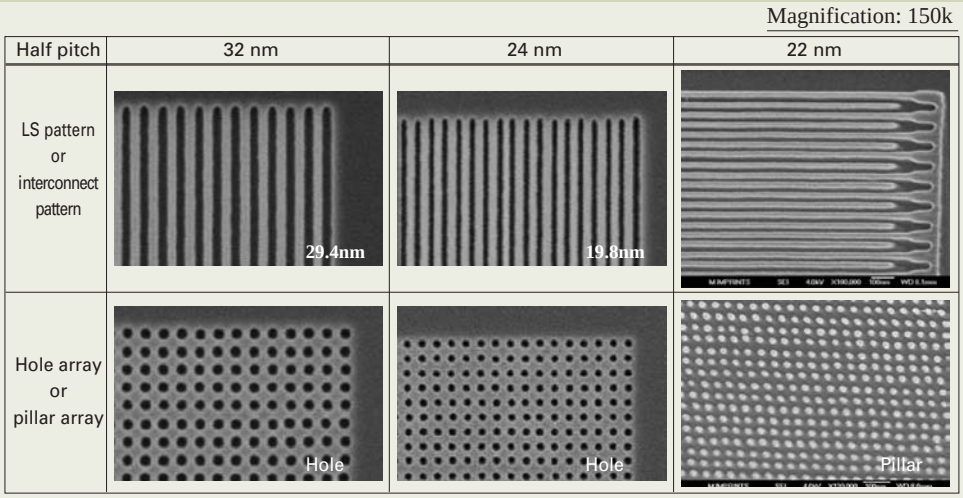


Fig. 9 SEM micrographs of quartz mold patterns written by the JBX-9300FS.

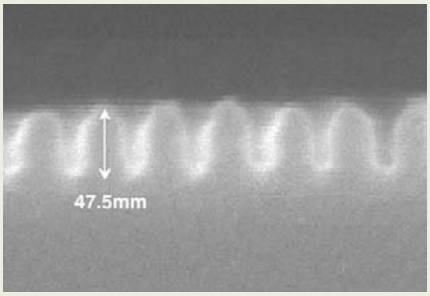


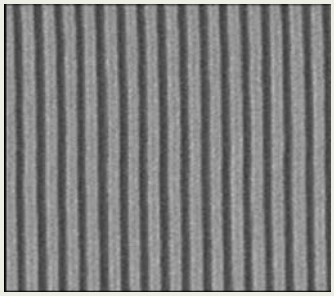

| Item | Measurement result |
|---|---|
| Line width (average) | 24.5 nm |
| LWR (3σ) | 3.1 nm |
| Pitch (average) | 44.7 nm |
| LER (3σ) | 3.5 nm |

Fig. 10 Half-pitch 22 nm nanoimprint resist images and LER measurement result.

nmhp, which were formed on a 60 mm diameter area on a 6 inch diameter quartz wafer, is shown in **Fig. 11**. Now, we are under optimization of writing and process conditions, aiming for forming patterns of 20 nmhp or less.

## Activities for Throughput Improvement

Although a 100 kV-SB electron-beam writer is superior in resolution performance, it has disadvantages such as decrease of resist sensitivity due to higher acceleration and low throughput that arises from the increase of shot numbers by the use of a small-size beam. To overcome these disadvantages, we are taking the following two kinds of activities.

The first activity is the development of a new process using high resolution chemically amplified resist (CAR). The sensitivity of ZEP520A resist at 100 kV, which has high resolution performance, is 300 to 400 $\mu C/cm^2$. This sensitivity is one magnitude lower than that of CAR, 30 to 40 $\mu C/cm^2$. Generally, sensitivity and resolution are tradeoff relations. Then, using the JBX-9300FS, we are trying the introduction of the CAR process, which has a sensitivity of about 100 $\mu C/cm^2$ and has the same resolution performance as ZEP520A. New CAR was kindly provided by Tokyo Ohka Kogyo Co., Ltd. **Table 2** shows a summary of experimental results. In the new CAR process, optimization of bake temperature and improvement of adhesive property between a substrate and resist were performed, and the results of new CAR were compared with the results of other resists [6]. When a primer is Agent B, the new CAR resist resolves 24 nmhp and its sensitivity is 112 $\mu C/cm^2$. Although the resolution performance is inferior to ZEP520A, a new CAR demonstrates a high potential because it has about 100 $\mu C/cm^2$ sensitivity while providing high resolution comparable to ZEP520A. Patterned media like resist images of the new CAR are shown in **Fig. 12**, whereas the results of the formation of Si mold patterns after etching are shown in **Fig. 13**. The results of new CAR are compared with the results of ZEP520A resist. The comparison in Figs 12 and 13 shows that the pattern shape is comparable to ZEP520A and the sensitivity is more than 3 times improved that of ZEP520A.

The second activity is mix writing, combined with a 50 kV-VSB electron-beam writer. There are two methods in mix writing. One is to write patterns smaller than certain size with 100 kV-SB, whereas to write patterns larger than certain size with 50 kV-VSB [7]. Another is to write the outline part with 100 kV-SB, whereas to write the inside part with 50 kV-VSB [8]. The description of the latter method is presented in **Fig. 14** (1). Also in Fig. 14 (2) and (3), micrographs of resist images obtained by the mix writing are shown. The outline part was written with the JBX-9300FS and the inside filled part was written with a JEOL JBX-9000MVII. In addition, Fig. 14 (4) is a tilted view SEM micrograph taken after etching the Si substrate. Although the throughput improvement rate depends on the kinds of the written patterns, mix writing is considered to be an effective technique that utilizes high position accuracy and alignment-writing capability of the JBX-9300FS.

## Conclusion

In preparation for the near-future nanoimprint mold writing for semiconductor lithography, we performed the adjustment of CD and position accuracies of the JBX-9300FS, and expected writing accuracies were ensured. As a result, it became possible to apply our technique using the JBX-9300FS to the development of a nanoimprint mold that contains a fine relief pattern of 30 nm or less. More specifically, we applied our technique to the trial fabrication of the 22 nmhp nanoimprint mold for the CMOS process development TEG.

Furthermore, utilizing the technique cultivated through this development, the mold fabrication process for patterned media has been developing. We are planning to apply this technique to trial mold fabrication for optical or bio devices, which will be promising application fields of nanoimprint in the future.

The biggest present challenge is low throughput. Although we reported, in this paper, on our activities to improve throughput, we have to recognize that these activities are not enough. In order to apply our nanoim-

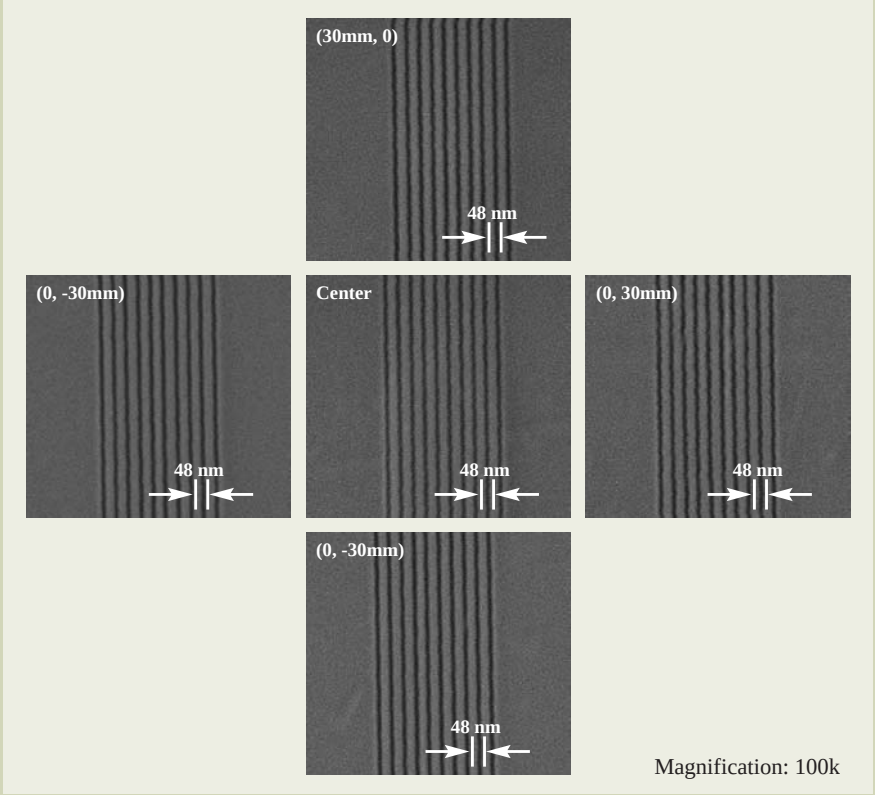


Fig. 11 SEM micrograph of hp 24 nm chrome LS patterns after quartz etching on 6 inch diameter circle quartz wafer.

Table 2 Summary of experimental results.

| E-beam resist | Primer | Resolution(Half Pitch) | Sensitivity |
|---|---|---|---|
| ZEP520A | HMDS | 18 nm | 340 $\mu C/cm^2$ |
| Conventional CAR | HMDS | 50 nm | 30 $\mu C/cm^2$ |
| New-CAR | HMDS | 32 nm | 72 $\mu C/cm^2$ |
| New-CAR | Agent B | 24 nm | 112 $\mu C/cm^2$ |

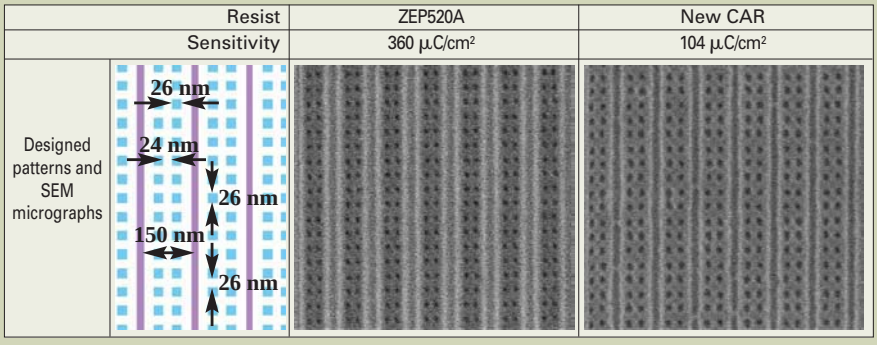


Fig. 12 Example of formation of resist patterns for patterned media.

print mold technique to full-scale production, it is necessary to achieve higher throughput for a 100 kV-SB and to improve resolution performance of a 50 kV-VSB electron-beam writer.

## Acknowledgement

The authors wish to thank people of JEOL Ltd., who are engaged in the JBX-9300FS development and engineering, for their work for higher accuracy and stable operation of the system. In addition, the authors are grateful to Mr. Suzuki of Tokyo Ohka Kogyo Co., Ltd., for providing new chemically amplified resist.

## References

[1] S. Y. Chou: "NANOIMPRINT LITHOGRAPHY" USP 5,772,905
[2] S. Murai, et al: "Establishment of Production Process and Assurance Method for Alternating Phase Shift Masks" *Proc. SPIE* **Vol.4186**, 890 (2000)
[3] M. Kitada, et al.: "Experimental analysis of image placement accuracy of single-membrane masks for LEEPL" *Proc. SPIE* **Vol.5853**, 921 (2005)
[4] A. Fujii, et al: "UV NIL mask making and imprint evaluation" *Proc. SPIE* **Vol.7028**, 70281W-1 (2008)
[5] S. Sasaki, et al: "UV NIL template making and imprint evaluation" *Proc. SPIE* **Vol.7122**, 71223P-1 (2008)
[6] M. Ishikawa, et al: "Si-mold fabrication process by using high-resolution chemically amplified resist" Digest of NNT'08, p204 (2008)
[7] M. Ishikawa, et al: "Hybrid EB-writing technique with a 50kV-VSB writer and a 100kV-SB writer for nanoimprint mold fabrication" *Proc. SPIE* **Vol.6607**, 66073i-1 (2007)
[8] H. Fujita, et al: "Hybrid EB-writing technique with 100kV-SB and 50kV-VSB writers: Use of the former for outlines and latter for bodies after pattern data splitting" *Microelectronic Engineering* **Vol.85**, Issue7, p1514 (2008)

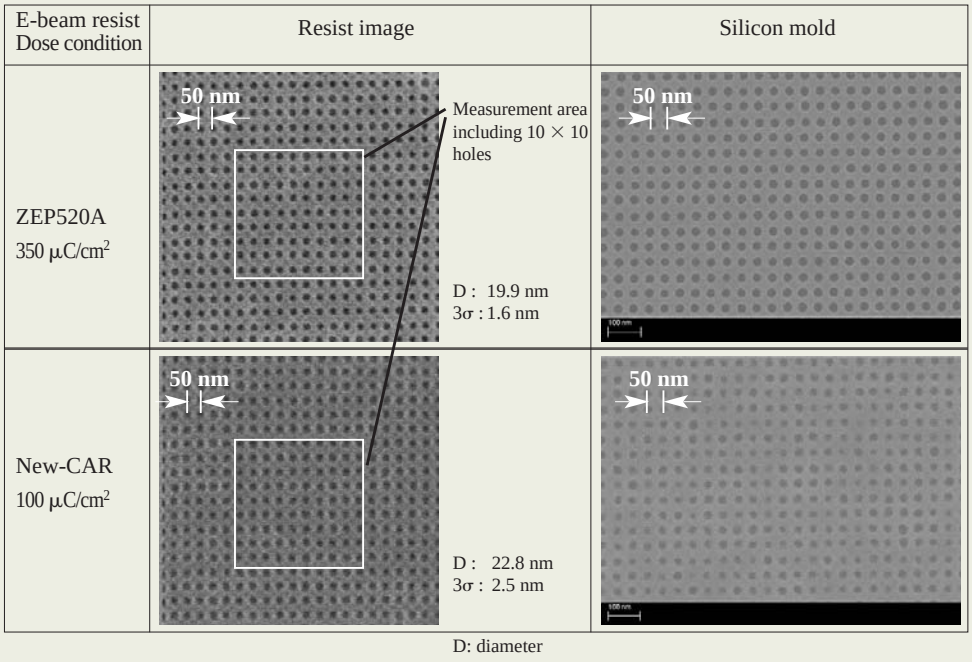


Fig. 13 Trial fabrication of silicone molds with 50 nm pitch hole array.

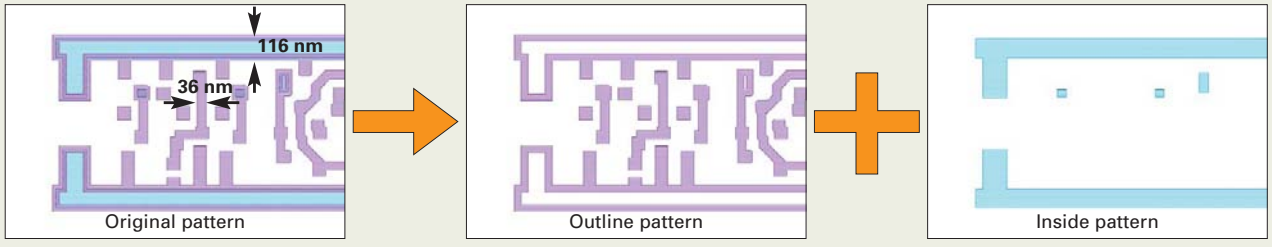


(1) Description of data separation for the outline part and inside filled part

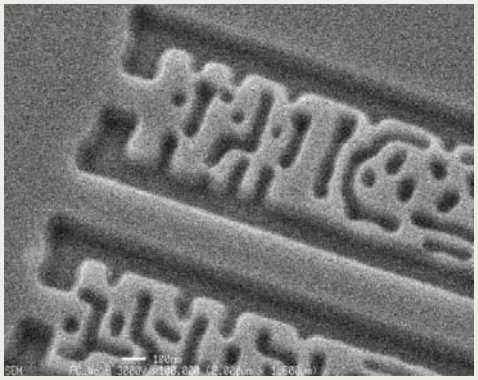

(4) Bird's-eye view SEM micrograph after substrate etching

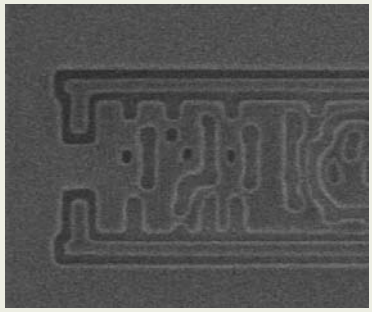

(2) Resist image when only the outline part is written with the JBX-9300FS

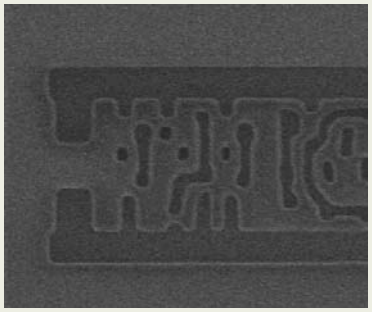

(3) Resist image when overlay writing is performed with the JBX-9000MVⅡ

Fig. 14 Description of mix writing and the result of relief pattern formation by the JBX-9300FS and the JBX-9000MVⅡ.

# Introduction of New Products

## Atomic Resolution Analytical Microscope
# JEM-ARM200F


### *The Power of STEM Cs corrected Microscope*

The JEM-ARM200F is a 200 kV atomic resolution analytical microscope, equipped with a STEM Cs corrector and is capable of atomic level analysis. Improved mechanical and electrical stabilities enable us to perform excellent microscopy and analysis at the highest-level resolution.
The JEM-ARM200F achieves a resolution of 0.08 nm in HAADF-STEM (high-angle annular dark-filed scanning transmission electron microscopy) mode. This is an ultimately high resolution, offering a breakthrough for practical use in nano-research.

***78 pm real imaging by HAADF method (Pico meter order microscopy)***

RAW data

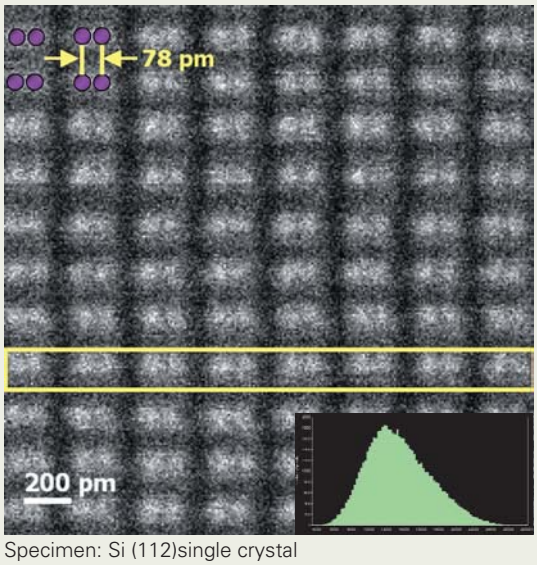


Specimen: Si (112)single crystal

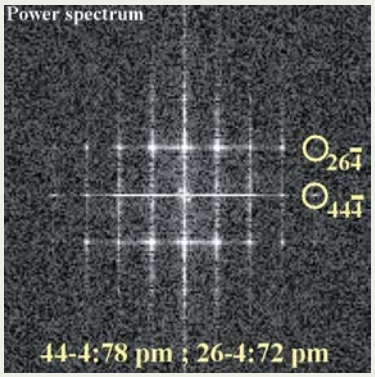


Intensity profile from rectangle area

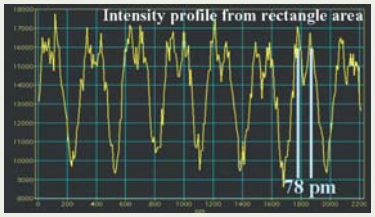


Acc vol:200kV

## *Features*

### Highly stable microscope column and base frame

To enable ultimate-resolution observation and analysis, the column and base frame, which are the core elements of the TEM, have been reinforced for higher stability. That is, the diameter of the column has been increased to improve its mechanical and thermal stability, whereas the base frame has been designed to the optimum geometry to support the robust column. Furthermore, magnetic and heat-insulation shields are optimally placed on the column, reducing the influence of external disturbance.

### Accelerating voltage stability and objective lens current stability

Accelerating voltage stability and objective-lens current stability have been improved, down to 1/2 compared to the conventional one. Thus, the JEM-ARM200F enables higher resolution imaging due to improved stability of not only the column and base frame but also accelerating voltage and objective-lens current.

### Built-in standard spherical aberration (Cs) corrector

The JEM-ARM200F is equipped with a STEM Cs corrector as a standard configuration. Adding special-purpose components to the column enables a TEM Cs corrector to also be installed.
In the standard configuration with a STEM Cs corrector, the JEM-ARM200F can focus an electron beam (probe) to an extremely small probe size, enabling STEM imaging, EDS* analysis and EELS* analysis to all be performed with a probe down to 0.1 nm or less. In addition, the JEM-ARM200F can increase the probe current, allowing for enhanced analysis with a higher signal-to-noise ratio.
In another configuration with a TEM Cs corrector added, the JEM-ARM200F provides ultimately high resolution TEM imaging.

### Variable condenser lens aperture

A condenser lens aperture has variable eight kinds of diameters (holes). Selecting appropriate diameters, according to purposes such as TEM imaging, STEM imaging, EDS analysis and nano-beam analysis, enables observation and analysis under the optimum conditions.

### Specimen anti-contamination device (ACD)

The ACD has been improved to more suppress specimen contamination that adversely affects high-resolution imaging and analysis. That is, the volume of the cooling tank for the cold trap has been increased. This improvement keeps the surroundings of the specimen clean for a long time.

### Scanning transmission image observation

The JEM-ARM200F simultaneously acquires bright-field (BF) and dark-field (DF) scanning transmission (STEM) images. A new image-detection chamber enables a STEM image aperture to be inserted between the BF STEM detector and the DF STEM detector. Thus, both the BF and DF images can be obtained at the same time under the optimum optical conditions.
Furthermore, adding the optional backscattered electron detector and optional dark field detector make it possible for the JEM-ARM200F to simultaneously obtain four images: high-angle annular dark-field (HAADF) image, low-angle dark-filed (LAADF) image, BF image and backscattered electron image.

*: EDS and EELS are optional.

## *HR-Elemental identification by EELS (Atomic column by column EELS map)*

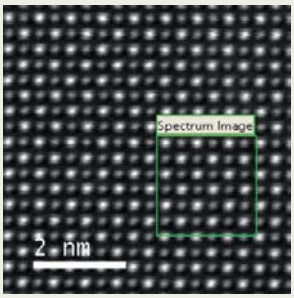


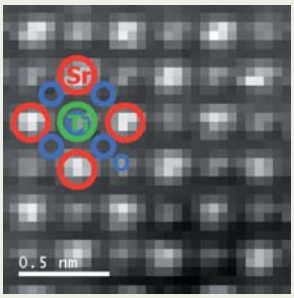


HAADF signal (acquired simultaneously)

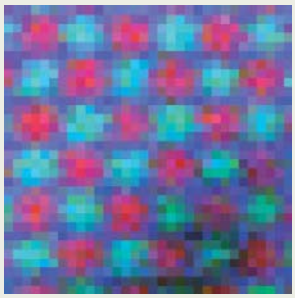

RGB map

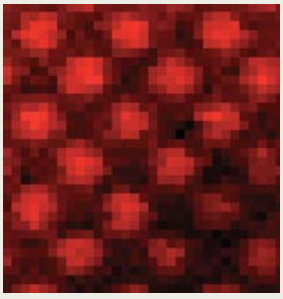

Sr-M map

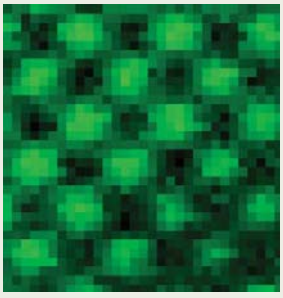

Ti-L map

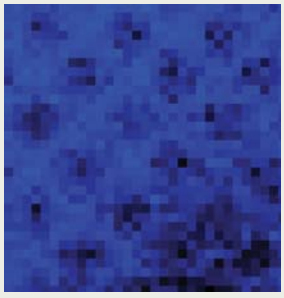

O-K map

# Introduction of New Products

## Field Emission Electron Probe Microanalyzer
# JXA-8530F

The JXA-8530F is a new Field Emission Electron Probe Microanalyzer (FE-EPMA). EPMA is an instrument for non-destructive analyses using various signals generated from specimens. As analytical results, a lot of information such as constituent elements, concentrations, element distribution, surface morphology and mean atomic number in micro to macro areas can be obtained.
The JXA-8530F, an upgraded FE-EPMA, incorporates a Schottky field-emission electron gun that enables analysis of 0.1 μm order. Furthermore, this FE-EPMA acts as a powerful WD/ED combined system. That is, the JXA-8530F accommodates up to five wavelength-dispersive X-ray spectrometers (WDS) and an energy-dispersive spectrometer (EDS). WDS is effective for accurate element analysis, and EDS is advantageous to simultaneous multiple elemental analysis. Also, its user-friendly PC-based operation achieves integrated control of the basic units such as the WDS, EDS, electron optical system (EOS) and specimen stage, and facilitates analyses of various acquisition data.
Thus, this revolutionized FE-EPMA provides high-accuracy element analysis in a wide range of fields, including inspection or research of metals, materials, chemistry and geology.

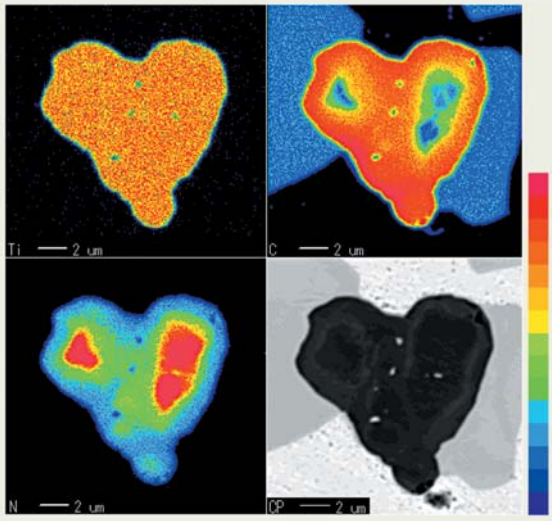


Particle of TiCN in steel.

***X-ray maps of Y in sintered material (AlN).***
The images are enlargements of the maps that were collected using a FE electron gun and a $LaB_6$ electron gun.
The accelerating voltage and probe current are the same as in the maps. The high-brightness FE electron gun can detect Y distributed of small areas in grain boundaries with high intensity.

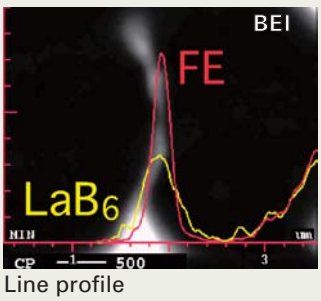


Line profile

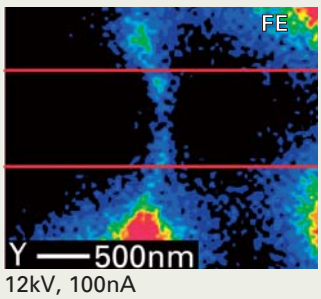


12kV, 100nA

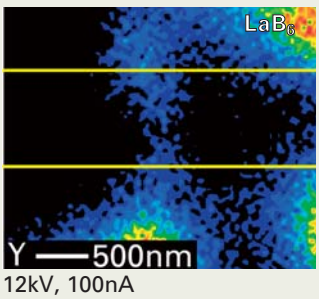


12kV, 100nA

# Introduction of New Products

## Gas Chromatograph Time-of-Flight Mass Spectrometer
## JMS-T100GCV

The JMS-T100GCV is a fully automatic Gas Chromatograph Time-of-Flight Mass Spectrometer (GC-TOFMS). This high-end spectrometer, designed based on a reflectron TOFMS, allows for high-sensitivity measurement comparable to SIM analysis with high-resolution mass chromatogram, as well as accurate mass measurement of trace components, thus satisfying any needs in GC-MS analyses.
The EI (Electron Ionization) ion source is provided as standard, and various other ion sources such as a CI (Chemical Ionization) ion source, an FD/FI (Field Desorption/Field Ionization) ion source and EI/FI/FD (combined ion source of Electron Ionization and Field Ionization/Field Desorption) are available as optional accessories.


## Scanning Probe Microscope
## JSPM-5410

The JSPM-5410, a renewal of JEOL environmental conventional SPM, is a high-end SPM that successfully employs modern control theory for high speed scanning up to 20 times faster than usual scanning.
Also, the JSPM-5410 can be used in various environments such as air, vacuum, controlled atmospheres and liquid. The sample heating and cooling are also enabled under various environments.
The JSPM-5410 has major operation modes as standard functions and it is easy to add on various operation modes.

***Features***

- Rapid scanning up to 20 times faster than usual scanning.
- High resolution. Horizontal 0.1 nm, Vertical 0.02 nm
- Built-in non-contact mode enabling high resolution with no damage to imaging
- Multiple environmental observation in the air, vacuum and fluid
- Sample heating and cooling
- New designed sophisticated user interface

ISO 9001 & 14001 REGISTERED FIRM
DNV Certification B.V., THE NETHERLANDS

JEOL ISO 9001 & ISO 14001 Certificated

Certain products in this brochure are controlled under the "Foreign Exchange and Foreign Trade Law" of Japan in compliance with international security export control. JEOL Ltd. must provide the Japanese Government with "End-user's Statement of Assurance" and "End-use Certificate" in order to obtain the export license needed for export from Japan. If the product to be exported is in this category, the end user will be asked to fill in these certificate forms.


JEOL JEOL Ltd. 1-2 Musashino 3-chome Akishima Tokyo 196-8558 Japan Sales Division ☎(042)528-3381 FAX(042)528-3386

http://www.jeol.com/

**ARGENTINA**
COASIN S.A.C.I.yF.
Virrey del Pino 4071,
1430 Buenos Aires
Argentina
Telephone: 54-11-4552-3185
Facsimile: 54-11-4555-3321

**AUSTRALIA & NEW ZEALAND**
JEOL(AUSTRALASIA) Pty.Ltd.
Suite 1, L2 18 Aquatic Drive
- Frenchs Forest NSW 2086
Australia
Telephone: 61-2-9451-3855
Facsimile: 61-2-9451-3822

**AUSTRIA**
LABCO GmbH
Dr.-Tritremmel-Gasse 8,
A-3013 Pressbaum, Austria
Telephone: 43-2233-53838
Facsimile: 43-2233-53176

**BANGLADESH**
A.Q. CHOWDHURY SCIENCE & SYNERGY PVT. LTD.
House No. 12, Road No. 5A
Sector No. 11, Uttara Dhaka - 1230
Bangladesh
Telephone: 880-2-9980790, 8953450, 8953501
Facsimile: 880-2-8854428

**BELGIUM**
JEOL (EUROPE) B.V.
Planet II, Gebouw B
Leuvensesteenweg 542,
B-1930 Zaventem
Belgium
Telephone:32-2-720-0560
Facsimile:32-2-720-6134

**BRAZIL**
FUGIWARA ENTERPRISES
INSTRUMENTOS CIENTIFICOS LTDA.
Avenida Itaberaba, 3563
02739-000 Sao Paulo, SPI Brazil
Telephone: 55-11-3983 8144
Facsimile: 55-11-3983 8140

**CANADA**
JEOL CANADA, INC.
(Represented by Soquelec, Ltd.)
5757 Cavendish Boulevard, Suite 540,
Montreal, Quebec H4W 2W8, Canada
Telephone: 1-514-482-6427
Facsimile: 1-514-482-1929

**CHILE**
TECSIS LTDA.
Avenida Kennedy 5454 - Piso 5
Vitacura, Santiago, Chile
Telephone: 56-2-401-8520
Facsimile: 56-2-410-8541

**CHINA**
JEOL LTD., BEIJING OFFICE
Room B1110/11, Wantong New World Plaza
No. 2 Fuchengmenwai Street, Xicheng District,
Beijing 100037, P.R.China
Telephone: 86-10-6804-6321/6322/6323
Facsimile: 86-10-6804-6324

JEOL LTD., SHANGHAI OFFICE
Shanghai Equatorial Hotel Office Building 803,
65 Yanan Road West, Shanghai 200040, P.R. China
Telephone: 86-21-6248-4868/4487/4537/4404
Facsimile: 86-21-6248-4075

JEOL LTD., GUANG ZHOU OFFICE
N3104, World Trade Center Building
371-375, Huan Shi East-Road, Guang Zhou,
510095, P.R.China
Telephone: 86-20-8778-7848
Facsimile: 86-20-8778-4268

JEOL LTD., WUHAN OFFICE
Room 3216, World Trading Bldg.
686 Jiefang Street, Hankou, Wuhan, Hubei 430032
P.R.China
Telephone: 86-27-8544-8953
Facsimile: 86-27-8544-8695

JEOL LTD., CHENGDU OFFICE
1807A Zongfu Building,
NO. 45 Zhongfu Road, Chengdu, Sichuan, 610016
P.R. China
Telephone: 86-28-86622554
Facsimile: 86-28-86622564

**CYPRUS**
JEOL (EUROPE) SAS
Espace Claude Monet, 1 Allee de Giverny
78290, Croissy-sur-Seine, France
Telephone: 33-13015-3737
Facsimile: 33-13015-3747

**EGYPT**
JEOL SERIVCE BUREAU
3rd Fl. Nile Center Bldg., Nawal Street,
Dokki, (Cairo), Egypt
Telephone: 20-2-3335-7220
Facsimile: 20-2-3338-4186

**FRANCE**
JEOL (EUROPE) SAS
Espace Claude Monet, 1 Allee de Giverny
78290, Croissy-sur-Seine, France
Telephone: 33-13015-3737
Facsimile: 33-13015-3747

**GERMANY**
JEOL (GERMANY) GmbH
Oskar-Von-Miller-Strasse 1a, 85386
Eching, Germany
Telephone: 49-8165-77346
Facsimile: 49-8165-77512

**GREAT BRITAIN & IRELAND**
JEOL (U.K.) LTD.
JEOL House, Silver Court, Watchmead,
Welwyn Garden City, Herts AL7 1LT, U.K.
Telephone: 44-1707-377117
Facsimile: 44-1707-373254

**GREECE**
N. ASTERIADIS S.A.
56-58,S. Trikoupi Str. P.O. Box 26140
GR-10022, Athens, Greece
Telephone: 30-1-823-5383
Facsimile: 30-1-823-9567

**HONG KONG**
FARMING LTD.
Unit 1009, 10/F., MLC Millennia Plaza
663 King's Road, North Point, Hong Kong
Telephone: 852-2815-7299
Facsimile: 852-2581-4635

**INDIA**
BLUE STAR LTD. (HQ: Mumbai)
Analytical Instrments Department,
Sahas' 414/2 Veer Savarkar Marg
Prabhadery Mumbai 400 025, India
Telephone: 91-22-6666-4000
Facsimile: 91-22-6666-4001

BLUE STAR LTD. (Delhi)
Analytical Instruments Department,
E-44/12 Okhla Industrial Area,
Phase-II, New Delhi 110 020, India
Telephone: 91-11-4149-4000
Facsimile: 91-11-4149-4005

BLUE STAR LTD. (Calcutta)
Analytical Instruments Department,
7, Hare Street Calcutta 700 001, India
Telephone: 91-33-2213-4133
Facsimile: 91-33-2213-4102

BLUE STAR LTD. (Chennai)
Analytical Instruments Department,
Garuda Building,
46, Cathedral Road, Chennai 600 086, India
Telephone: 91-44-4244-4000
Facsimile: 91-44-4244-4190

**INDONESIA**
PT. TEKNOLABindo Penta Perkasa
Komplek Gading Bukit Indah Blok I/11
Jl. Bukit Gading Raya Kelapa Gading Permai,
Jakarta 14240, Indonesia
Telephone: 62-21-45847057/58/59
Facsimile: 62-21-45842729

**ITALY**
JEOL (ITALIA) S.p.A.
Centro Direzionale Green Office
Via dei Tulipani, 1
20090 Pieve Emanuele (MI) Italy
Telephone: 39-02-9041431
Facsimile: 39-02-90414343

**KOREA**
JEOL KOREA LTD.
Dongwoo Bldg. 7F, 458-5, Gil-Dong,
Gangdong-Gu, Seoul, 134-010, Korea
Telephone: 82-2-511-5501
Facsimile: 82-2-511-2635

**KUWAIT**
YIACO MEDICAL Co.K.S.C.C.
P.O. Box 435
13005-Safat, Kuwait
Telephone: 965-24842322/24814358
Facsimile: 965-24844954/24833612

**MALAYSIA**
JEOL(MALAYSIA) SDN.BHD.(359011-M)
205, Block A, Mezzanine Floor,
Kelana Business Center,
97, Jalan SS 7/2, Kelana Jaya,
47301 Petaling Jaya, Selangor, Malaysia
Telephone: 60-3-7492-7722
Facsimile: 60-3-7492-7723

**MEXICO**
JEOL DE MEXICO S.A. DE C.V.
Av. Amsterdam #46 DEPS. 402
Col Hipodromo, 06100, Mexico D.F.
Mexico
Telephone: 52-5-55-211-4511
Facsimile: 52-5-55-211-0720

**PAKISTAN (Karachi)**
ANALYTICAL MEASURING SYSTEM (PVT) LTD.(AMS LTD.)
14-C Main Sehar Commercial Avenue Lane 4,
Khayaban-e-Sehar,
D.H.A-VII, Karachi-75500, Pakinstan
Telephone: 92-21-5345581/5340747
Facsimile: 92-21-5345582

**PANAMA**
PROMED S.A.
Parque Industrial Costa del Este
Urbanizacion Costa del Este
Apartado 0816-01755, Panama, Panama
Telephone: 507-303-3100
Facsimile: 507-303-3115

**PHILIPPINES**
PHILAB INDUSTRIES INC.
7487 Bagtikan Street, SAV Makati,
1203 Metro, Manila Phillippines
Telephone: 63-2-896-7218
Facsimile: 63-2-897-7732

**PORTUGAL**
Izasa Portugal Lda.
R. do Proletariado, 1
2790-138 CARNAXIDE, Portugal
Telephone: 351-21-424-73-00
Facsimile: 351-21-418-60-20

**RUSSIA**
JEOL LTD Moscow Office
Pereulok Krasina 16, bld 1. Office 302,
Moscow, Russia
Telephone: 7-495-641-11-14
Facsimile: 7-495-641-28-63

**SAUDI ARABIA**
ABDULREHMAN ALGOSAIBI G.T.C. (Riyadh)
King Abdulaziz Avenue,
P.O. Box 215, Riyadh 11411, Saudi Arabia
Telephone: 966-1-479-3000
Facsimile: 966-1-477-1374

**SCANDINAVIA**
JEOL (SKANDINAVISKA) A.B.
Hammarbacken 6A, Box 716, 191 27 Sollentuna
Sweden
Telephone: 46-8-28-2800
Facsimile: 46-8-29-1647

SERVICE & INFORMATION OFFICE
JEOL NORWAY
Ole Deviks vei 28, N-0614 Oslo, Norway
Telephone: 47-2-2-64-7930
Facsimile: 47-2-2-65-0619

JEOL FINLAND
Ylakaupinkuja 2, FIN-02360 Espoo, Finland
Telephone: 358-9-8129-0350
Facsimile: 358-9-8129-0351

JEOL DENMARK
Naverland 2, DK-2600 Glostrup, Denmark
Telephone: 45-4345-3434
Facsimile: 45-4345-3433

**SINGAPORE**
JEOL ASIA PTE. LTD.
2 Corporation Road #01-12 Corporation Place
Singapore 618494
Telephone: 65-6565-9989
Facsimile: 65-6565-7552

**SOUTH AFRICA**
ADI Scientific (Pty) Ltd.
370 Angus Crescent,
Northlands Business Park, 29 Newmarket Road
Northriding, Ranburg, Republic of South Africa
Telephone: 27-11-462-1363
Facsimile: 27-11-462-1466

**SPAIN**
IZASA. S.A.
Argoneses, 13, 28100 Alcobendas,
(Poligono Industrial), Madrid, Spain
Telephone: 34-91-663-0500
Facsimile: 34-91-663-0545

**SWITZERLAND**
JEOL (GERMANY) GmbH
Oskar-Von-Miller Strasse 1,
85386 Eching, Germany
Telephone: 49-8165-77346
Facsimile: 49-8165-77512

**TAIWAN**
JIE DONG CO., LTD.
7F, 112, Chung Hsiao East Road,
Section 1, Taipei, Taiwan 10023
Republic of China
Telephone: 886-2-2395-2978
Facsimile: 886-2-2322-4655

For Semiconductor Products:
JEOL TAIWAN SEMICONDUCTORS LTD.
11F-1, No. 346, Pei-Da Road, Hsin-Chu City 300,
Taiwan, Republic of China
Telephone: 886-3-523-8490
Facsimile: 886-3-523-8503

**THAILAND**
BECTHAI BANGKOK EQUIPMENT & CHEMICAL CO., Ltd.
300 Phaholyothin Rd. Phayathai, Bangkok 10400,
Thailand
Telephone: 66-2-615-2929
Facsimile: 66-2-615-2350/2351

**THE NETHERLANDS**
JEOL (EUROPE) B.V.
Lireweg 4, NL-2153 PH Nieuw-Vennep,
The Netherlands
Telephone: 31-252-623500
Facsimile: 31-252-623501

**TURKEY**
TEKSER LTD.STI.
Acibadem Cad. Erdem Sok, Nº 6/1
34660, Uskudar, Istanbul, Turkey
Telephone: 90-216-3274041
Facsimile: 90-216-3274046

**UAE**
BUSINESS COMMUNICATIONS LLC. (Abu Dhabi)
P.O. Box 2534, Abu Dhabi UAE
Telephone: 971-2-6348495
Facsimile: 971-2-6316465

BUSINESS COMMUNICATIONS LLC. (Dubai)
P.O. Box 233, Dubai, UAE
Telephone: 971-4-2220186
Facsimile: 971-4-2236193

**USA**
JEOL USA, INC.
11 Dearborn Road, Peabody, MA 01960, U.S.A.
Telephone: 1-978-535-5900
Facsimile: 1-978-536-2205/2206

JEOL USA, INC. WEST OFFICE
5653 Stoneridge Drive Suite #110
Pleasanton, CA 94588, U.S.A.
Telephone: 1-925-737-1740
Facsimile: 1-925-737-1749

**VENEZUELA**
GOMSA Service and Supply C.A.
Urbanizacion Montalban III
- Residencias Don Andres - Piso 7 - Apartomento 74
Avenida 3, entre calles 7 y 6
Montalban, Caracas, Venezuela
Telephone: 58-212-443-4342
Facsimile: 58-212-443-4342

**VIETNAM**
TECHNICAL MATERIALS AND RESOURCES IMPORT-EXPORT JOINT STOCK COMPANY(REXCO)
Hanoi Branch,
157 Lang Ha Road, Dong da District, Hanoi, Vietnam
Telephone: 84-4-562-0516,17/562-0535
Facsimile: 84-4-853-2511



*(Ser. No. 127)*

*No. 9801F930C Printed in Japan, Kp*